공학박사 학위논문

Heterogeneous Catalytic Dehydrative Reactions for the Conversion of Biomass-derived C4 Chemicals

바이오매스로부터 유래하는 C4 화학물질의 전환을 위한 비균일계 탈수적 촉매반응

2016년 2월

서울대학교 대학원

화학생물공학부

김 태 용

Abstract

Heterogeneous Catalytic Dehydrative Reactions for the Conversion of Biomass-derived C4 Chemicals

Tae Yong Kim
School of Chemical and Biological Engineering
The Graduate School
Seoul National University

The utilization of biomass for the production of fine chemicals has been attracted as an alternative way to conventional petrochemical processes. As biomass-derived feedstocks contain abundant oxygen atoms, selective removal of oxygen is required to produce fine chemicals previously obtained from petroleum. Dehydrative reactions such as dehydration and esterification are effective to reduce oxygen content of biomass-derived feedstock as well as to produce desired functional groups. In this thesis, heterogeneous dehydrative reactions for the conversion of biomass-derived C4 chemicals including 2,3-butanediol and 1-butanol are studied.

At first, a novel type of dehydration reaction that produces 2,3-epoxybutane from 2,3-butanediol (dehydrative epoxidation) is discovered and explored. Among a number of tested basic catalysts, the CsO_x/SiO_2 catalyst showed outstanding performance for the dehydrative epoxidation of 2,3-butanediol and is considered to be the most promising catalyst for this type of reaction. In order to identify the superiority of the CsO_x/SiO_2 catalyst and a mechanism of the reaction, structure-activity relationships were studied along with density

functional theory (DFT) calculations. The following features are found to be responsible for the excellent activity of the CsO_x/SiO_2 catalyst: i) strong basic sites formed by Cs^+, ii) low penetration of Cs^+ into SiO_2 which permits basic sites to be accessible to the reactant, iii) stable basic sites due to the strong interactions between Cs^+ and SiO_2 surface, and iv) mildly acidic surface of SiO_2 which is advantageous for the elimination to H_2O. In addition, the dehydrative epoxidation involves an inversion of chirality (e.g. *meso*-2,3-butanediol (*R,S*) to *trans*-2,3-epoxybutane (*R,R* or *S,S*)), which is in agreement with DFT results that the reaction follows a stereospecific S_N2-like mechanism.

The 2,3-epoxybutane produced from the dehydrative epoxidation of 2,3-butanediol can be further utilized to produce fine chemicals. When 2,3-epoxybutane was reacted over basic lithium phosphate catalyst, isomerized product, 3-buten-2-ol, was obtained with high selectivity. Furthermore, it was found that 3-buten-2-ol is an ideal precursor for the production of 1,3-butadiene. Reaction of 3-buten-2-ol over acidic mesoporous aluminosilicate (Al-MCM-41) led to dominant formation of 1,3-butadiene via acid-catalyzed dehydration. On the basis of the results, heterogeneous catalytic process for the production of 1,3-butadiene from 2,3-butanediol is proposed.

Esterification of 1-butanol with carboxylic acid produces various esters which can be utilized to environmentally friendly solvents and precursors for fragrances. Esterification reactions are industrially conducted with homogeneous mineral acid catalysts, which causes process and environmental problems. Heterogeneous acid catalyst for the esterficiation reactions is essential to overcome the current problems. Zr-WO_x clusters on WO_x/ZrO_2 catalyst are known to be active sites for the acid catalyzed reactions, such as dehydration of alcohols and alkane isomerization reactions. However synthetic methods for producing high density of Zr-WO_x clusters with high surface areas are not currently available. A facile method for preparing mesoporous Zr-WO_x/SiO_2 is proposed and the effect of Zr/W ratio on its structure and acidity

was examined. Results showed that the sequential hydrolysis of zirconium and tungsten via soft-templating resulted in the formation of Zr-WO_x clusters with uniform mesopore structures and a high acidity. The prepared Zr-WO_x/SiO_2 was characterized by N_2 physisorption, XRD, TEM, XPS, UV-Vis spectroscopy, NH_3-TPD and in-situ FTIR. Catalytic performance for the esterification of 1-butanol with acetic acid was evaluated. The materials had a high surface area of over 500 m^2/g and ordered cylindrical pores with a uniform size of ca. 5 nm. Below a Zr/W ratio of ≈0.5, the zirconium was primarily associated with tungstate rather than SiO_2, which indicates the formation of Zr-WO_x clusters. The highest density of Zr-WO_x clusters was obtained at a Zr/W ratio of 0.3 with a strong Brønsted acidity. Consequently, Zr-WO_x/SiO_2, as a Zr/W ratio of 0.3 exhibited the highest activity with a significantly improved performance compared to HZSM-5 and WO_x/ZrO_2 catalysts.

Keywords: Heterogeneous catalysis, dehydration, esterification, reaction mechanism, catalytic process

Student Number: 2011-30277

Contents

List of Tables

List of Figures

List of Schemes

Chapter 1. Introduction

1.1 Biomass as a source for chemical production

With growing demand for sustainability of chemical processes, the catalytic conversion of biomass to value-added chemicals has been raised as an alternative to conventional petrochemical processes [1]. Since biomass-derived feedstocks contain abundant oxygen atoms (O/C ratio up to 0.6 for woody biomass [2]), as opposed to petrochemical feedstocks (O/C ratio less than 0.02 [3]), the selective removal of oxygen is a central challenge for producing valuable chemicals using biomass sources [4-6]. In this connection, dehydrative reactions, such as dehydration and esterification, play a key role in the reduction of abundant oxygen from biomass-derived feedstocks. For example, in the case of the production of HMF from glucose [7,8] and furfural from xylose [8-10], half of the oxygen atoms in sugars are effectively removed by dehydration reactions.

In the aspect of chemical structure, hydroxyl and carboxylic acid groups are two major chemical structure present in biomass-derived feedstocks. Therefore, dehydration and esterification reactions also have significance in the formation of desirable functional groups as well as the removal of oxygen atoms. Hydroxyl groups in biomass-derived feedstocks can be effectively converted into functional groups, such as C=C and C=O bonds, via dehydration. The formation of such functional groups by dehydration made it possible to produce

DMF [11,12], γ-valerolactone [13], alkanes and alkenes [14] from biomass-derived feedstocks. In addition, the consecutive dehydration of glycerol led to the formation a C=O bond (3-hydroxypropionaldehyde) followed by C=C bond formation, resulting in the production of acrolein which is a valuable precursor for the production of acrylic acid [15-17]. On the other hand, esterification reaction is useful to convert carboxylic acid group to ester group. The esterification can produce esters from biomass-derived carboxylic, acids such as lactic acid, succinic acid, itacconic acid, and glutamic acid. The produced esters are potentially useful to solvent liquid as they have non-toxic, bio-degradable, and high-boiling properties [18].

1.2 C4 feedstocks derived from biomass

2,3-Butanediol is the longest chain alcohol found as natural major end product of microbial fermentation along with butanol. Harden and Walpole first reported the production of 2,3-butanediol from microbial fermentation [19]. It is generally synthesized via mixed acid fermentation of pathogenic bacteria such as *Klebsiella pneumonia*, *Klebsiella oxytoca*, *Enterobacter aerogenes*, and *Paenibacillus polymyxa* [20-23]. These bacteria are useful to produce 2,3-butanediol with high yields and productivities, but large-scale fermentation is quiet difficult due to their pathogenic properties. The use of non-pathogenic *Saccharomyces cerevisiae* is considered to be desirable as an alternative. This microbial fermentation is proceeded through several intermediate compounds such as α-acetolactate, diacetyl, and acetoin (Figure 1-1). Other side products, i.e. ethanol, acetate, formate, lactate, and succinate are also synthesized depending on the applied conditions or types of microorganisms. However, microbial fermentation using *Saccharomyces cerevisiae* led to low productivity and yield so that several attempts to improve 2,3-butanediol production have been tried [24-27].

Butanol has been traditionally produced by ABE fermentation which is an anaerobic conversion of carbohydrates by metabolically engineered strains of *Clostridium* into acetone, butanol, and ethanol [28-35]. As two major global corporations, BP and Dupont reported to start butanol production by

fermentation of sugar beet in June 2006 and established the joint-venture Butamax^{TM} Biofuels LLC in 2009, the production of butanol is expected to grow rapidly. On October 2, 2013, Butamax announced that the production facilities for biobutanol has been constructed by simple retrofit of existing Highwater Ethanol' plant in Lamberton, Minnesota [36]. Biobutanol can be produced from cereal crops, sugar cane and sugar beet, etc, but can also be produced from cellulosic raw materials [37].

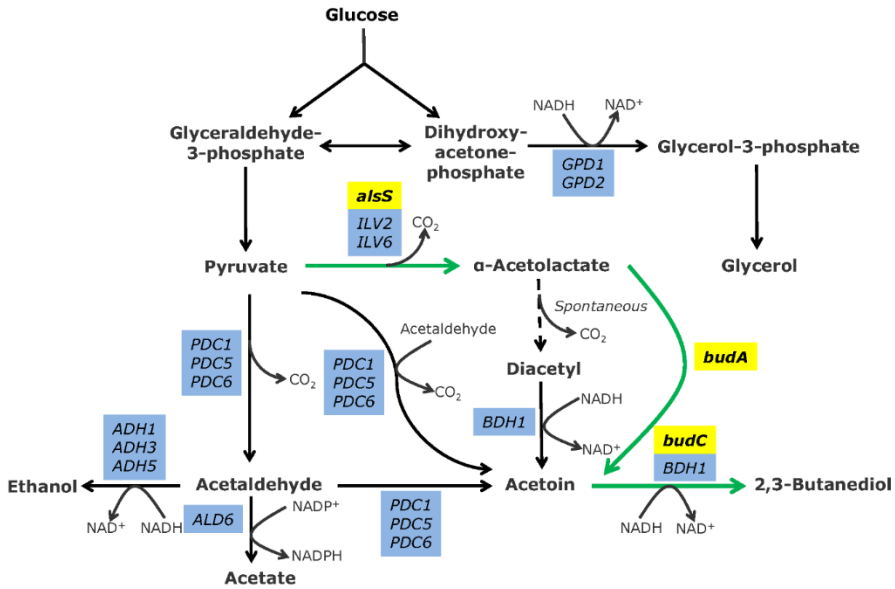

Figure 1-1. Metabolic pathways for the synthesis of 2,3-butanediol in *Saccharomyces cerevisiae*. Green arrow show the bacterial 2,3-butanediol synthesis pathway through α-acetolactate decarboxylase. Blue boxes contain the Saccharomyces cerevisiae innate genes, while yellow boxes indicate the foreign genes introduced to the engineered strains. Figure is reprinted from [35]

1.3 Catalytic dehydrative reactions

Different from petroleum based feedstocks, biomass derived feedstocks contain a plenty of oxygen as a form of alcohol, carboxylic acid, aldehyde, and ketone. Therefore, oxygen removal has to be involved in the conversion of biomass to produce fine chemicals that are derived from petroleum. The dehydrative reaction is advantageous solution to reduce oxygen content as well as to produce chemicals with desired functionality.

1.3.1 Dehydration of 2,3-butanediol and the production of 1,3-butadiene

1,3-butadiene is one of essential monomers for polymer synthesis, and has been solely produced via petrochemical process. Production of 1,3-butadiene from biomass derived feedstock is of great importance in that a renewable resource is utilized as opposed to a petrochemical process. In this regard, 2,3-butanediol has been recognized as an attractive biomass derived feedstock for 1,3-butadiene production [38], because elimination of two water molecules from 2,3-butanediol can lead to the formation of 1,3-butadiene.

Homogeneous catalytic process for the production of 1,3-butadiene from 2,3-butanediol was previously reported in 1945 by S. Marshak et al. [39], and was recently studied in more detail in our group [40]. This process is sequential

esterification of 2,3-butanediol and pyrolysis of produced ester. The esterification of 2,3-butanediol can take place with carboxylic acids like acetic acid and formic acid using H_2SO_4 as a homogeneous catalyst, and produces mono- and di-ester. The di-ester is thermally activated in the pyrolysis step, resulting in the formation of 1,3-butadiene. This process can produce 1,3-butadiene from 2,3-butanediol with high yield ~ 80%, but utilization of homogeneous mineral acid can cause corrosion, separation, and environmental problems. Therefore, a heterogeneous catalytic process is highly desired to realize the production of 1,3-butadiene from 2,3-butanediol.

Acid catalyzed dehydration is conventional and the first choice for heterogeneous catalytic dehydration of alcohols. However, in the case of 2,3-butanediol, the acid catalyzed dehydration resulted in formation of methyl ethyl ketone and isobutraldehyde, which contain unreactive C=O bonding and hamper further dehydration to 1,3-butadiene. Therefore, a novel catalytic route, not based on acid catalysis, is required to realize the heterogeneous catalytic pocess for the production of 1,3-butadiene from 2,3-butanediol.

1.3.2 Esterification of 1-butanol with acetic acid

Industrial esterification processes have utilized homogeneous acid catalysts such as H_2SO_4 and HCl.[41] The homogeneous process provides good productivity with cheap catalysts, but has drawbacks including difficult

separation and severe corrosion problems. Therefore, it is highly desirable to replace the current homogeneous process to heterogeneous one by adopting solid acid catalysts.

There are various options for solid acid catalysts, including zeolites, aluminosilicates, acidic oxides, supported heteropoly acids, ion-exchange resins, and so on. Peters et al. compared several commercial acid catalysts for the liquid phase esterification of acetic acid with butanol [41]. It was found that ion-exchange resins were better performed than zeolites and superacids. The apparent rate constant per acid site for ion-exchange resins, recalculated from data in ref 41, was $3.4 \cdot 10^{-6}$ and $7.1 \cdot 10^{-6}$ $m^3\ mol^{-2}\ s^{-1}$ for Amberlyst 15 and Smopex-101, respectively. These values are slightly lower than sulfuric acid ($2.0 \cdot 10^{-5}$ $m^3\ mol^{-2}\ s^{-1}$) and p-toluenesulfonic acid ($1.0 \cdot 10^{-5}$ $m^3\ mol^{-2}\ s^{-1}$), and are comparable with phosphomolybdic acid ($7.0 \cdot 10^{-6}$ $m^3\ mol^{-2}\ s^{-1}$). In contrast, the apparent rate constant per acid site for zeolites was considerably lower than ion-exchange resin, except for H-USY zeolite which has relatively large pores. The authors proposed that internal diffusion in pores of zeolite limited the reaction. Sulfated zirconia exhibited rate constant similar to Amberlyst 15, but its acid contents were 10-times lower than ion-exchange resin thus much more catalysts were required to achieve similar acid amount.

On the other hand, strength of acid sites is also important requirement for

appropriate catalyst. Corma et al. studied the influence of Si/Al ratio of HY zeolites on the esterification of ethanol with phenylacetic acid [42]. The authors observed increase in activity with increasing Si/Al ratio, which indicates that esterification only takes place at strongly acidic sites. Similar trend was also reported by Peters et al. [41].

On the basis of the literature survey, it can conclude that sufficiently large pore size and strong acid sites are required for esterification catalyst. These required properties make one image mesoporous material with high density of strong acid sites as an ideal catalyst for esterification reaction. Regarding to strongly acidic material, I focused on tungstated zirconia (WO_x/ZrO_2). Tungstated zirconia (WO_x/ZrO_2) catalysts have attracted interest, since Hino and Arata first discovered their strong acidity and low-temperature activity for light alkane isomerization [43] It has been reported to have a high activity for alkane isomerization and the dehydration of alcohols [44-46]. Furthermore, the higher thermal and chemical stabilities of WO_x/ZrO_2 make them attractive for use in a variety of industrial processes [43,46]. It is generally accepted that the strong acidity is due to the strong interaction between zirconia and tungstate or by the presence of Zr-WO_x clusters. Although the origin of strong acidity was identified, methods for improving the activity of WO_x/ZrO_2 catalysts are not available. High surface area mesoporous material combined with active site of WO_x/ZrO_2 can be an ideal catalyst for esterification reaction.

1.4. Objectives

Catalytic conversion of biomass to replace petrochemical processes has become an important issue in the field of catalysis. Current limitations in the conversion of biomass are closely related to the large oxygen contents in biomass. Removal of oxygen atoms is basically required to produce fine chemicals, but catalytic routes as well as known catalytic materials are insufficient to create efficient catalytic process for the biomass conversion.

In this regard, the objective of this thesis is achieving efficient catalytic conversion of biomass-derived 2,3-butanediol and 1-butanol through discovery of a novel catalysis, understanding of reaction mechanism, and development of highly active catalyst.

A novel dehydration reaction which produces 2,3-epoxybutane from 2,3-butanediol is first discovered and studied. Required characteristics for an active catalyst and reaction mechanism are proposed based on experimental results and theoretical calculations. On the basis of this novel reaction, heterogeneous catalytic process for the production of 1,3-butadiene from 2,3-butanediol is proposed.

Design and synthesis of an active catalyst for the esterification of 1-butanol with acetic acid is studied. The synthesized catalyst, mesoporous Zr-WO_x/SiO_2, exhibited high surface area and high density of strong acid site. Thanks to these properties, the catalyst showed promising catalytic performance.

Chapter 2. Dehydrative Epoxidation of 2,3-butanediol and Heterogeneous Catalytic Process for the Production of 1,3-butadiene

2.1 Introduction

2,3-butanediol is an attractive biomass-derived feedstock to produce C4 fine chemicals. Researches on the catalytic dehydration of 2,3-butanediol have received little attention, and only few studies have been reported on this issue. Several studies on dehydration of 2,3-butanediol to 3-buten-2-ol were reported [47], but most of the reports related to this subject have been limited to acid catalyzed dehydration, yielding aldehydes and ketones [48-54]. Such restricted uses and studies will not be sufficient to identify efficient reaction pathways for biomass conversion for replacing conventional petrochemical products. In this regard, the discovery of novel dehydration reactions of vicinal diols has the potential to open up new possibilities for the utilization of biomass, and thereby has the potential to expand the scope of chemicals that can be produced from biomass.

Herein, a novel dehydration reaction of 2,3-butanediol (**BD**), leading to the formation of 2,3-epoxybutane (**EB**), is reported. Since the reaction involves the formation of an epoxide ring with the elimination of H_2O, the reaction is referred as 'dehydrative epoxidation'. At first, dehydrative epoxidation of

vicinal diols, including ethylene glycol, 1,2-propanediol, and **BD**, was performed and was compared with previously reported dehydration reactions. A series of active catalysts were screened for the dehydrative epoxidation of **BD**, and the optimum catalyst was identified. The acidic-basic and physicochemical properties of the catalysts were characterized, in order to identify the cause of the difference in catalytic activity with respect to dehydrative epoxidation. In addition, the stereochemistry involved in dehydrative epoxidation was explored. DFT calculations were carried out to determine the energetics of the reaction, including the transition states as well as the configurations and adsorption of the molecules. On the basis of the experimental results and the DFT calculations, the active site of the catalyst and a reaction mechanism for dehydrative epoxidation is proposed. Using the dehydrative epoxidation, heterogeneous catalytic processes for the production of 1,3-butadiene from **BD** is proposed. The process is composed of sequential three reactions: dehydrative epoxidation of **BD** to **EB**, isomerization of **EB** to 3-buten-2-ol (**BO**), and acid-catalyzed dehydration of **BO** to 1,3-butadiene.

2.2 Experimental

2.2.1 Preparation catalysts

Sodium acetate trihydrate (TCI), potassium oxalate monohydrate (Samchun Chemical), cesium acetate (Samchun Chemical), magnesium nitrate hexahydrate (Fluka), calcium nitrate tetrahydrate (Sigma-Aldrich), strontium nitrate (Sigma-Aldrich), lanthanum nitrate hexahydrate (Junsei Chemical), and cerium nitrate hexahydrate (Kanto chemical) were used as precursors for supported basic metal oxide catalysts and were used without further purification. Al-MCM-41 (Aluminosillicate, mesostructured, Sigma-Aldrich) was used as received. The catalysts were prepared by the incipient wetness impregnation method. In typical procedures, at first, a predetermined amounts of precursor was dissolved in 3 ml of deionized water. The aqueous solution of precursor was then added drop-wise to 2.0 g of a support oxide (SiO_2 (Aerosil® 200), Al_2O_3 (Aeroxide® Alu C), and TiO_2 (Aeroxide® P25)) with vigorous mixing by hand for at least 20 min. To prevent a complete wetness, impregnation was conducted repeatedly by dosing a small quantity of precursor solution and followed by drying at room temperature. The impregnated powders were dried at 343 K overnight, and then be grounded and calcined at desired temperature (5 K/min) for 4h.

For the catalysts used in the screening of active materials (section 2.3.2), 10 wt.% (Cs_2O, CaO, SrO, La_2O_3, CeO_2), 2.4 wt.% (Na_2O), 3.6 wt.% (K_2O), and 3.1 wt.% (MgO) were loaded on a SiO_2 support, and the notation of M/SiO_2 is used. Calcination was carried out at 823 K for 4h. In sections 3.3 and 3.4, the

following notation is used to express the SiO_2 supported Cs catalysts: $xCsO_x/SiO_2$-y, where x is the wt.% of Cs_2O loading, and y is the calcination temperature (723 – 1023 K). The catalysts prepared using other supports are expressed in the same way.

Basic lithium phosphate (Li_3PO_4) was prepared by precipitation method. 1.82 g of sodium phosphate monobasic (0.015 mol, NaH_2PO_4, Sigma-Aldrich) and 1.28 g of lithium hydroxide monohydrate (0.030 mol, $LiOH{\cdot}H_2O$, Sigma-Aldrich) were separately dissolved in 15 ml and 10 ml of deionized water, respectively. Prior to precipitation, the former solution (NaH_2PO_4) was transferred to a 100 ml round-bottom flask. The contents were heated and the temperature was maintained at 313 K. The aqueous solution of $LiOH{\cdot}H_2O$ was then added drop-wise with vigorous stirring using a magnetic bar. A white precipitate was immediately formed when the solution was added. The mixed solution was aged at 313 K for 24 h. After the aging, the white precipitates were isolated on a filter, washed three times with 200 ml of de-ionized water, and dried at 343 K for overnight. Calcination of the dried precipitates were conducted at 673 K (5 K/min of ramping speed) for 6 h.

2.2.2 Reactivity tests

A fixed-bed quartz reactor was used to evaluate the catalytic performances of the catalysts for the dehydration of 2,3-butanediol, 1,2-propanediol, and ethylene glycol. Temperature were measured by a K-type thermocouple and were controlled with external electrical furnace. Reactions were performed

using 0.1 g of catalyst samples held on a porous quartz bed with aqueous solutions of 2,3-butanediol (Acros Organics, 98%, mixture of *racemic* and *meso* forms), *meso*-2,3-butanediol (Sigma-Aldrich), 1,2-propanediol, ethylene glycol (Alfa Aesar, 97%), *trans*-2,3-epoxybutane (Alfa Aesar, 97%), *cis*-2,3-epoxybutane (Alfa Aesar, 98%), 3-buten-2-ol (Alfa Aesar, 97%), and methyl ethyl ketone (J.T. Baker, 99.0%). The compositions of reactants in the aqueous solutions were 9.9 wt.% (2.1 mol%) for 2,3-butanediol, 8.3 wt.% (2.1 mol%) for 1,2-propanediol, 6.9 wt.% (2.1 mol%) for ethylene glycol, and 8.1 wt% (2.1 mol%) for the others in order to ensure a same space velocity of reactants (Space velocity (SV) = total flow rate / amounts of catalyst = 1.38 L/(min (g cat)). The reactor was heated to the desired temperatures (673 K) with ramping rate of 10 K/min and maintained for 30 min with a flow of dry N_2 (99.999%, 30 cm^3/min). The reactant solutions were then injected with a rate of 1.5 cm^3/h (1.64 mmol 2,3-butanediol/h) into a pre-heating zone which was maintained at 473 K and was connected to a top of the reactor. Effluent gases were passed through a helix type condenser and was collected in a sample tube containing 20 ml of deionized water. Acetonitrile was used as an external standard for quantification and added to products collected hourly. The products were analyzed using gas chromatography (Younglin ACME 6100 instrument) equipped with a FID detector and Rtx®-VRX capillary column (Restek, cat. # 19316). The data acquired at 2 h of the reaction was used to compare the catalytic activity of the catalysts. In case of the acid catalyzed dehydration of the intermediates, 1,3-butadiene in the effluent gases was analyzed using an on-line gas chromatograph (Donam DS 6200)

equipped with a FID detector and HayeSep C-ValcoPLOT® capilary column (VICI®, Product no. CFS-PC3053-200). The turnover frequency (TOF) and specific formation rates of products for supported catalysts were calculated by following equations:

$$\text{Turnover frequency } (\mathrm{h}^{-1}) = \frac{Converted \quad amounts \quad of \quad reactant \quad (mol/h)}{Loaded \quad amounts \quad of \quad metal \quad (mol)}$$

$$\text{Specific formation rate } (\mathrm{h}^{-1}) = \frac{Formed \quad amounts \quad of \quad product \quad (mol/h)}{Loaded \quad amounts \quad of \quad metal \quad (mol)}$$

2.2.3 Characterization

Temperature programmed desorption (TPD) of NH_3 was carried out using Micromeritics Autochem II chemisorption analyzer. Prior to the analysis, 0.1 g of sample was heated at 673 K for 1h under a He flow to remove adsorbed impurities. After cooling to 323 K, the sample was saturated with probe by a flow of 10.2% NH_3/He. The physisorbed probe was removed by flushing of He flow at 373 K. After the sample was cooled down to 323 K and the TCD signal was stabilized, the signal was recored with increasing the temperature from 323 K to 673 K at a rate of 10 K/min under a flow of He.

The Hammett indicator titration method was utilized to compare the base strength of the prepared catalysts. In typical procedure, the Hammett indicators were dissolved in methanol to obtain 0.05 M solutions. Prior to the titration, a determined amounts (10 mg) of a catalyst was heated at 423 K in vacuum oven to remove adsorbed species. Then, it was titrated by 400 μl of each indicator solution, and color change was recorded. Following four indicators were used:

Neutral red (pK_a = 6.8), phenolphthalein (pK_a = 8.2), 2,4-dinitroaniline (pK_a = 15.0), and 4-nitroaniline (pK_a=18.4). Benzoic acid titration method was employed to quantify the total basicity of the catalysts.

X-ray photoelectron spectroscopy (XPS) was carried out on a KRATOS AXIS electron spectrometer equipped with MgKα radiation. The binding energies were corrected using C_{1s} as an internal standard (284.6 eV). The peaks were fitted by mixed Gaussian-Lorentzian functions with substraction of Shirley type background using XPS peak fitting program (XPSPEAK 4.1).

^{29}Si cross polarization/magic angle spinning (CP/MAS) nuclear magnetic resonance (NMR) spectra of the samples were recorded on a Bruker AVANCE 400 WB (400 MHz) spectrometer operating at a frequency of 79.5 MHz. The magic angle spin speed used for ^{29}Si spectral recording was 5 kHz. ^{133}Cs MAS NMR spectra were recorded on the same instrument operating at a frequency of 52.5 MHz and 7 kHz of the magic angle spin speed. Electron spin resonance (ESR) spectra of the catalysts were recorded on a JEOL JES-TE200 spectrometer operating at 9.43 GHz of a microwave frequency and 1.0 mW of a microwave power. The differential scanning calorimetry (DSC) and thermogravimetric analysis (TGA) were performed on a TA instruments SDT Q600 analyzer. The temperature was increased from room temperature to 1173 K with a heating rate of 10 K/min under an air flow.

High resolution transmission electron micrograph (HR-TEM) images were obtained on a JEOL JEM-3010 microscope using bright field (BF) mode with an acceleration voltage of 300 kV. The X-ray diffraction (XRD) patterns were measured by a Rigaku D-MAX2500-PC powder X-ray diffractometer with Cu

Kα radiation (1.5406 Å) in an operating mode of 50 kV and 100 mA. An analytical high-angle annular dark-field scanning transmission electron microscope (HAADF-STEM, Tecnai F20-FEI, 200 kV) equipped with energy dispersive X-ray spectroscopy (EDS, Tecnai 136−5-EDAX) was used to explore the distribution of elements over the prepared catalysts. N_2 adsorption-desorption analyses were carried out using a Micromeritics ASAP-2010 instrument. The total surface area of the samples was calculated by the BET method (P/P_o = 0.1-0.2). The pore volume and pore size distributions were obtained from the desorption branches of the isotherms using BJH methods.

2.2.4 Computational details

Periodic density functional theory (DFT) calculations were carried out using the Vienna *ab initio* simulation package (VASP) [55]. The generalized gradient approximation (GGA) parameterized by Perdew-Burke-Ernzerhof (PBE) exchange-correlation functional was employed [56]. Ionic cores were described by the projector augmented wave (PAW) method [57]. Dispersion forces were included with the DFT-D2 Grimme's empirical correction [58]. The C6 (57.74 J nm^6/mol) and R0 (1.776 Å) parameters for cesium were taken from the data of F. Zhang et al [59]. The wave functions were constructed from the expansion of planewaves with an energy cutoff of 400 eV. A 1 × 1 × 1 Monkhorst-Pack *k*-point mesh was used to sample the Brillioun zone. All calculations were converged until the forces on all atoms were less than 0.03 eV/Å. The electronic optimization steps were converged self-consistently to < 2 × 10-4 eV.

In our calculations, β-cristobalite (001) was used to represent the surface of the amorphous SiO_2. It has been often used for the same purpose because the physical properties, including refractive index and bulk density, of β-cristobalite are close to those of amorphous SiO_2 [60,61]. Previous reports also have supported that (001) and (111) plane of β-cristobalite successfully describe the surface of amorphous SiO_2 [60-63]. Detailed explanation about the model can be found in the report of J. Handzlik et al.[64] I42d space group with Si in 4 (a) and O in 8 (d) crystallographic positions [65] was used as an initial structure for geometry optimization of bulk β-cristobalite. For the calculation of bulk optimization, the cutoff energy was increased to 520 eV and a 4 × 4 × 4 *k*-point mesh was used. The lattice constants of the fully optimized bulk structure are found to be 5.02 Å (a, b) and 7.38 Å (c), which is in agreement with the experimentally reported values of 5.04 Å (a, b) and 7.13 Å (c) [65]. The surface was constructed by cleaving (2 × 2 × 1) optimized bulk structure (a = b = 10.04 Å) along the (001) plane. To prevent in-physical electronic interactions, 20 Å of vacuum region between the slabs was added. Dangling oxygens on the surface were fully hydroxylated by adding equal number of hydrogens. The surface consisted of 8 layers (4 Si layers and 4 O layers). The top four layers were allowed to relax while the remaining four bottom layers were fixed. The surface of CsO_x/SiO_2 was constructed by replacing one of the hydrogen atoms with Cs atom since Cs ion in CsO_x/SiO_2 has same oxidation state (+1) as proton, and is capable to exchange with the proton [66-69]. Experimental evidences are also provided by XPS analysis of CsO_x/SiO_2 catalyst. The most stable geometries for the adsorption of *anti-meso*-2,3-

butanediol, *gauche-meso*-2,3-butanediol, *cis*-2,3-epoxybutane and *trans*-2,3-epoxybutane were obtained by systematically exploring the adsorption sites on the CsO_x/SiO_2 surface. The adsorption energies were calculated as follows: $\Delta E_{ads} = E_{adsorbate/surface} - E_{adsorbate} - E_{surface}$.

The transition state was located using climbing image-nudged elastic band (CI-NEB) method [70,71]. Seven equally spaced images were obtained by linear interpolation and used as initial trajectories for reaction path. In the CI-NEB calculations, the images was refined until the maximum atomic forces are converged within 0.06 eV/Å.

2.3 Results and discussion

2.3.1 The dehydrative epoxidation of vicinal diols

Acidic catalysts are frequently used as dehydration catalysts and were mainly adopted to use in the dehydration of vicinal diols. The dehydration of vicinal diols in the presence of an acidic catalyst preferentially produces aldehydes and ketones via a carbocation intermediate which is frequently observed in acid catalysis [48-54]. On the other hand, S. Sato et al. utilized the rare-earth and transition-metal oxides for the dehydration of vicinal diols including 1,2-propanediol, 2,3-butanediol (**BD**), and 1,2-butanediol [47,72]. In the reports, main products of reaction over the rare-earth metal oxides were aldehydes and ketones as similar to the acid catalyzed dehydration. When transition metal oxides were utilized, they found that ZrO_2 catalyst is capable of selectively producing 3-buten-2-ol (**BO**) via dehydration of **BD** [47].

In contrast to the above dehydration reactions, the reaction of vicinal diols over a basic CsO_x/SiO_2 catalyst resulted in the formation of new dehydration products (Table 2-1). Epoxides including epoxyethane, 1,2-epoxypropane, and 2,3-epoxybutane (**EB**) were produced from ethylene glycol, 1,2-propanediol, and **BO**, respectively. The reaction of 1,2-propanediol and **BD** also produced unsaturated alcohols (2-propen-1-ol and **BO**, respectively), whereas unsaturated alcohols were not produced in the case of the reaction of ethylene glycol due to the shorter carbon chain. Comparing the reaction results of the vicinal diols (Figure 2-1), the extent of conversion became higher with the length of the carbon chain of the reactant. This is attributed to increased

amounts of epoxides and unsaturated alcohols that are produced. Aldehydes and ketones presented opposite trend and their yields decreased slightly with the longer carbon chain length. Consequently, dehydrative epoxidation takes place more easily for vicinal diols with longer carbon chain.

Considering the fact that typical dehydration leads to the formation of C=C or C=O bonds, the formation of epoxides is clearly a distinguishing result, since a strained intramolecular C-O bond was formed. Sequence of this reaction may be similar to the dehydration of monoethanolamine to ethyleneimine which involves a formation of similar 3-membered ring via dehydration [73]. However, it is important to note that the dehydration of monoethanolamine to ethyleneimine can be induced by SiO_2 catalyst, whereas the formation of epoxides from vicinal diols cannot be. There is definitely distinct catalysis on the formation of epoxides from vicinal diols. Discovering a catalysis that is used in the formation of epoxides from the dehydration of the vicinal diols could be an important issue.

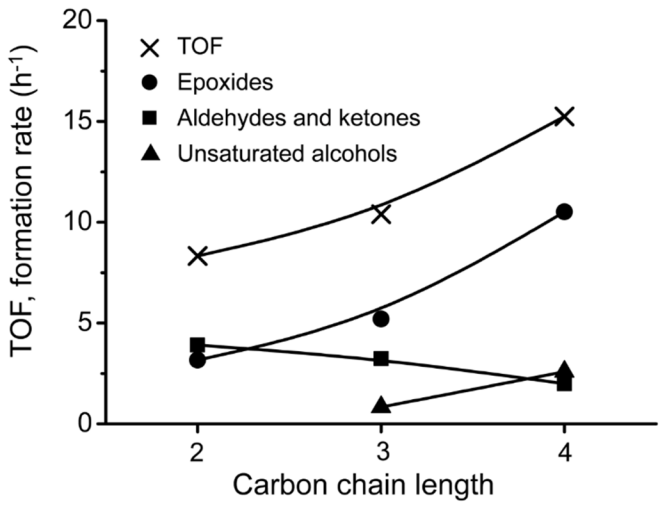

Figure 2-1. Compositional changes in dehydration products with respect to the carbon chain length of the vicinal diols: Carbon chain length of 2, 3, and 4 represents ethylene glycol, 1,2-propanediol, and 2,3-butanediol **BD**, respectively. Reaction condition: Fixed-bed flow reactor, T_{rxn} = 673 K, SV = 1.38 L/(min (g cat)).

Table 2-1 Catalytic reaction of vicinal diols over the CsO_x/SiO_2.[a]

Reactant	Turnover frequency (h^{-1})[b]	Products / Specific formation rate (h^{-1})[c]			
		Epoxide	Unsaturated alcohol	Ketone	Aldehyde
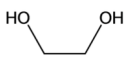 ethylene glycol	8.3 (36)	 epoxyethane	-	-	 acetaldehyde
		4.4 (38)	-	-	3.9 (47)
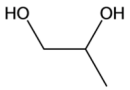 1,2-propanediol	10.4 (45)	 epoxypropane	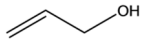 2-propen-1-ol	 acetone	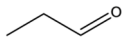 propionaldehyde
		5.2 (50)	0.8 (8)	0.9 (9)	2.3 (22)
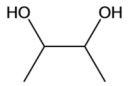 2,3-butanediol (**BD**)	15.3 (66)	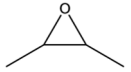 2,3-epoxybutane (**EB**)	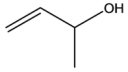 3-buten-2-ol (**BO**)	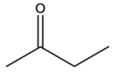 methyl ethyl ketone (**MEK**)	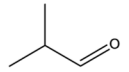 Isobutyraldehyde (**IBA**)
		10.5 (69)	2.6 (17)	1.7 (11)	0.3 (2)

[a] Fixed-bed flow reactor, T_{rxn} = 673 K, SV = 1.38 L/(min (g cat)). [b] he values in parentheses are the conversion of reactant (%). [c] he values in parentheses indicate product selectivity (%).

2.3.2 Dehydrative epoxidation of 2,3-butanediol: Screening of basic metal oxides

To explore the dehydrative epoxidation reaction in more detail, a series of active materials for the reaction is tested. A number of SiO_2 supported catalysts were prepared using alkali, alkaline-earth, and rare-earth metal oxides as basic metal oxides. Acidic Al-MCM-41 was also tested as a reference catalyst. In these experiments, **BD** was used as representative vicinal diol. Since it was confirmed that **BO** is secondary product which is originated from **EB**, the specific activity for the dehydrative epoxidation was compared based on the sum of specific formation rate for **EB** and **BO**. Chemical names, structures, and abbreviations for reactants and products appeared in the conversion of **BD** are summarized in Scheme 2-1.

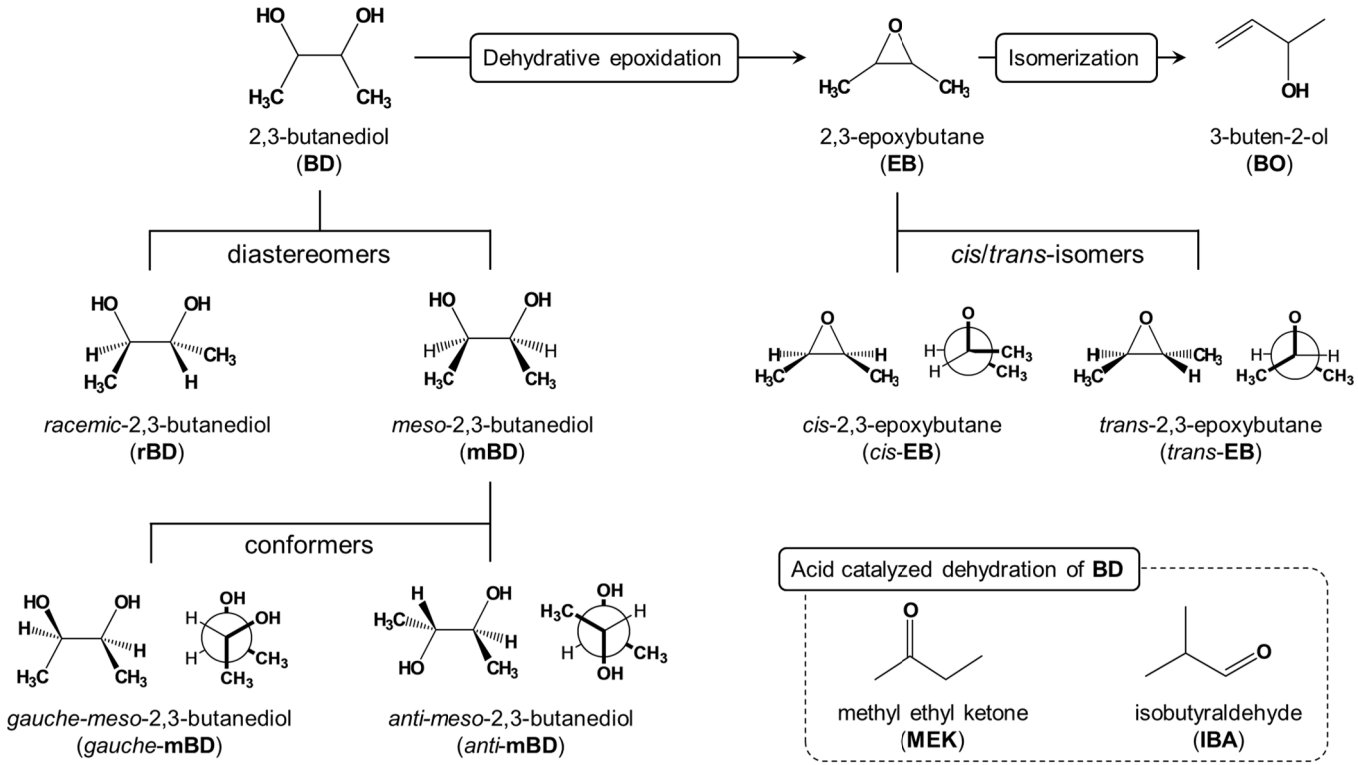

Scheme 2-1. Chemicals included in this study on the dehydration of 2,3-butanediol (**BD**). Names, abbreviations (in parentheses), and structures of reactants and possible products are present.

2.3.2.1 Reactivity tests

In the results for the SiO_2 supported alkali metal oxides (Table 2-2. entry 1-3), KO_x/SiO_2 showed selective formation of **EB** and **BO**, but with considerably lower activity than CsO_x/SiO_2. Specific formation rate of **EB** and **BO** for NaO_x/SiO_2 was 4-fold lower than KO_x/SiO_2. Accordingly, the specific activity for dehydrative epoxidation increased in the order of increasing atomic number of the alkali metal oxides. Meanwhile, the SiO_2 supported alkaline-earth and rare-earth metal oxides (entry 4-8) produced **MEK** and **IBA** mainly. Any trace amounts of **EB** and **BO** were not detected for MgO_x/SiO_2, LaO_x/SiO_2, CeO_x/SiO_2. Only CaO_x/SiO_2 and SrO_x/SiO_2 were capable of producing **EB** and **BO**, but their specific activities were lower than those of the supported alkali metal oxides. Therefore, alkaline-earth and rare-earth metal oxides were considered poorly effective for the dehydrative epoxidation than alkali metal oxides. In the reaction for Al-MCM-41 catalyst (acidic catalyst, entry 9), **MEK** and **IBA** were exclusively produced, as previously reported [53].

Table 2-2 Catalytic performance of the catalysts on the dehydration of 2,3-butanediol.[a]

Entry	Catalysts[b]	Turnover frequency (h^{-1})[c]	Specific formation rate (h^{-1})[d]				Specific activity (h^{-1})[e]
			2,3-epoxybutane (**EB**)	3-buten-2-ol (**BO**)	Methyl ethyl ketone (**MEK**)	Isobutyraldehyde (**IBA**)	
1	NaO_x/SiO_2	4.0 (19)	0.4 (10)	0.2 (5)	2.2 (54)	0.4 (9)	0.6 (2.9)
2	KO_x/SiO_2	4.5 (21)	1.6 (36)	0.5 (12)	1.3 (29)	0.4 (8)	2.1 (10.1)
3	CsO_x/SiO_2	15.3 (66)	10.5 (69)	2.6 (17)	1.7 (11)	0.3 (2)	13.1 (56.8)
4	MgO_x/SiO_2	21.5 (100)	0	0	14.2 (66)	3.9 (18)	0
5	CaO_x/SiO_2	8.2 (89)	0.2 (2)	0.4 (5)	5.0 (62)	1.2 (14)	0.6 (6.2)
6	SrO_x/SiO_2	9.7 (57)	0.3 (3)	0.5 (5)	6.6 (68)	1.0 (10)	0.8 (4.6)
7	LaO_x/SiO_2	26.7 (100)	0	0	19.5 (73)	4.0 (15)	0
8	CeO_x/SiO_2	28.2 (100)	0	0	20.9 (74)	4.2 (15)	0
9	Al-MCM-41[f]	79.7 (100)	0	0	46.2 (58)	23.1 (29)	0

[a] Fixed-bed flow reactor, T_{rxn} = 673 K, SV = 1.38 L/(min (g cat)). [b] Loaded basic metal oxides are denoted by a symbol. [c] The values in parentheses are the conversion of 2,3-butanediol (%). [d] The values in parentheses indicate product selectivity (%). [e] Sum of specific formation rate for 2,3-epoxybutane (**EB**) and 3-buten-2-ol (**BO**). The values in parentheses are the yield of **EB** and **BO**. [f] T_{rxn}=573 K.

2.3.2.2 Acid and basic properties of the screened catalysts

It appeared that dehydrative epoxidation is significantly influenced by the type of loaded basic metal oxides. In order to identify the causes of the catalytic difference among the screened catalysts, the acidic and basic properties of the catalysts were correlated with the reaction results.

Figure 2-2 show the NH_3 TPD results for the catalysts. The loading of basic metal oxides on the SiO_2 support resulted in an increase in acidic sites. This increase would be similar to the formation of acidic sites on heteroatom doped silicate materials [74]. The amounts of acidic sites that are formed vary considerably, depending on the type of loaded metal oxides. MgO_x/SiO_2, CaO_x/SiO_2, and LaO_x/SiO_2 have relatively high amounts of acidic sites, and the SiO_2 supported alkali metal oxides and strontium oxide have medium amounts of acidity. CeO_x/SiO_2 contained a quite low level of acidic sites. The formation of additional acidic sites could cause the considerable formation of **MEK** and **IBA** for the SiO_2 supported alkaline-earth metal oxides and rare-earth metal oxides, as **MEK** and **IBA** are major products of acid catalyzed dehydration. Since Brønsted acidic catalysts were reported to be effective in the formation of **MEK** and **IBA** [53,54], the type of acidic sites formed in these catalysts is predicted to be Brønsted acidic sites. Compared to Al-MCM-41, these SiO_2 supported catalysts produced much smaller amounts of **IBA**. The ratio of **MEK** to **IBA** for Al-MCM-41 was found to be about 2 whereas that for the alkaline-earth and rare-earth metal oxides was considerably higher (ranging from 3.7 to 6.8). The smaller amounts of **IBA** for the SiO_2 supported alkaline-earth and

rare-earth metal oxides implies that acidic sites weaker than those in Al-MCM-41 were formed in these catalysts, because **IBA** is formed via a methyl group rearrangement,[53] which is closely related to the formation of a carbocation [75]. In contrast, much less **MEK** and **IBA** were formed on the SiO_2 supported alkali metal oxides, which indicates that the formed acidic sites by the loading of alkali metal oxides are different from those for alkaline-earth and rare-earth metal oxides, and are probably weak Lewis acidic sites.

The trend for the specific formation rate of **EB** and **BO** among the SiO_2 supported catalysts is also important to note in relation to the base strength of the catalysts. The base strength of alkali, alkaline-earth, and rare-earth metal oxides generally follows the theoretical basicity trend of electronegativity (EN). This relationship of base strength and EN has been frequently reported in metal oxides and hydroxides [76-79], ion-exchanged zeolites [80-84], and supported metal oxides [85,86]. The EN values in the Pauling scale for loaded metals are in decreasing order from Mg (1.31), Ce (1.12), La (1.1), Ca (1.0), Sr (0.95), Na (0.93), K (0.82), to Cs (0.79), which is the opposite trend of base strength. When the specific formation rate of **EB** and **BO** for the SiO_2 supported catalyst is compared with EN values of loaded metal (Figure 2-3), the specific activity tended to increase with decreasing order of EN. Therefore, this relationship indicates that stronger basic sites are more advantageous for dehydrative epoxidation. The specific activity of NaO_x/SiO_2 deviated slightly from the trend because of the significantly decreased surface area of the catalyst (13, 101, 115 m^2/g for NaO_x/SiO_2, KO_x/SiO_2, CsO_x/SiO_2, respectively). A Hammett indicator titration method was utilized to confirm the base strength and total basicity of

the SiO_2 supported catalysts. The results of the Hammett indicator titration method are consistent with the base strength scale by EN of the loaded metal as the catalysts which consisted of a metal oxide with a high EN value showed a lower base strength (MgO_x/SiO_2, LaO_x/SiO_2, and CeO_x/SiO_2). However, the poor resolution of the method due to limitations in the availability of indicators made it difficult to distinguish the base strength of the catalysts within $8.2 < H_- < 15.0$. Comparing the base strength determined by Hammett indicator titrations and activity for the dehydrative epoxidation, the catalysts with strong basic sites of $H_- > 8.2$ were clearly able to trigger the dehydrative epoxidation reaction.

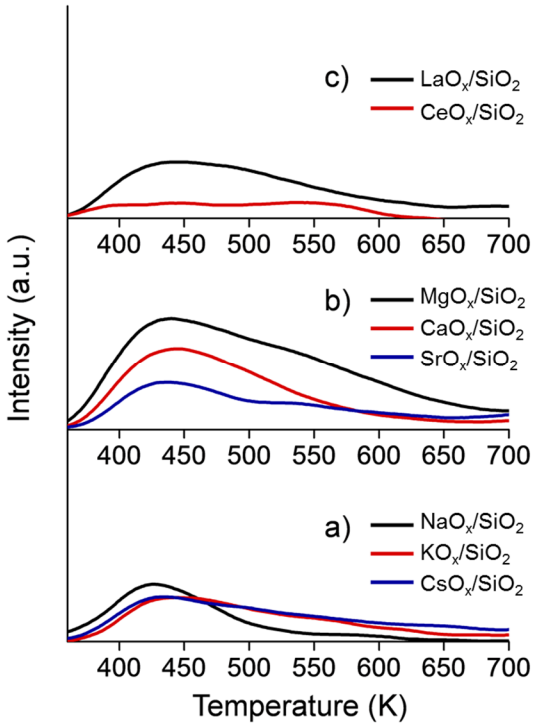

Figure 2-2. NH_3-TPD profiles of the SiO_2 supported basic metal oxide catalysts: a) alkali metal oxides, b) alkaline-earth metal oxides, and c) rare-earth metal oxides.

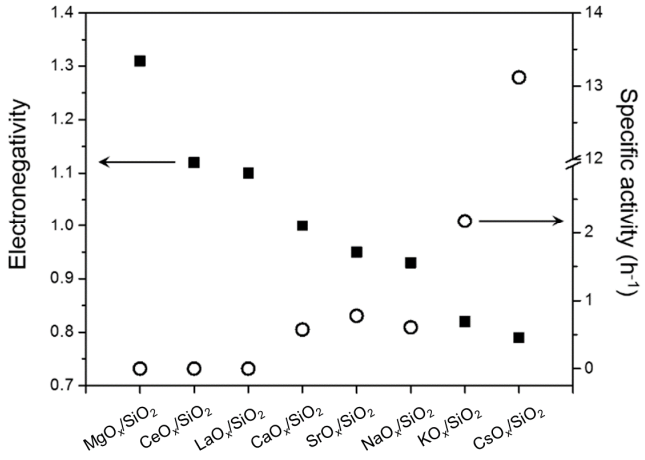

Figure 2-3. Relationship between electronegativity (closed rectangle, left y axis) and the specific activity (open circle, right y axis) for the SiO_2 supported catalysts.

2.3.2.3 Structural characterization of the SiO_2 supported alkali metal oxide catalysts

Among the alkali metal oxides, CsO_x/SiO_2 was found to be exceptionally active for dehydrative epoxidation. This can be attributed, in part, to the stronger basicity of Cs than Na and K. However, difference in base strength does not appear to be sufficient to explain the exceptional performance of CsO_x/SiO_2. To identify other causes for this exceptional performance, the structural characteristics of the supported alkali metal oxides (NaO_x/SiO_2, KO_x/SiO_2, and CsO_x/SiO_2) are compared as well.

The chemical states of alkali metal atoms in the catalysts were analyzed by XPS and ESR (Figure 2-4 and 2-5, respectively). The results indicate that alkali metal atoms on the catalysts are present as metal cations (M^+), and did not exhibit any paramagnetic or diamagnetic properties, indicating the absence of superoxide (O_2^-) and peroxide (O_2^{2-}) species.

HR-TEM and STEM images of the SiO_2 supported alkali metal oxide catalysts are shown in Figure 2-6. The images show the absence of crystalline alkali metal oxide phases and also show that the catalysts are microscopically homogeneous. No evidence was found to the formation of separated particulates or a crystalline phase. The absence of a crystalline phase was also supported by the results of XRD analysis. EDS mapping of the CsO_x/SiO_2 catalyst clearly shows that the Cs atoms are well dispersed within the catalyst. The morphology of the SiO_2 supported catalysts is similar to each other and is nearly identical to bare SiO_2.

In contrast, the results of N_2 adsorption-desorption analyses revealed that the pore structure and specific surface area of the catalysts are considerably different from one another. The BET surface area of the catalysts was 115, 101, and 13 m^2/g for CsO_x/SiO_2, KO_x/SiO_2, and NaO_x/SiO_2, respectively. In the isotherm plots (Figure 2-7), a Type IV isotherm and a H3 hysteresis loop at P/P_0 = 0.8 – 1.0 indicates that inter-particular porosity is common for these catalysts. The inter-particular porosity decreased in the order of Cs < K < Na. This indicates that SiO_2 particles were agglomerated by the loading of alkali metal oxides, the extent of which is in the order of Cs < K < Na. Moreover, the significant decrease in the surface area of NaO_x/SiO_2 can be attributed to the transformation of amorphous SiO_2 to cristobalite by high temperature calcination as a frequently observed in Na-SiO_2 system [87].

Local structures of the SiO_2 supported alkali metal oxide catalysts were explored by means of ^{29}Si CP/MAS NMR (Figure 2-8). In the results, the bare support (SiO_2) shows a characteristic peak at -108 ppm which is assigned to Q^4 species of Si [88]. The slightly asymmetric shape (to positive chemical shift) of the peak indicates that Q^3 species also exist in the support material. When sodium or potassium oxide was loaded on the support, the Q^3 peak (-95 ppm) clearly increased. This change in the spectrum suggests that the highly cross-linked silica network is disrupted by sodium and potassium, resulting in the formation of branching sites. In contrast, the shape of the NMR spectrum for CsO_x/SiO_2 was nearly identical to that of the bare support. The different extent of change in the local silicate structure can be attributed to the strength of silicate dissolving ability of alkali metal cations which is in the order of Cs^+ <

$Na^+ < K^+$ [89]. Considering this trend of dissolving ability, the ionic radii of K^+ (152 pm) which is smaller than Cs^+ (182 pm), and the coarse framework of amorphous silica, K^+ can more easily penetrate into the bulk layer of the support than Cs^+ (Na^+ is not compared since NaO_x/SiO_2 has a considerably lower specific surface area). Experimental evidence for the degree of penetration from XPS spectra of the O 1s orbital of KO_x/SiO_2 and CsO_x/SiO_2 is found as follows: When alkali metal oxides were loaded on the support, a new peak at near 530.5 eV (O_{Alk}) was appeared in O_{1s} spectra due to the interaction of alkali metal cations with nearby oxygen atoms. When the O_{Alk} and alkali metal cations are quantified, the atomic ratio of O_{Alk} and alkali metal cations for KO_x/SiO_2 was determined to be 6.6, which is higher than that for CsO_x/SiO_2 (3.2). This result indicates that K^+ is surrounded by a larger number of oxygen atoms than Cs^+, which means that more K^+ is located in the bulk layer of the SiO_2 support. The penetrated K^+ (and generated basic sites) in KO_x/SiO_2 would be not accessible for the reaction. Consequently, this structural difference between KO_x/SiO_2 and CsO_x/SiO_2 could contribute to the outstanding performance of CsO_x/SiO_2.

Based on these results, it can be concluded that outstanding performance of CsO_x/SiO_2 among the SiO_2 supported alkali metal oxide catalysts can be attributed to i) stronger basic sites induced by the loading of Cs^+, ii) lower agglomeration of SiO_2 particles and less decrease in specific surface area, and iii) sufficiently large ionic radius and lower extent of silicate dissolution that allows Cs^+ to exist on the surface of the catalyst.

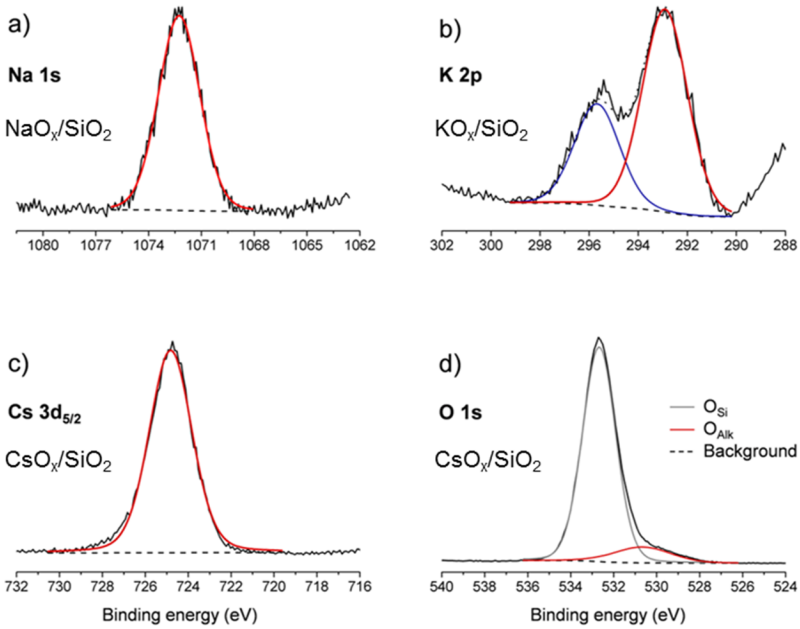

Figure 2-4. XPS spectra of the supported alkali metal oxides: a) Na 1s of NaO_x/SiO_2, b) K 2p of KO_x/SiO_2, c) Cs $3d_{5/2}$ of CsO_x/SiO_2, and d) O 1s of CsO_x/SiO_2.

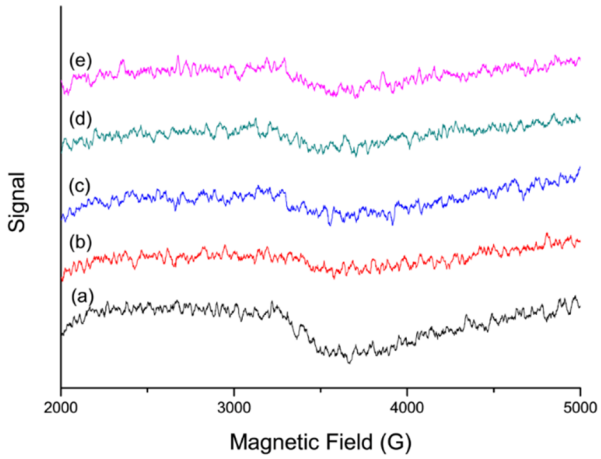

Figure 2-5. ESR spectra of a) NaO_x/SiO_2, b) KO_x/SiO_2, c) CsO_x/SiO_2, d) $10CsO_x/Al_2O_3$-823, and e) $10CsO_x/TiO_2$-823.

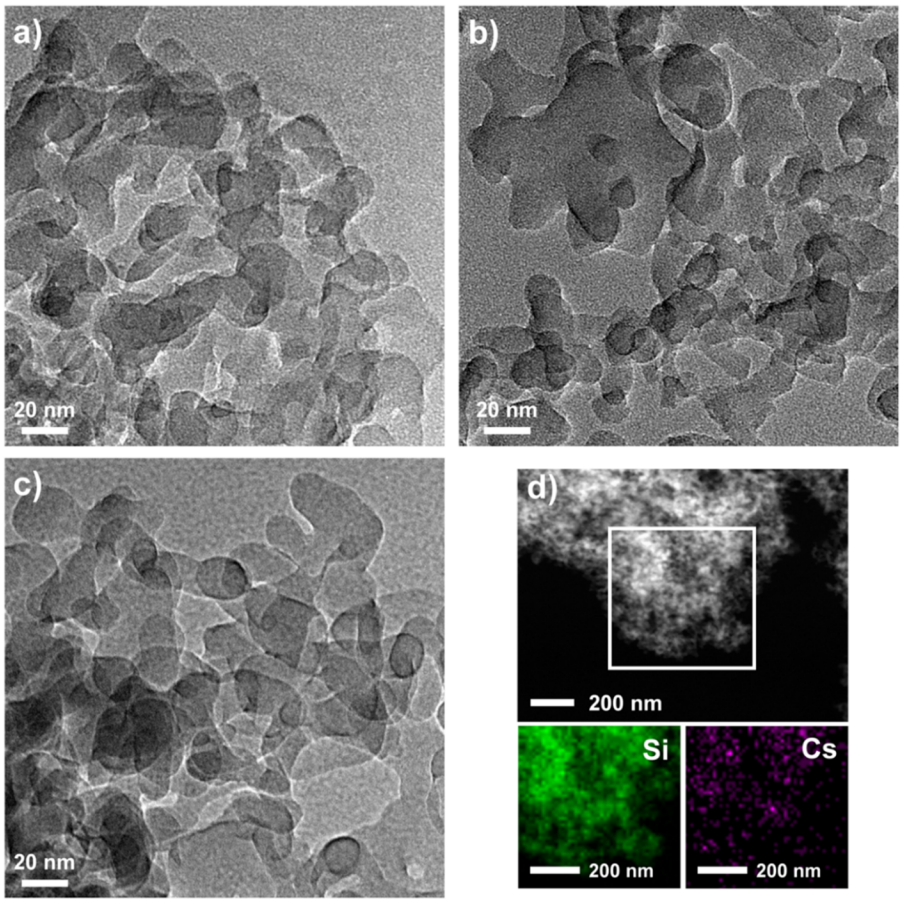

Figure 2-6. HR-TEM images of a) NaO_x/SiO_2, b) KO_x/SiO_2, c) CsO_x/SiO_2, and d) HAADF-STEM image of CsO_x/SiO_2 and their corresponding elemental mapping images of Cs (purple), Si (green).

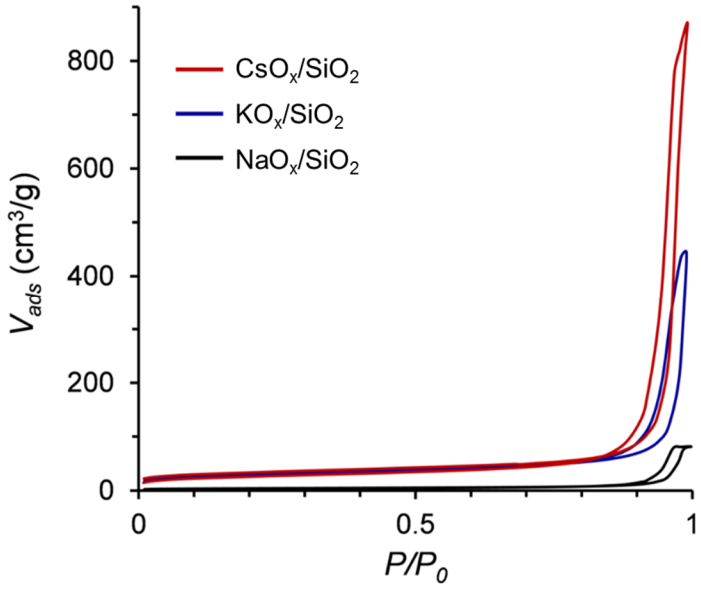

Figure 2-7. Isotherm plots of N_2 adsorption-desorption analyses for the SiO_2 supported alkali metal oxide catalysts.

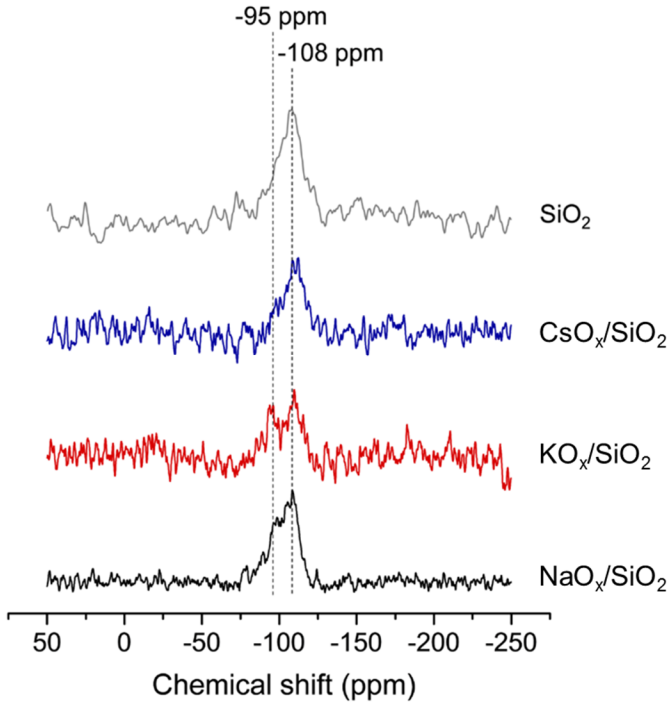

Figure 2-8. ^{29}Si CP/MAS NMR spectra of the SiO_2 supported alkali metal oxide catalysts.

2.3.3 Effect of preparation conditions in CsO_x/SiO_2 catalyst system

To further understand the CsO_x/SiO_2 catalyst system in more detail, I studied the effect of preparation conditions including Cs_2O wt.% loading and calcination temperature on the catalytic performance and the structure of the catalysts (the notation of $xCsO_x/SiO_2$-y is used to express the x wt.% loading of Cs_2O and y K of calcination temperature). Furthermore, a stability test was performed for the optimum catalyst.

2.3.3.1 Cs_2O wt.% loading

Figure 2-9a show the isotherm plots of N_2 adsorption-desorption analyses for the CsO_x/SiO_2 catalysts with different amounts of loaded Cs_2O. With increasing Cs_2O wt.% loading, the specific BET surface area is continuously decreased from 177 m^2/g ($1CsO_x/SiO_2$-823) to 147 ($5CsO_x/SiO_2$-823), 115 ($10CsO_x/SiO_2$-823), and 49 m^2/g ($20CsO_x/SiO_2$-823). Some extent of this decrease in surface area can be attributed to increased amounts of Cs_2O. However, the effective SiO_2 surface area is also decreased (179, 155, 127, and 61 m^2/g for 1, 5, 10, and $20CsO_x/SiO_2$-823, respectively), which indicates that an increase in Cs_2O content significantly influences the structure of the SiO_2 support. In Figure 2-9a, the hysteresis at P/P_0 = 0.7~1.0 shifted to a higher P/P_0 value and is considerably decreased with increasing Cs_2O contents from 10 wt.% to 20 wt.%. This shift means that inter-particular porosity disappears due to agglomeration of SiO_2 particles. In the results of XRD analysis (Figure 2-10), the peak

assigned to amorphous SiO_2 (22°) is shifted to higher angle (24.5° for $20CsO_x/SiO_2$-823), indicating that large Cs atoms are intercalated between SiO_2 particles during the agglomeration process.

The effect of Cs_2O wt.% loading on catalytic activity are shown in Figure 2-11 as a function of the surface density of Cs atoms. The results clearly show an increasing trend of specific activity with decreased surface density. The specific activity was 7.5 h^{-1} at a high surface density of 17 Cs/nm^2 ($20CsO_x/SiO_2$-823), and was increased by 6-fold to 44.2 h^{-1} for 0.24 Cs/nm^2 ($1CsO_x/SiO_2$-823). Importantly, such a high activity at very low surface density indicates that isolated Cs atoms on SiO_2 make up the active center for dehydrative epoxidation. Moreover, the distance between active sites is also a crucial factor for the dehydrative epoxidation, as evidenced by a continuous increase in specific activity with decreasing surface density.

2.3.3.2 Calcination temperature

An increase in calcination temperature at a constant loading of Cs_2O (1 wt.%) also affected the textural properties of the catalysts (Figure 2-10b). Below a calcination temperature of 923 K, the CsO_x/SiO_2 catalysts exhibits similar BET surface areas (174, 177, and 187 m^2/g for 723, 823, and 923 K of calcination temperature, respectively). At a calcination temperature of 1023 K, the catalyst loses surface area significantly (123 m^2/g). This considerable decrease in surface area can be attributed to the condensation of silanol groups as evidenced by differential scanning calorimetry anaylsis (Figure 2-12). An endothermic

region is present in the range of 373 ~ 633 K, which is attributed to the removal of surface adsorbates such as water molecules. In the range of 633 ~ 983 K, the process is exothermic, and can be caused by the oxidation of carbonaceous substances which are produced from acetate groups of the cesium precursor. At temperatures over 983 K, the endothermic process becomes dominant, due to the condensation of silanol groups in the surface of SiO_2 [61, 90]. The XRD patterns of these catalysts were almost identical and were different from the patterns for the catalysts with different Cs_2O loading because only small amounts of Cs_2O (1 wt.%) were loaded.

In Table 2-3 (entry 1-4), the specific activity of the catalysts was considerably affected by a calcination temperature. Although similar specific BET surface area was estimated after the calcination at 723, 823, and 923 K, the specific activity was higher for catalysts prepared at higher temperature. In contrast, the calcination at 1023 K led to a decrease in the catalytic activity of the catalyst ($1CsO_x/SiO_2$-1023). The decreased activity caused by calcination at 1023 K can be attributed to the decreased surface area, which leads to a higher surface density of Cs atoms. On the other hand, an increase in specific activity calcination for 723 ~ 923 K could be related to carbonaceous species which are produced from the cesium precursor. As evidenced by the result of a DSC analysis (Figure 2-12), the oxidation of carbonaceous species is occurred in the range of 633 ~ 983 K. Therefore, carbonaceous species can be removed insufficiently in this range of a calcination temperature. Remained carbonaceous species can cover active sites and thereby can cause a decrease in the catalytic activity.

2.3.3.3 Stability test

Using the optimum catalyst ($1CsO_x/SiO_2$-923), a long-time reaction test was performed to evaluate the stability of the catalyst. The specific activity at initial time (2 ~ 6 h) decreased rapidly from 59.3 h^{-1} to 40.1 h^{-1}. The specific activity then decreased slightly with time, and became constant for 32.7 ~ 35.8 h^{-1} after 13 h of reaction. The rapid decrease in activity at the initial time can be attributed to a decrease in basic sites caused by the leaching of Cs atoms.

Table 2-3 Catalytic performance of the supported cesium oxide catalysts on the dehydration of 2,3-butanediol.[a]

Entry	Catalysts	Surface density (Cs/nm^2)	Specific formation rate (h^{-1})			Specific activity (h^{-1})[b]
			2,3-epoxybutane (**EB**)	3-buten-2-ol (**BO**)	Methyl ethyl ketone (**MEK**)	
1	$1CsO_x/SiO_2$-723	0.24	23.7	8	7.2	31.6
2	$1CsO_x/SiO_2$-823	0.24	34.8	9.4	9.2	44.2
3	$1CsO_x/SiO_2$-923	0.23	47.8	11.5	15.8	59.3
4	$1CsO_x/SiO_2$-1023	0.35	36.2	8.7	9.6	44.8
5	$0.5CsO_x/Al_2O_3$-923	0.32	t.a.	t.a.	126	t.a.
6	$0.25CsO_x/TiO_2$-923	0.59	t.a.	t.a.	292	t.a.
7	$10CsO_x/SiO_2$-823	3.7	10.5	2.6	1.7	13.1
8	$10CsO_x/Al_2O_3$-823	5.1	0.9	0.9	0.9	1.8
9	$10CsO_x/TiO_2$-823	9	1.6	0.6	2.9	2.2

[a] Fixed-bed flow reactor, T_{rxn} = 673 K, SV = 1.38 L/(min (g cat)). [b] Sum of specific formation rate for 2,3-epoxybutane (**EB**) and 3-buten-2-ol (**BO**).

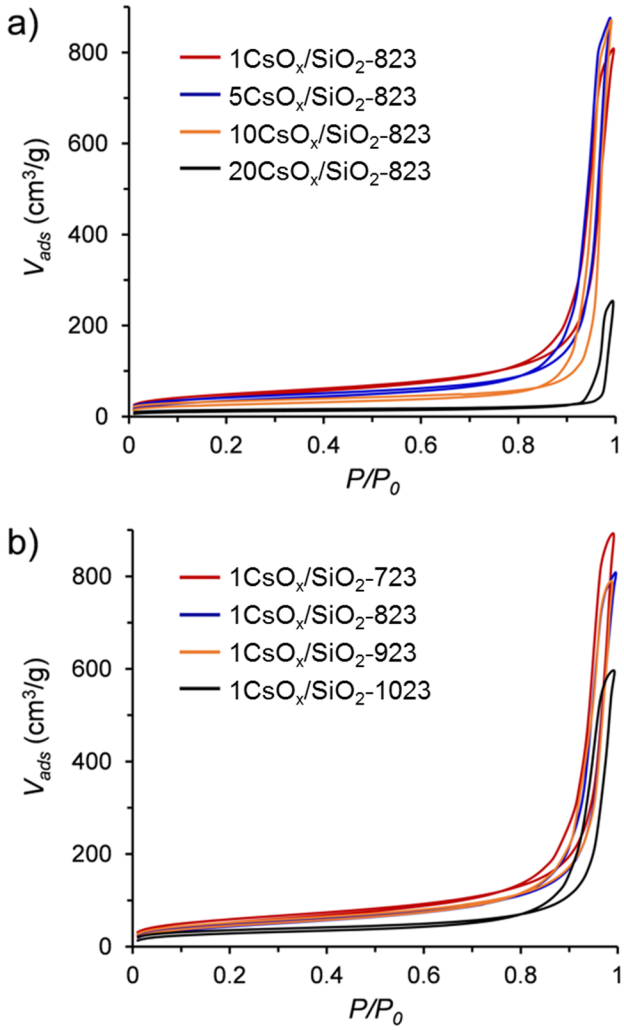

Figure 2-9. Isotherm plots of N_2 adsorption-desorption analyses for the prepared CsO_x/SiO_2 catalysts: a) the catalysts with different Cs_2O wt.% loading calcined at 823 K, b) $1CsO_x/SiO_2$ catalysts calcined at different temperatures.

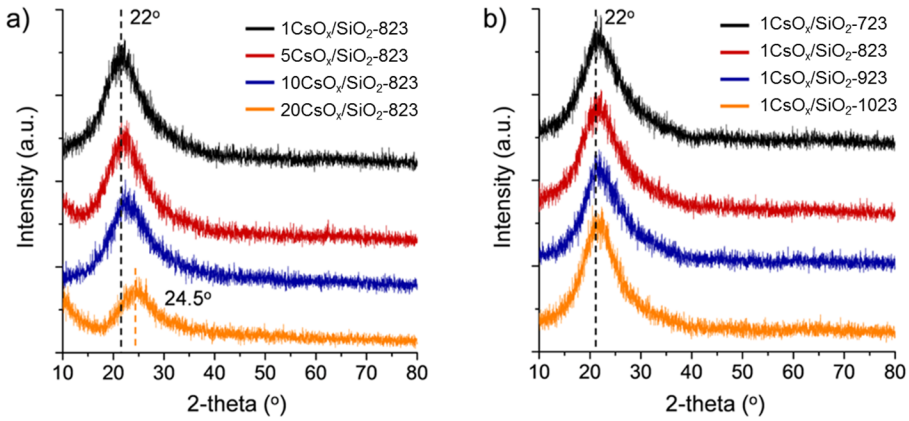

Figure 2-10. XRD patterns of the prepared CsO_x/SiO_2 catalysts: a) the catalysts with different Cs_2O wt.% loading calcined at 823 K, b) $1Cs/SiO_2$ catalysts calcined at different temperatures.

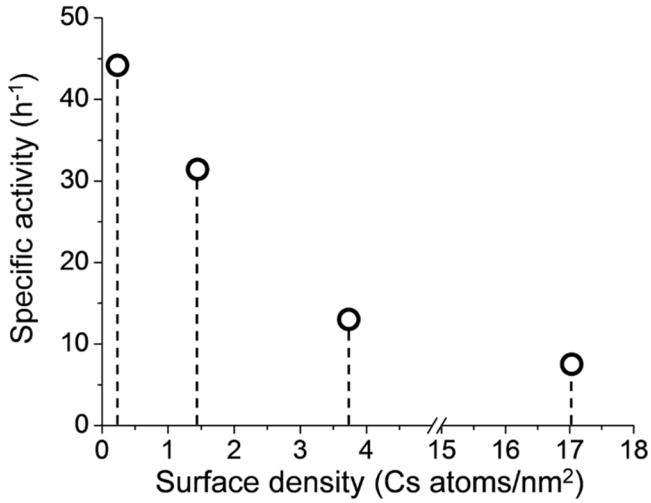

Figure 2-11. The specific activity of the CsO_x/SiO_2 catalysts calcined at 823 K as a function of surface density: $1CsO_x/SiO_2$-823 (0.24 Cs/nm^2), $5CsO_x/SiO_2$-823 (1.45 Cs/nm^2), $10CsO_x/SiO_2$-823 (3.74 Cs/nm^2), and $20CsO_x/SiO_2$-823 (17.0 Cs/nm^2).

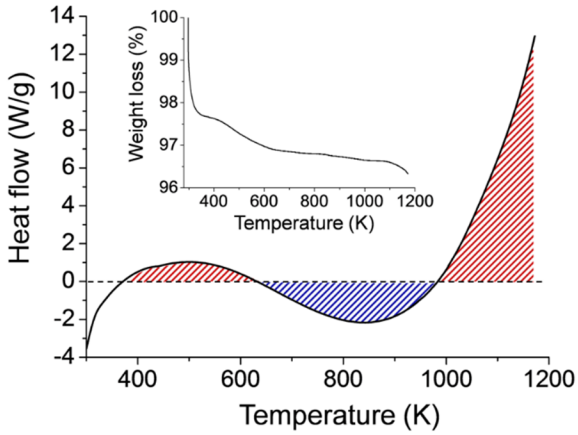

Figure 2-12. Profile for the differential scanning calorimetry analysis of the as-prepared $1CsO_x/SiO_2$. Red and blue stripe zones indicate endothermic and exothermic process, respectively. Inset shows the thermogravimetric data.

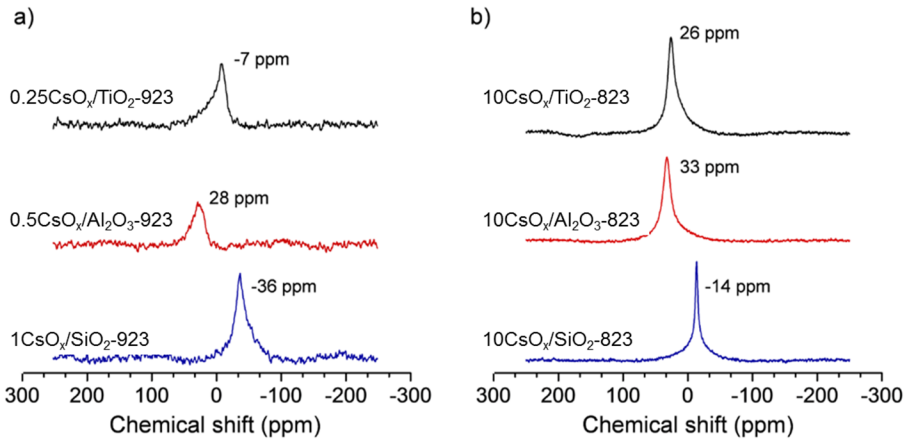

Figure 2-13. ^{133}Cs MAS NMR spectra of the supported cesium oxide catalysts: a) low surface density, b) high surface density.

2.3.4 Effect of support: Significance of the SiO_2 support

The significance of the support in the dehydrative epoxidation was further investigated by a comparison of catalysts using different supports (Al_2O_3 and TiO_2). CsO_x/Al_2O_3 and CsO_x/TiO_2 catalysts were prepared at two different conditions to compare their catalytic activity at low and high surface densities. Similar to the CsO_x/SiO_2 catalyst, Cs atoms were present as Cs^+ The textural properties of the prepared catalysts were characterized by means of N_2 adsorption-desorption, HR-TEM, and XRD analyses. In brief, crystalline cesium oxides were not observed in the catalysts, and the inter-particular porosity of the catalysts were similar (Type IV isotherm and H3 hysteresis loop at P/P0 = 0.8 – 1.0), ensuring that the internal diffusion of reactants was not a determining factor for catalytic activity.

When Al_2O_3 and TiO_2 were utilized as the support instead of SiO_2, the catalytic activity for the dehydrative epoxidation was significantly decreased compared to CsO_x/SiO_2 catalysts (Table 2-3. Entry 3, 5-9). At low surface density, $0.5CsO_x/Al_2O_3$-923 (entry 5) and $0.25CsO_x/TiO_2$-923 (entry 6) produced trace amounts of **EB** and **BO**, as opposed to $1CsO_x/SiO_2$-923. These two catalysts exhibited a considerably high specific formation rate of **MEK** and **IBA**. This rate would be an overestimated value, as the formation of **MEK** and **IBA** can be attributed to the intrinsically reactive sites of Al_2O_3 and TiO_2 rather than the basic sites formed by Cs atoms [91-93]. Moreover, by-products, such as 3-hydroxy-2-butanone, 2,3-butanedione, t-butanol, and 2-butanol were also detected. These products can be formed via a combination of side reactions,

such as dehydrogenation, hydrogenation, and undesired dehydration reactions. For CsO_x/Al_2O_3 and CsO_x/TiO_2 at a high surface density level (entry 8 and 9), the formation of **MEK** and **IBA** was suppressed due to a decrease in the exposed surface of Al_2O_3 and TiO_2, and quantifiable amounts of **EB** and **BO** were produced as well. However, the specific activity was still considerably lower than that for the CsO_x/SiO_2 catalysts.

It appeared that not only the loaded Cs atoms, but the SiO_2 support also plays a crucial role in catalyzing dehydrative epoxidation. This significance of SiO_2 indicates that the properties of a basic site can vary considerably, depending on the support, or another promotional effect of a support occurs. In this regard, the base strength and local environment of Cs atoms in the supported Cs catalysts were compared to determine how strong the influence of a support is on the properties of a basic site.

The base strength of the catalysts were compared by a Hammett indicator titration method. Among the catalysts, $10CsO_x/Al_2O_3$ exhibited the strongest base strength of $H_- > 15.0$. Other catalysts showed the comparable base strength of $8.2 < H_- < 15.0$, except for $0.25CsO_x/TiO_2$-923 that the base strength was determined to be $6.8 < H_- < 8.2$. The results indicate that the base strength can be considerably affected by the type of support.

The local structure of Cs^+ on the supported cesium oxide catalysts was examined by ^{133}Cs MAS NMR spectroscopy. At a low surface density (Figure 2-13a), Cs atoms in $1CsO_x/SiO_2$ are more negatively shielded (-36 ppm) than those in $0.5CsO_x/Al_2O_3$ (28 ppm) and $0.25CsO_x/TiO_2$ (-7 ppm). This order of chemical shift is also observed for the catalysts with a high surface density

(Figure 2-13b), but the characteristic peak was slightly shifted to a positive value (-14, 33, and 26 ppm for $10CsO_x/SiO_2$, $10CsO_x/Al_2O_3$, and $10CsO_x/TiO_2$, respectively). The values of the chemical shift for the CsO_x/SiO_2 and CsO_x/Al_2O_3 catalysts are similar to the reported values of Cs^+ exchanged silicate and boehmite [69]. It is important to note that the chemical shift is closely related to the interaction between Cs^+ and surface oxygen, the extent of which becomes stronger for a more negative chemical shift. Therefore, the more shielded (negative) chemical shift for CsO_x/SiO_2 catalysts indicates that Cs^+ in CsO_x/SiO_2 is more tightly bonded to surface oxygen than Cs^+ in CsO_x/Al_2O_3 and CsO_x/TiO_2. In addition, the positive shift for a high surface density means that the interaction is weakened when the distance between Cs atoms becomes shorter. Since the ionic radius of cesium is large (181 pm), Cs^+ which is weakly bonded to the surface would hinder the adsorption of reactant molecule on surface basic sites, resulting in a decreased activity. In addition, Cs^+ can be unstable when reaction conditions involve water molecules due to rapid leaching [69]. The variation in chemical shift for different supports can be attributed to the surface charge of the supports. The point of zero charge (PZC) for Al_2O_3 (Aeroxide® AluC) and TiO_2 (Aeroxide® P25) is 9 and 6.4, respectively, and these values are considerably higher than the 2.7 of PZC for SiO_2 (Aerosil® 200) [94]. The higher PZC value for Al_2O_3 and TiO_2 means that a less negative surface charge is present, which can result in weaker interactions between Cs^+ and surface oxygen atoms. This trend in PZC values is also in agreement with the trend for chemical shifts.

Based on these results, the type of support can have an effect on base strength, accessibility of basic sites, and stability of Cs^+ ions. However, the results do not clearly explain the extraordinary effect of SiO_2 support because base strength of $10CsO_x/Al_2O_3$ is stronger than that of CsO_x/SiO_2 catalysts, and the extent of difference in the local environment of Cs^+ ion does not appear to be so significant. Hence, there would be other promotional function of SiO_2 support that makes CsO_x/SiO_2 outstanding in the dehydrative epoxidation. The promotional function of the SiO_2 support is further discussed in section 2.3.6.3, based on the results of DFT calculations.

2.3.5 Stereochemistry in the dehydrative epoxidation

The *cis*/*trans* ratio of epoxide **EB** in the products presents an important stereochemical footprint during the dehydrative epoxidation. In our experiments, a mixture of isomers of **BD** was used (*meso*: 77%, *racemic*: 23%), and the *trans*-**EB** was dominant in the products (Figure 2-14a). For precise information, pure *meso*-2,3-butanediol (**mBD)** was utilized as a reactant, and thereby the proportion of *trans*-**EB** increased to 96% from 80% for the mixed isomers of **BD**. Based on these results, it appears that the **mBD** is selectively converted to *trans*-**EB** via the dehydrative epoxidation. Similarly, *cis*-**EB** could be derived from *racemic*-2,3-butanediol (**rBD**) as well. This indicates that the reaction is stereoselective or stereospecific since configuration of one chiral center is inverted ((*R,S*) of **mBD** to (*S,S* or *R,R*) of *trans*-**EB**, and (*S,S* or *R,R*) of **rBD** to (*R,S*) of *cis*-**EB)**.

Regarding the conformations and related energies of **mBD**, it was reported that a *gauche*-arrangement of O-C-C-O (*gauche*-**mBD**) is much favored in the gas phase over the anti-arrangement (*anti*-**mBD**) due to the stabilization by intramolecular hydrogen bonding and/or so called "*gauche* effect" [95]. Comparing the dihedral angle of the C-C-C-C for diol **mBD** and epoxide **EB**, the structure of *gauche*-**mBD** is similar to that of *cis*-**EB** rather than *trans*-**EB**. In order to have the selective conversion of stable *gauche*-**mBD** to *trans*-**EB**, the dehydrative epoxidation of **mBD** should involve a rotation on the C_2-C_3 axes of the molecule during the reaction.

There are three possible paths for the selective conversion with *gauche*-**mBD**: A rotation followed by dehydration, simultaneous rotation and dehydration, and dehydration followed by rotation (Figure 2-14b. path 1, path 2, and path 3, respectively). Feasibility of each path was examined by DFT calculations and is discussed below. In addition, the path 3 was verified experimentally to be infeasible as a reaction of *cis*-**EB** produced negligible quantity of *trans*-**EB** (1% yield).

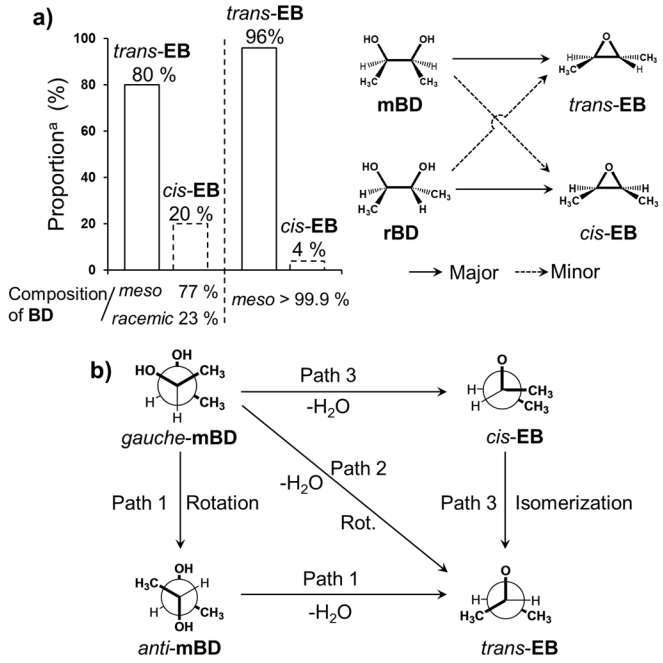

Figure 2-14. a) Conformational effect of the reactant on the dehydration of 2,3-butanediol **BD**, b) Possible paths for selective formation of *trans*-**EB** from *gauche*-**mBD**.

2.3.6 Mechanism of the dehydrative epoxidation reaction

To further understand the dehydrative epoxidation and its reaction mechanism, DFT calculations were performed on the model surface of CsO_x/SiO_2 catalyst. In this investigation, the stereochemistry in the dehydrative epoxidation was considered.

2.3.6.1 DFT calculations: meso-2,3-butanediol in the gas-phase and in the adsorption on the model surface of CsO_x/SiO_2

DFT calculations were performed at the PBE-D2 level of theory. In order to model the surface of the CsO_x/SiO_2, a SiO_2 surface was first constructed based on previous reports [64,96-98] and Cs ion was then exchanged with proton of surface silanol group. The site of exchange plays the role of a basic site (O_{base}). For efficient calculations, the surface density of 1.0 Cs/nm^2 was utilized instead of the value for the optimum catalyst (0.24 Cs/nm^2 for $1CsO_x/SiO_2$-923). Detailed descriptions of the modelled CsO_x/SiO_2 surface are shown in Figure 2-15. Table 2-4 summarizes relative energies and important geometrical parameters obtained from the DFT calculations.

The gas-phase structures of **mBD** with different conformations were optimized and the activation barrier for the rotation of *gauche*-**mBD** to *anti*-**mBD** was calculated. The structure of *gauche*-**mBD** is quite similar to that of previous reports [95] which showed the existence of intramolecular hydrogen bonding between adjacent hydroxyl groups. This intramolecular hydrogen bonding is not present in the structure of *anti*-**mBD**. For this reason, *gauche*-

mBD is more stable than *anti*-**mBD** (9 kJ/mol). It was reported that *gauche*-**mBD** exclusively presented in the gas-phase about 90% at a temperature of 298 K due to this difference of energy [95]. In order to have a rotation from the most stable *gauche*-**mBD** to *anti*-**mBD**, somewhat high energy barrier of 22 kJ/mol is required.

Through the systematic screening of the surface adsorption sites for *anti*-**mBD** and *gauche*-**mBD**, the most stable adsorption geometries for *anti*-**mBD** and *gauche*-**mBD** were found (Figure 2-16). It is important to note that the presence of interactions between H_α and O_{base} site has a considerable effect on the adsorption energy of the molecule. When the interaction between H_α and O_{base} is absent, the adsorption is weakened and the adsorption energy changes up to –61 kJ/mol. Therefore, the basic site (O_{base}) is a major adsorption site on the CsO_x/SiO_2 catalyst. The adsorption energies (ΔE_{ads}) for *anti*-**mBD** and *gauche*-**mBD** were –118 kJ/mol and –158 kJ/mol, respectively. Therefore, *gauche*-**mBD** is energetically favored over *anti*-**mBD** in the adsorption on CsO_x/SiO_2 surface as well as in the gas-phase. The stronger adsorption of *gauche*-**mBD** can be primarily attributed to the larger extent of hydrogen bonding with the surface. In case of the *gauche*-**mBD** adsorption, O_α–H_α is adsorbed on O_{base} site with hydrogen bonding (O_{base}---H_α, 1.72 Å), and another O_β-H_β site enters into two types of hydrogen bonding situations with H_{Si} and O_{Si} (O_β---H_{Si}, 1.55 Å; O_{Si}---H_β, 1.66 Å). In contrast, the adsorption of *anti*-**mBD** is only involved in two hydrogen bonding situations with the CsO_x/SiO_2 surface (O_{base}---H_α, 1.63 Å; O_β---H_{Si}, 1.60 Å). The fact that the *anti*-arrangement is intrinsically less stable

than *gauche*-arrangement in the gas-phase (9 kJ/mol) is also one reason for the smaller adsorption energy of *anti*-**mBD**.

The adsorption geometries of **mBD** allude the expected role of basic site as well as importance of surface hydroxyl site on dehydrative epoxidation. In the geometries, the bond lengths of O_{α}-H_{α} and C_3-O_{β} are slightly elongated upon the adsorptions (Table 2-4), which means that the strength of those bonds are weakened.

Table 2-4 Relative energies and structural parameters for the optimized geometries of the molecules in gas phase, the adsorption, and the transition states of the reaction. Calculations were performed at the PBE-D2 level of theory.

Model	Molecule	ΔE^a / kJ/mol	Dihedral angle[b] (O_α-C_2-C_3-O_β)	Dihedral angle[b] (C_1-C_2-C_3-C_4)	Hydrogen bonding and bond length[c] / Å				
					O_{base}-H_α	O_β-H_{Si}	O_{Si}-H_β	O_α- H_α	C_3-O_β
Gas phase	*gauche*-**mBD**	0	61°	60°	-	-	-	-0.97	-1.43
	anti-**mBD**	9	180°	178°	-	-	-	-0.97	-1.44
	cis-**EB**	105	-	0°	-	-	-	-	-
	trans-**EB**	94	-	152°	-	-	-	-	-
Adsorption	*gauche*-**mBD**	-158	65°	61°	1.72	1.55	1.66	-1	-1.44
	anti-**mBD**	-118	163°	164°	1.63	1.6	-	-1.02	-1.46
	cis-**EB**	-57	-	1°	-	1.56[d]	-	-	-
	trans-**EB**	-68	-	154°	-	1.58[d]	-	-	-
Transition States	TS1	42 (160)	(162°)	152°	-1.14	-1.06	-	1.3	2.14
	TS2	134 (292)	(92°)	105°	-1.05	-1.03	2.13	1.55	2.56
	TS3	118 (276)	(27°)	7°	2.71	1.67	1.58	1.7	2.38

[a] Energies relative to *gauche*-**mBD** in gas phase and bare surface of CsO_x/SiO_2 (ΔE_{ads} for adsorption). Values in parentheses for transition states are activation energies (ΔE_A). [b] Numbering of carbon is denoted from left to right. O_α and O_β indicate hydroxyl oxygen atoms of 2,3-butanediol. [c] Hydrogen bonding length is noted without parentheses, and chemical bond length is given in parentheses. [d] Distance between O_α and H_{Si1}.

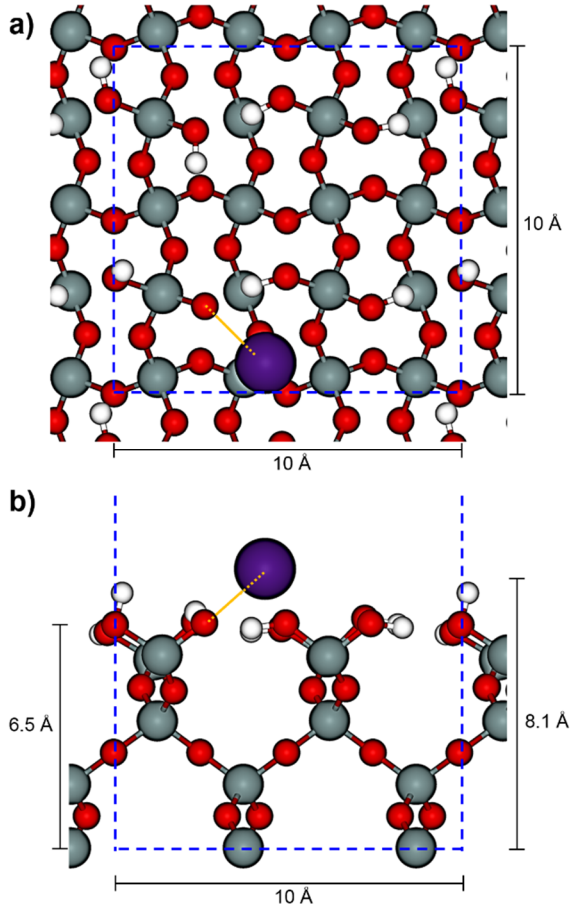

Figure 2-15. Periodic supercell of CsO_x/SiO_2 model surface. Blue dotted line indicates periodic boundary of the system. Bond distance between O_{base} and Cs^+ (represented by orange line) is 2.88 Å, which is quite similar value with experimental distance of Cs-O (2.86 Å) in Cs_2O [78].

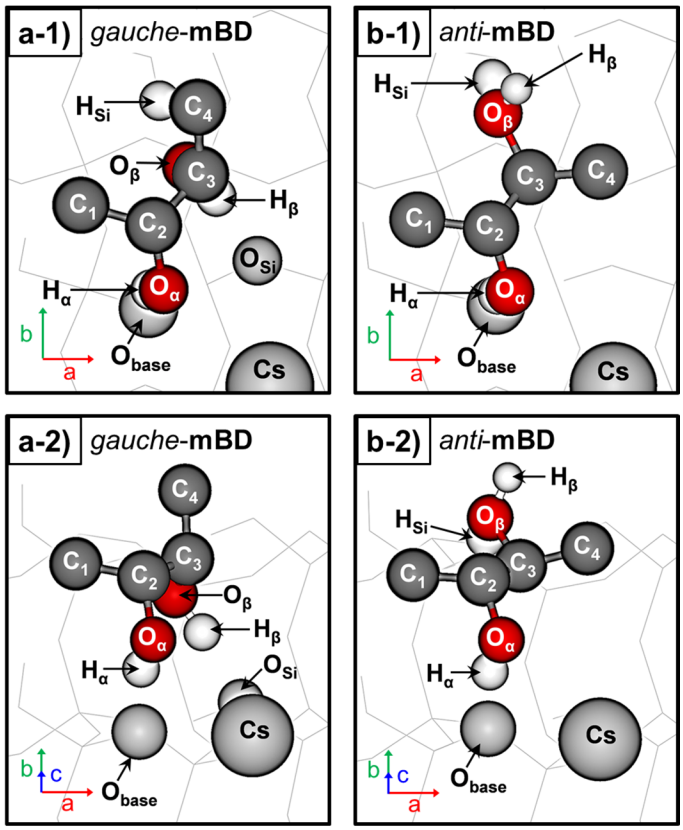

Figure 2-16. The most stable geometries for the adsorption of *gauche*-**mBD** (a-1, top view; a-2, rotated view) and *anti*-**mBD** (b-1, top view; b-2, rotated view) on the model surface of CsO_x/SiO_2. Hydrogen atoms attached to carbon atoms are not present for a clear description. O_{base}, H_{Si}, and O_{Si} represent basic site, silanol proton, and surface oxygen of SiO_2, respectively. O_α-H_α and O_β-H_β indicate hydroxyl groups of **mBD**. Calculations were performed at the PBE-D2 level of theory.

2.3.6.2 DFT calculations: Clarification of the mechanism for the dehydrative epoxidation of 2,3-butanediol

Figure 2-17 presents transition state structures for the dehydrative epoxidation of **mBD** with different conformational changes and a relative energy diagram over reaction coordinates. The three calculated transition states (Figure 2-17a, b, and c) correspond to the dehydration reaction of the paths in Figure 2-17b (path 1, path 2, and path 3, respectively. They are briefly summarized at the top of Figure 2-17).

Considering the energy diagram at initial stage of reaction coordinate (Figure 2-17d), the path 1 is relatively unfavorable than the other paths because of the required energy for the rotation from *gauche*-**mBD** into *anti*-**mBD** (22 kJ/mol) and relatively unstable geometries for *anti*-**mBD** (values for energy difference between *anti*-**mBD** and *gauche*-**mBD** are 9 and 40 kJ/mol in the gas phase and in the adsorption, respectively). However, the activation barrier (ΔE_A) for TS1 (160 kJ/mol) in the path 1 is significantly lower than that for TS2 (292 kJ/mol) and TS3 (276 kJ/mol). It is important to note that the difference in ΔE_A (TS1 vs. TS2 and TS3) is much larger than the difference between *anti*-**mBD** and *gauche*-**mBD** in the gas phase and in the adsorption. Therefore, the path 1 is the energetically most probable path for the dehydrative epoxidation although adsorption geometry for *gauche*-**mBD** is more stable than that for *anti*-**mBD**. These results explain why the dehydrative epoxidation of **mBD** selectively produces *trans*-**EB**.

When the transition state structure is considered for the most probable path (TS1, Figure 2-17a), it is found that surface hydroxyl site of SiO_2 is involved to produce H_2O during the dehydrative epoxidation. In the structure, the silanol hydrogen (H_{Si}) is transferred to the O_β-H_β hydroxyl group, resulting in the elimination of H_2O from *anti*-**mBD**. Simultaneously, the O_{base} accepts the H_α, making the O_α nucleophilic prior to forming an epoxide ring. Hence, the structure indicates that both the surface hydroxyl site and the basic site are required for the dehydrative epoxidation of **mBD**. As similar to the structure of TS1, the transition state structure in path 2 (Figure 2-17b. TS2, *gauche*-**mBD** to *trans*-**EB**) also showed the involvement of the silanol hydrogen (H_{Si}) in the elimination of H_2O. However, the distortion of carbon backbone is quite different in this case. Dihedral angle of C_1-C_2-C_3-C_4 in TS1 is 152°, which is almost identical to that for *trans*-**EB** (152° in gas-phase, 154° after adsorption). In contrast, the dihedral angle in TS2 is 105.0° which is significantly distorted from the value for *trans*-**EB**. Single point calculations on the organic molecules in TS1 and TS2 estimates the extent of distortion at 77 kJ/mol. This value is comparable to 92 kJ/mol for the difference in transition state energy ($E_{TS2} - E_{TS1}$), which indicates that the distortion in the organic molecule is a major contributor to the higher activation barrier of TS2. As opposed to TS1 and TS2, the participation of a silanol hydrogen did not occur in the transition state structure of path 3 (Figure 2-17c TS3, gauche-**mBD** to cis-**EB**). H_α is directly transfered to the O_β-H_β hydroxyl group, leading to the elimination of H_2O.

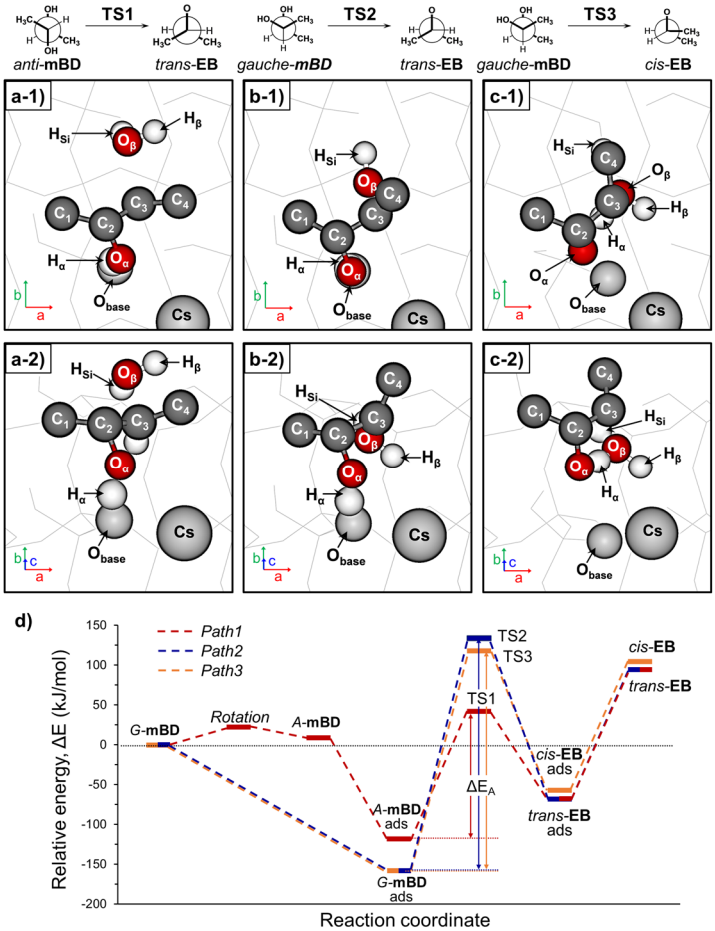

Figure 2-17. Transition state structures of *anti*-**mBD** to *trans*-**EB** (a-1. top view; a-2. rotated view), *gauche*-**mBD** to *trans*-**EB** (b-1. top view; b-2. rotated view), and *gauche*-**mBD** to *cis*-**EB** (c-1. top view; c-2. rotated view); Hydrogen atoms attached to carbon atoms are not present for a clear description. d) Total energy diagram for the dehydrative epoxidation of **mBD** over the model surface of CsO_x/SiO_2. (*anti*-, *gauche*-, adsorption, and transition state are shortened as *A*-, *G*-, ads, and TS, respectively). Calculations were performed at the PBE-D2 level of theory.

2.3.6.3 Discussion.

In the optimized adsorption geometries and transition state structure from the DFT calculations, it was found that not only the basic site, but also the surface hydroxyl site of the support are involved in dehydrative epoxidation. Importantly, the involvement of the surface hydroxyl site could explain the promotional effect of the support discussed in section 3.4. The proton in the hydroxyl site participates in the elimination of H_2O, indicating that the acidity of the proton could be important in this function. In this regard, the point of zero charge (PZC) of support is closely related to the acidity of protons of surface hydroxyl sites as the surface charge of oxides can typically change by the gain and loss of a proton. A low PZC means that the surface of the oxide favors a negatively charged state by losing its proton. Therefore, since the PZC of SiO_2 is lower (2.7), the surface hydroxyl site of SiO_2 would contain a more acidic proton than Al_2O_3 and TiO_2 (PZC = 9 and 6.4, respectively) and could be more effective in terms of the elimination of H_2O. It is noteworthy that the trend in PZC values of the supports is consistent with the trend for specific activity among $10CsO_x/SiO_2$-823, $10CsO_x/Al_2O_3$-823, and $10CsO_x/TiO_2$-823. Based on these results, it can be concluded that the promotional effect of the support originates from the role of the surface hydroxyl site in the elimination of H_2O, and the relatively higher acidity of protons in the surface hydroxyl sites of the SiO_2 support contributes the outstanding performance of CsO_x/SiO_2 on the dehydrative epoxidation.

On the basis of experimental data and DFT calculations, an S_N2-like

mechanism for dehydrative epoxidation of **mBD** is proposed (Scheme 2-2). The dehydrative epoxidation of **mBD** results in the selective formation of *trans*-**EB**, since the reaction with the conformational change of **mBD** in an *anti*-arrangement of O-C-C-O to *trans*-**EB** has a considerably lower activation barrier than the other conformational change. In this conformational change, the chirality of the carbon from which the hydroxyl group is eliminated is inverted by the backside attack of an anionic oxygen ((*R,S*) of **mBD** to give (*R,R*) of *trans*-**EB** in this model case). This inversion is quite similar to that for an S_N2 type of substitution reaction [95] and suggests that the reaction is stereospecific. The mechanism of the dehydrative epoxidation is quite different from typical dehydration reactions which proceed via an elimination mechanism (E1, E2) [100]. The dehydrative epoxidation of other vicinal diols could occur in a manner similar to that for **mBD**. The sequence of the proposed mechanism is analogous to that for the dehydration of monoethanolamine to ethyleneimine which involves both weak acid and basic sites [73]. However, the higher basicity of the $-NH_2$ group in monoethanolamine would make the reaction easier to be induced, even by SiO_2, thus making it different from dehydrative epoxidation.

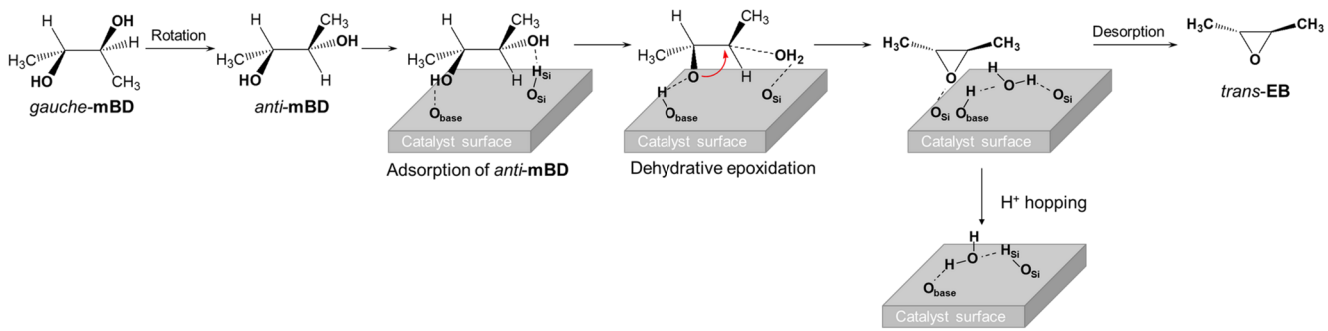

Scheme 2-2. The proposed mechanism for the dehydrative epoxidation of *meso*-2,3-butanediol: S_N2-like stereospecific production of *trans*-2,3-epoxybutane via cooperative catalysis of the basic site and the nearby hydroxyl (silanol) site.

2.3.7 Conversion of 2,3-epoxybutane into 1,3-butadiene

2.3.7.1 Precursor for 1,3-butadiene production

Compared to the products from acid catalyzed dehydration of **BD** (i.e. **MEK** and **IBA**), **EB** is much reactive due to the presence of epoxide ring. This reactivity can provide the chance for further dehydration into 1,3-butadiene. However, reaction of **EB** over acidic Al-MCM-41 catalyst resulted in dominant formation of **MEK** and showed low selectivity toward 1,3-butadiene (19% yield at total conversion, Figure 2-18). On the other hand, **BO** which is isomerized product of **EB** was very attractive precursor as high 1,3-butadiene yield of 97% was achieved with this reactant. Based on these results, **EB** itself is not suitable precursor for the production of 1,3-butadiene, and the isomerization of **EB** to **BO** is essential prior to the subsequent dehydration.

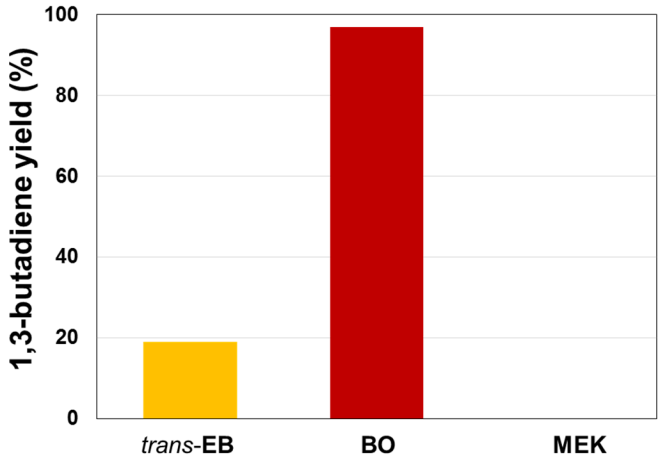

Figure 2-18. Results for reaction of *trans*-**EB**, **BO**, and **MEK** over acidic Al-MCM-41 catalyst. Reaction condition: Fixed-bed flow reactor, T_{rxn} = 523 K for *trans*-**EB** and **BO**, 623 K for **MEK**, SV = 1.38 L/(min (g cat)).

2.3.7.2 Isomerization of 2,3-epoxybutane to 3-buten-2-ol

Basic lithium phosphate (Li_3PO_4) was utilized as an catalyst for the isomerization of **EB** to **BO**. This catalyst was previously utilized in the isomerization of propylene oxide into allyl alcohol [19], which process is analogous to the isomerization of **EB** to **BO**.

Reaction results using *cis*-**EB** and *trans*-**EB** are shown in Figure 2-19. Both the *cis*- and *trans*-**EB** were selectively converted to **BO**, but the use of *trans*-**EB** resulted in a more selective reaction (92, 75 % for *trans*-**EB** and *cis*-**EB**, respectively). In the case of *trans*-**EB** isomerization, **BO** was major product and **MEK** was minor product. In contrast, the reaction of *cis*-**EB** produced *trans*-**EB** and **rBD** as well as **BO** and **MEK**. This difference between *cis*- and *trans*-**EB** could be caused by relative stability of **EB** molecule. In the selction 2.3.5, it was found that *trans*-**EB** is more energetically stable than *cis*-**EB** (11 kJ/mol). Therefore, at certain transition state, *cis*-**EB** can isomerize to *trans*-**EB** spontaneously, but *trans*-**EB** cannot.

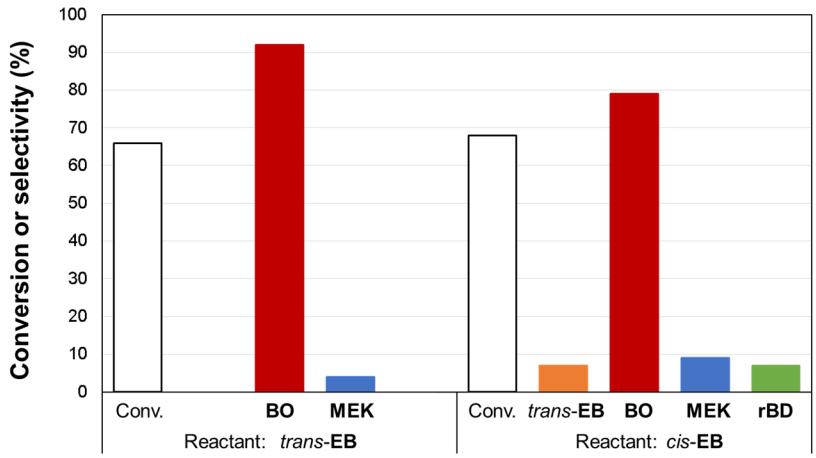

Figure 2-19. Resultis for reaction of *trans*-**EB** (left) and *cis*-**EB** (right) over basic lithium phosphate catalyst. Reaction condition: Fixed-bed flow reactor, T_{rxn} = 623 K, SV = 1.38 L/(min (g cat)).

2.3.8 Heterogeneous catalytic process for the production of 1,3-butadiene

On the basis of this study, heterogeneous catalytic process is proposed as Scheme 2-3. At the first reactor, the dehydrative epoxidation of **BD** over CsO_x/SiO_2 catalyst produces **EB** and **BO** with high selectivity. Since the boiling point (BP) of **BD** (184 ºC) is considerably higher than **EB**, **BO**, and **MEK** (55, 97, and 80 ºC, respectively), unreacted 2,3-butanediol could be easily recovered. **EB** in the low BP products is further isomerized to **BO** at the second reactor. The downstream of the second reactor contains **EB**, **BO**, and **MEK**. As difference in BP between **EB** and **MEK** is higher than that between **BO** and **MEK**, separating **EB** from the downstream is easier to be carried out. The separated **EB** is recycled to the second reactor, and **BO** is further dehydrated into 1,3-butadiene at the third reactor. The produced 1,3-butadiene has considerably low boiling point of -4.5 ºC, thus separation between 1,3-butadiene and **MEK** could be easily undertaken.

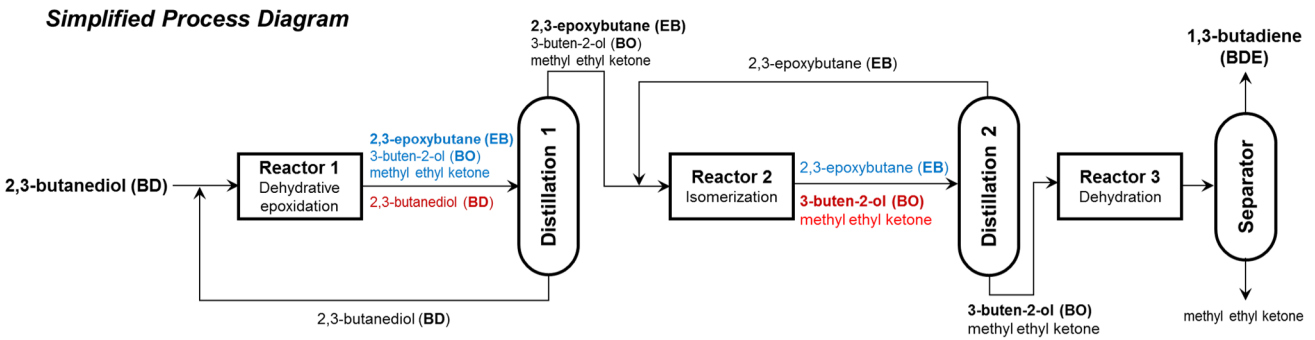

Scheme 2-3. The proposed process diagram for the heterogeneous catalytic conversion of 2,3-butanediol to 1,3-butadiene.

Chapter 3. Mesoporous Solid Acid Catalyst for the Esterification of 1-butanol with Acetic Acid

3.1 Introduction

The development of new solid acid catalysts has been essential in terms of replacing conventional homogeneous catalysts which are not only harmful to the environment, but also cause process problems [102]. A number of solid acids have been examined for this purpose, but all have certain limitations. For example, the small pores (< 2 nm) of zeolites make them difficult to use in reactions that involve the use of high molecular weight components. Sulfated zirconia catalysts, well known superacids, become deactivated during reactions, with the release of volatile sulfur-containing pollutants [103,104]. Solid acids based on supported metal oxides are potential candidates for replacing conventional mineral acids and chlorided Pt/Al_2O_3, which are harmful to the environment [105]. Among these types of catalysts, tungstated zirconia (WO_x/ZrO_2) catalysts have attracted interest, since Hino and Arata first discovered their strong acidity and low-temperature activity for light alkane isomerization [43]. It has been reported to have a high activity for alkane isomerization and the dehydration of alcohols [44-46]. The higher thermal and chemical stabilities of WO_x/ZrO_2 make them attractive for use in a variety of industrial processes [43,46]. They have the potential for use in commercial processes, including the selective catalytic reduction of NO_x to N_2, the

formation of xylene from toluene and methanol, and the oligomerization of lower molecular weight alkanes to gasoline, diesel and lubricants [106-109].

Not only the application of WO_x/ZrO_2 catalysts, but also the origin of their activity has been investigated by various characterization methods. Many investigators have attempted to find correlations between the structure of tungstate and catalytic activity [44,46,110-122]. Several proposed models and general surface species, including monotungstate, polytungstate and crystalline WO_3 have been proposed. The proposed active sites are as follows: i) slightly reduced polytungstate formed in-situ generated strong acid sites during reactions [44,111-113,138,139], ii) a balance between strong Brønsted acidity and Lewis acidity is required for a high activity [46,116,117], iii) zirconium incorporated tungstate clusters formed on WO_x/ZrO_2 produce charge compensating protons as strong Brønsted acids [110,114,115,120-122]. Regardless of the proposed models, it is generally accepted that the strong acidity is due to the strong interaction between zirconia and tungstate or by the presence of Zr-WO_x clusters. However, even though extensive research into the active site has been reported, methods for improving the activity of WO_x/ZrO_2 catalysts are generally not available. In addition, the low surface area of ZrO_2 (< 100 m^2/g) is a disadvantage in catalytic reactions, especially liquid phase reactions.

In order to improve WO_x/ZrO_2 catalysts, ordered mesoporous Zr-WO_x/SiO_2 with a high surface area and a high density of Zr-WO_x clusters is prepared. To optimize the density of the Zr-WO_x clusters, the Zr/W ratio was varied to control the tungstate species on the catalysts. Using this procedure it was

possible to investigate not only the enhanced population of Zr-WO_x clusters, but also to obtain quantitative information, which results in a better understanding of the catalysts. The structure of the tungstate present on the prepared catalysts was characterized using a variety of characterization methods. Qualitative and quantitative data of acidity were collected to find the influence of the structure of tungstate, especially Zr-WO_x clusters. Finally, the performance of the materials as an acid catalyst was examined for the esterification of 1-butanol with acetic acid and the results were compared with conventional solid acids.

3.2 Experimental

3.2.1 Preparation of mesoporous Zr-WO_x/SiO_2

Sodium tungstate dihydrate ($Na_2WO_4•2H_2O$), zirconium butoxide solution ($Zr(OC_4H_9)_4$), tetraethyl orthosilicate (TEOS) were purchased from Sigma-Aldrich; and hydrochloric acid (35-37%) was purchased from Samchun chemical.

To facilitate the formation of Zr-WO_x clusters, the sequential hydrolysis of zirconium and tungsten was introduced to the preparation procedure. A typical Zr-WO_x/SiO_2 synthesis was as follows: P123 (3.26 g, 0.562 mmol) was dissolved in H_2O (100 ml, 5.56 mol) and stirred until a clear solution was obtained. HCl (8.6 ml, 0.089 mol) was then added to the solution. A zirconium butoxide ethanol solution (v/v=1) was added dropwisely to the solution with vigorous stirring. Due to the rapid hydrolysis and condensation of zirconium butoxide in water, a white precipitate was formed immediately and gradually disappeared with stirring. After the solution became clear, an aqueous solution of sodium tungstate (3 ml) was added dropwisely and the solution stirred for 1h to insure the formation of pre-Zr-WO_x clusters. To obtain the same weight percent of tungstate (30 wt%) with different Zr/W ratio, amount of $Zr(OC_4H_9)_4$ and $Na_2WO_4•2H_2O$ were adjusted to 0~4.48 mmol and 3.47~4.48 mmol, respectively. TEOS (6.9 ml, 31 mmol) was then introduced and heated at 40 ^oC for 24 h with stirring. Subsequently, hydrothermal treat was carried out at 100 ^oC for 24 h without stirring. Resultant precipitate was filtered and washed by

ethanol and de-ionized water several time to remove sodium ion and remained acid. The filtered precipitate was dried at 80 ºC overnight and then calcined at 550 ºC for 3 h. The catalysts are denoted simply as 'WZrX', where X indicates the atomic amount of Zr relative to 10 W atoms (i.e. WZr1, atomic ratio of Zr/W=1/10).

3.2.2 Characterization

The N_2 physisorption were carried out on a Micrometrics ASAP-2010 system. The total surface area of the samples was calculated by the BET method (P/P_o=0.1~0.2). The pore volume and pore size distributions were obtained from the desorption branches of the isotherms using BJH methods. High resolution transmission electron micrograph (HR-TEM) images were obtained on a JEOL JEM-3010 microscope using bright field (BF) mode with an acceleration voltage of 300 kV. The X-ray diffraction (XRD) patterns were measured by a Rigaku D-MAX2500-PC powder X-ray diffractometer with Cu Kα radiation (1.5406 Å) in an operating mode of 50kV and 100mV.

X-ray photoelectron spectroscopy (XPS) spectra were recorded using a KRATOS AXIS electron spectrometer equipped with MgKα radiation. All of the binding energy of the peaks was referred to the C1s at 284.6 eV. Binding energies were reported within an experimental error of ±0.2 eV. Ultraviolet-visible (UV-Vis) spectra were recorded with a Jasco V670 spectrometer with diffuse reflectance spectroscopy (DRS) unit. The powdery sample was loaded into a quartz cell, and spectra were collected at 200-1000 nm referenced to KBr.

NH_3 temperature programmed desorption (TPD) was carried out using Micrometrics Autochem II chemisorption analyzer. Prior to the analysis, a 0.1g of sample was treated at 400 ^oC for 1h under a He flow. After cooling to 50 ^oC, the sample was saturated by treatment with a 10.2% NH_3/He flow. The physisorbted NH_3 was eliminated by flushing with a stream of He at 100 ^oC. After cooling to 50 ^oC, the TCD signal was recorded while the temperature was increased to 600 ^oC at a rate of 10 ^oC/min under a flow of He. In-situ FTIR spectra of NH_3 adsorption were measured with a Midac spectrometer (model 2100). A self-supported pellet containing about a 50 mg sample was placed in an In-situ IR cell, designed by Moon et al.[123] The pellet was pretreated at 250 ^oC under a He flow for 1 h. After cooling to room temperature, the pellet was exposed to NH_3 gas of 20 Torr pressure for 3 min. Desorption of NH_3 was performed by evacuation at different temperatures (30, 150 and 250 ^oC). The spectrum was recorded after desorption at each temperature. To quantify the Bronste/Lewis acidity, the previously reported peak area-amount correlation is used [124]. NH_4^+ symmetric stretching (~1450 cm^{-1}, Brønsted acid site) is typically seven-times more sensitive to asymmetric deformation of NH_3 coordinated to a Lewis acid site (~1610 cm^{-1}). To adjust for this, the peak area of the Brønsted acid site was divided by 7. In order to quantify the amounts of Bronsted acid sites, it was assumed that total acid amounts obtained from NH_3 TPD were similar to amounts of NH_3 remained after evacuation at 30^oC (in-situ FTIR).

3.2.3 Acid catalyzed reaction

Esterification of 1-butanol and acetic acid was carried out on a closed autoclave reactor with magnetic stirrer. Typically, 18.5ml of 1-butanol (200 mmol) and 11.5ml of acetic acid (200 mmol) were added to reactor. A 0.2 g sample was then introduced to the reactant. The reactor was heated to 150ºC and maintained for 4 h. Product was separated from the catalysts and analyzed by gas chromatography (Younglin ACME 6100 instrument) equipped with a FID detector and a HP-Innowax capillary column.

3.3 Results and discussion

3.3.1 Textural properties

Detailed pore structure and surface area of the materials were investigated by N_2 physisorption and the results are shown in Figure 3-1 and Table 3-1. An isotherm plot and pore size distribution of the catalysts are shown in Figure 3-1. The WZr0 to WZr5 samples show a Type IV isotherm and H1 hysteresis loop between P/P_0=0.6~0.8. This is caused by ordered cylindrical pores similar to mesoporous silicate, i.e., SBA-15. However, the WZr10 sample showed a broader hysteresis loop. Correspondingly, the WZr0 and WZr5 samples had a uniform pore size of about 5 nm and WZr10 had a smaller pore size with a non-uniform distribution. The different hysteresis loop and corresponding pore structure might be due to the penetration of zirconium into SiO_2 framework, as previously reported [117].

Table 3-1 shows the BET surface area, average pore size, and pore volume of the prepared catalysts. Except for WZr5 and WZr10, a high BET surface area of over 500 m^2/g was found. Compared to WZr0, the BET surface area increased slightly by the addition of a small amount of zirconium (WZr1), but then decreased gradually with increasing amounts of zirconium. The average pore size of the WZrX catalysts was about 5.3nm, except for WZr10, which has a smaller size of about 4.4 nm.

Three possible crystalline phases could be present on WO_x/ZrO_2, namely, monoclinic WO_3, tetragonal ZrO_2 and monoclinic ZrO_2 phases [45,120]. The

crystalline structures of ZrO_2 are not crucial factors for activity. However, the formation of monoclinic WO_3 is known as a 'boundary point of decreasing activity' on the volcano relationship between activity and WO_x loading [120]. XRD data for the prepared catalysts reveal the presence of monoclinic WO_3 for WZr0 and WZr1 (Figure 3-2 a, b). WZr3, WZr5 and WZr10 showed only a broad peak near 25° due to silica. No peaks corresponding to crystalline ZrO_2 were found for any of the catalysts. It is known that tungstate inhibits the crystallization of zirconia [45,120]. Similarly the addition of zirconium inhibits the aggregation of tungstate and results in the elimination of crystalline WO_3. Importantly, gradual shift of the peak appeared from amorphous SiO_2 also supports the insertion of Zr in SiO_2 framework.

To verify the results of N_2 physisorption and XRD, transmission electron microscopy was carried out to directly image the prepared catalysts. The results were consistent with the N_2 physisorption and XRD results. For WZr0 and WZr1, monoclinic WO_3 was formed and separated from mesoporous silica (Figure 3-3 inset) and an ordered cylindrical pore was found on WZr0 to WZr5, while the presence of cylindrical pores in WZr10 was unclear.

Table 3-1 Textural properties of the WZrX catalysts.

Catalysts	Surface area (m^2/g)	Average pore size (nm)	Pore volume (cm^3/g)
WZr0	575	5.3	0.805
WZr1	629	5.1	0.874
WZr3	558	5.3	0.814
WZr5	477	5.5	0.699
WZr10	346	4.4	0.413

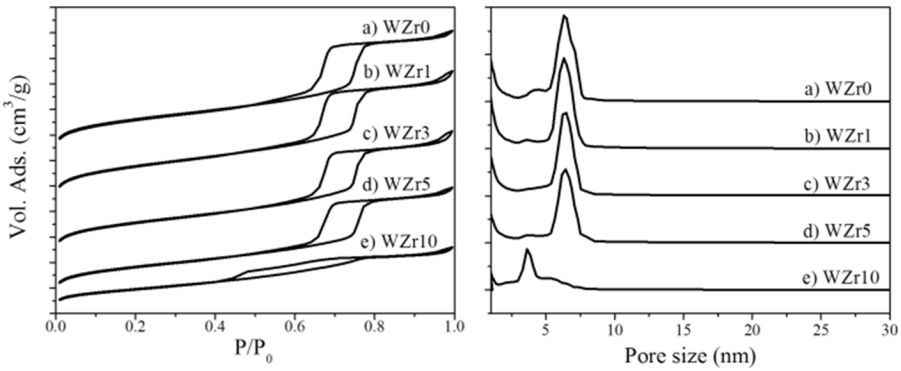

Figure 3-1. Isotherm plot (left) and pore size distribution (right): a) WZr0, b) WZr1, c) WZr3, d)WZr5, and e) WZr10.

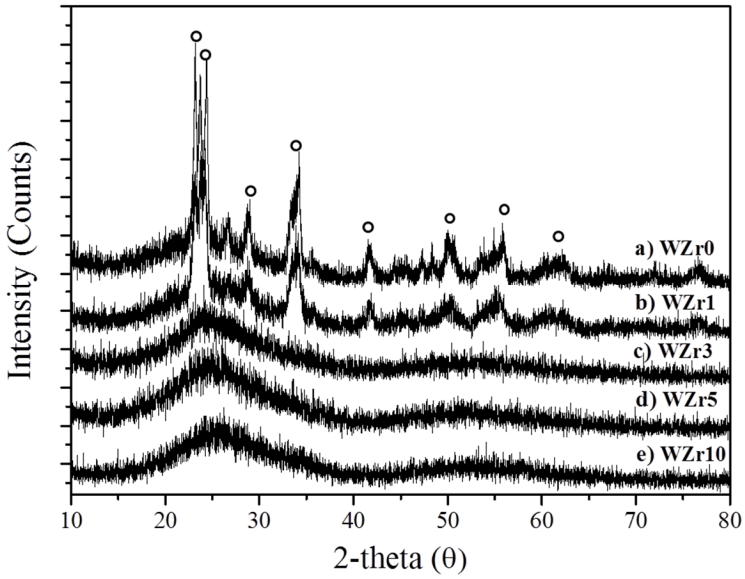

Figure 3-2. XRD patterns of WZrX catalysts: Monoclinic WO_3 (circle).

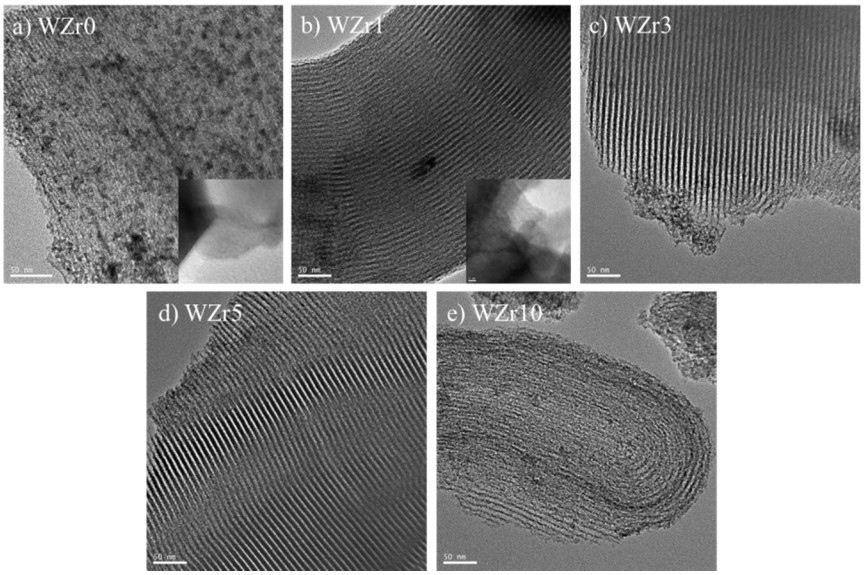

Figure 3-3. TEM images of WZrX catalysts: a) WZr0, b) WZr1, c) WZr3, d) WZr5, and e) WZr10.

3.3.2 The nature of tungstate on WZrX catalysts

X-ray photoelectron spectroscopy has been used to correlate the oxidation state and acidity of WO_x/ZrO_2 catalysts [132-134]. M.A. Corte´s-Ja´come et al. reported a trend in the XPS results for WO_x/ZrO_2 catalysts prepared at different calcination temperatures [132]. They confirmed that a large portion of the W^{5+} was present in the case of catalysts calcined at 560 ^oC, while no W^{5+} was found for samples calcined at 700 ^oC. Some of the W^{5+} was formed again when the preparation was calcined at 800 ^oC. Among these catalysts, calcination at 700 ^oC resulted in the largest amount of Brønsted acidity, but there was no clear relation between the oxidation state of W and acidity. However, it is obvious that the state of W is an important factor and that it could affect the acidity of tungstate.

XPS results for the WZrX catalysts revealed not only changes in the oxidation state, but also important evidence for the presence of Zr-WO_x clusters. Figure 3-4 shows XPS spectra of the W4f region. W4f consists of two spin-orbit components. The peak at 35.7±0.2 eV and 37.8±0.2 eV is assigned to W^{6+} species [132]. The W^{5+} species show two peaks at 34.7±0.2 eV and 36.8±0.2 eV. A relatively large amount of tungsten (about 17 %) exists as W^{5+} on WZr0. Full width at half maximum of the peak for W^{6+} (2.88 eV) is larger than that for the other catalysts, which indicates that a more diverse state of tungstate was formed. A small amount of added zirconium results in a significant decrease in the amount of W^{5+} (8%) as well as the narrowing of the W^{6+} peak (FWHM=2.32 eV). The same trend was found for increasing amounts of Zr for WZr3, WZr5

and WZr10. It is interesting to note that the presence of Zr has a significant effect on the oxidation state of W, which supports the strong interaction between Zr and W.

O1s spectra of the WZrX catalysts provided important evidence for the location of zirconium (Figure 3-5). Because zirconium was not included in the WZr0 catalyst, there would be two peaks, from SiO_2 and WO_X, in the O1s region. As can be seen in Figure 3-5, the O1s spectrum is clearly distinguished by the two peaks (532.8, 530.6 eV). The binding energy of each peak is similar to that of SiO_2 (532.6~533.3 eV) and WO_3 (530.2~530.8eV), which can be reasonably deconvoluted. Herein, O1s (Si) and O1s (tail) are denoted for the larger peak (532.8 eV) and the smaller one (530.6 eV), respectively.

Because WZr0 contains no zirconium, the O1s (tail) peak is solely contributed by tungstate. When the amount of zirconium in the catalysts is increased, the growth of O1s (tail) would be expected to be due to the similar binding energy of ZrO_2 (530.2~530.9 eV) and WO_3 (530.2~530.8 eV). However, the area ratio of O1s (tail) and O1s (Si) is almost the same for WZr0, WZr1, and WZr3 (0.041, 0.043, and 0.044, respectively). The ratio slightly increases to 0.055 for WZrX 5, and then suddenly increases to 0.21 for WZr10. This trend reveals important structural information related to the catalysts, especially the location of Zr.

Scheme 3-1 describes the influence of Zr insertion on different locations. When Zr is located on tungstate, the oxygen of W-O-Zr would be not much different from the original W-O-H or W-O-W due to the similar O1s binding energy of WO_3 and ZrO_2. Hence, the O1s (tail)/O1s (Si) ratio is retained. However, the situation is different when Zr is included in the SiO_2 framework.

Because the O1s binding energy is significantly different between SiO_2 and ZrO_2, O1s (tail) would be increased. Based on this assumption, this explains that the similar O1s (tail)/O1s (Si) ratio of WZr0, WZr1 and WZr3 is due to Zr is located on tungstate rather than on the SiO_2 framework. A slight increase in the ratio for WZr5 means that Zr starts to form in silicate as well as tungstate. For WZr10, the ratio is significantly increased to 0.21, which would result in a disordered cylindrical pore structure (consistent with the TEM images).

Tungstate based catalysts, including WO_x/ZrO_2, have been extensively studied, in attempts to determine the active site and to correlate the structure with activity [115,119,120,126-132]. Raman spectroscopy data for WO_x/ZrO_2 revealed that the presence of Zr-WO_x and tungstate with Keggin like structures [115,119,127]. Previous investigators attempted to determine the nature of the coordination and bonding of tungstate present in active WO_x/ZrO_2 [130,131]. Even though no significant differences between active and non-active catalysts were found, it was revealed that tungstate is mainly comprised of 'edge-shared octahedra' rather than corner-shared octahedra. Among the various characterizations, ultraviolet-visible spectroscopy also has been utilized to investigate the structure of tungstate [115,119,120,126-128]. On tungstate based materials, a sharp absorption between 2.6 eV and 3.6 eV is typically found, which is caused by ligand-to-metal charge transfer ($O_{2p} \rightarrow W_{5d}$) [119]. The absorption edge energy (Eg) is affected by several factors: i) the tungstate domain size (confinement effect), ii) the structure of the tungstate, iii) effect of the support [119]. There might be some differences in the tungstate structure between well-studied WO_x/ZrO_2 catalysts and our WZrX catalysts because of

the presence of silicate. However, both WO_x/ZrO_2 and WO_x/SiO_2, which have been previously studied, showed edge-shared units with Keggin-like structures [130,131,135]. It would therefore be expected that the local structure of WZrX catalysts would not differ substantially from that of WO_x/ZrO_2.

In Figure 3-6, two shoulders in WZr0 and WZr1 indicate the different tungstates are formed. The first shoulder of absorption edge energy (Eg)≈2.5 eV is assigned to monoclinic WO_3, and the second to polytungstate.[119] Because monoclinic WO_3 is presented, it is hard to obtain the Eg value of polytungstate in these catalysts. However, compared to WZr3, WZr5, and WZr10, a second shoulder starts at a lower energy. Hence, the Eg of polytungstate on the two catalysts is lower than the others. Different from WZr0 and WZr1, monoclinic WO_3 (Eg≈2.5eV) disappears on WZr3, WZr5 and WZr10, which is consistent with the TEM and XRD findings. The second shoulder, which is unclear in the case of WZr0 and WZr1, is clearly present. The Eg value is 3.3 eV for WZr3 and 3.4 eV for WZr5 and WZr10, which is assigned to presence of a polytungstate W-O-W linkage [119]. The absorption edge energy of WZr3 is higher than that for the supported 20 wt% WO_x/ZrO_2 (Eg=3.0eV). This can be attributed to the influence of the support rather than structure or domain size of tungstate. E. Iglesia et al. reported that the Eg of monotungstate present on WO_x/ZrO_2 (3.49 eV) and WO_x/Al_2O_3 (3.95 eV) was much lower than isolated molecular monotungstate, Na_2WO_4 (4.89 eV), due to tungstate-support interactions which cause increase in the effective domain size [119]. As is well known, different from Al_2O_3 and ZrO_2, the interaction between silica and tungstate is weak even when monoclinic WO_3 is formed using a very

low concentration of tungstate [119,126,136]. Hence the effect of the silica support on the increase in effective domain size would be expected to be lower than ZrO_2 and Al_2O_3, which would result in a higher Eg value. The very similar Eg values of WZr5 and WZr10 could be explained by differences in the effect of the support on the catalysts. As already shown by the XPS results, only a small amount of Zr was contained by the SiO_2 framework for WZr5, so the effect of the support would be almost the same as WZr3. However situation was somewhat different for WZr10 because large amounts of Zr were introduced. The surroundings of tungstate on WZr10 are mixed ZrO_2-SiO_2 rather than SiO_2. Therefore, it resulted an increase in the effective domain size due to effect of ZrO_2, thus decreasing the absorption edge energy.

Compared to the Keggin structured model tungstate (ammonium metatungstate, phosphotungstic acid), the Eg of WZr3 and WZr5 is slightly higher (3.0eV vs 3.3, 3.4eV). It is known that the Eg of tungstate is linearly correlated with the average number of covalent bridging W-O-W bonds [127]. The $N_{W\text{-}O\text{-}W}$ for a Keggin structure is 4. Because of the Keggin-like structure present on WO_x/ZrO_2 and WO_x/SiO_2, the $N_{W\text{-}O\text{-}W}$ of WZr3 and WZr5 would be lower than 4, consequently resulting in a lower domain size for tungstate. Zhou et al. recently demonstrated the presence of Zr-WO_x clusters through direct imaging using HAADF-STEM [121]. They reported that Zr-WO_x clusters present on WO_x/ZrO_2 are comprised of sub-nanometre tungstate with a 3D structure. Because it is known that the molecular size of Keggin structured 12-tungstate is about 1 nm [137], the slightly lower $N_{W\text{-}O\text{-}W}$ for WZr3 and WZr5 is in agreement with previous research findings.

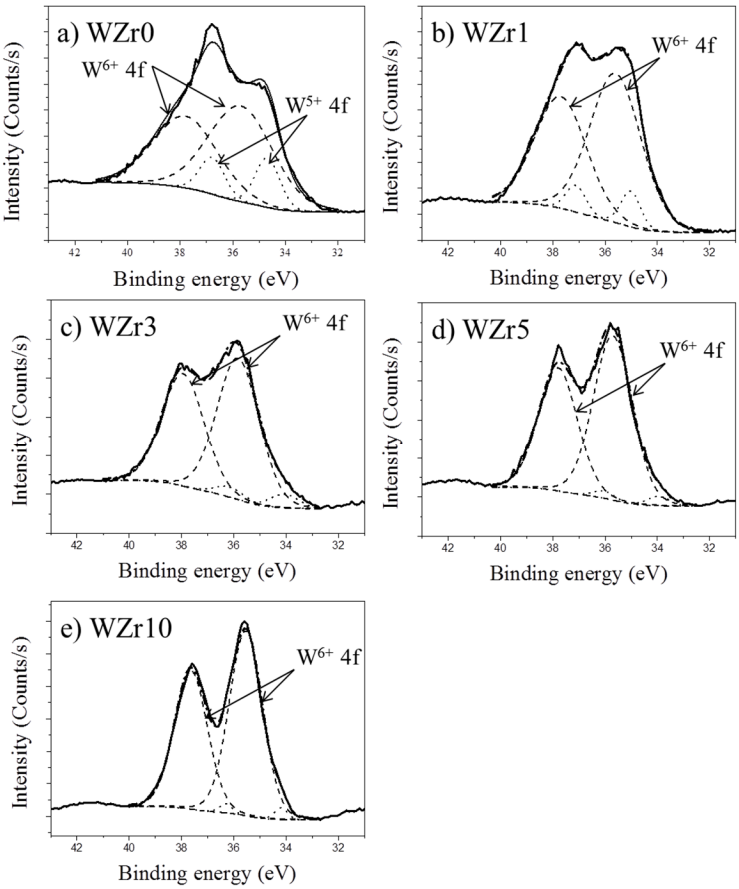

Figure 3-4. X-ray photoelectron W4f spectra of WZrX catalysts: a) WZr0, b) WZr1, c) WZr3, d) WZr5, and e) WZr10.

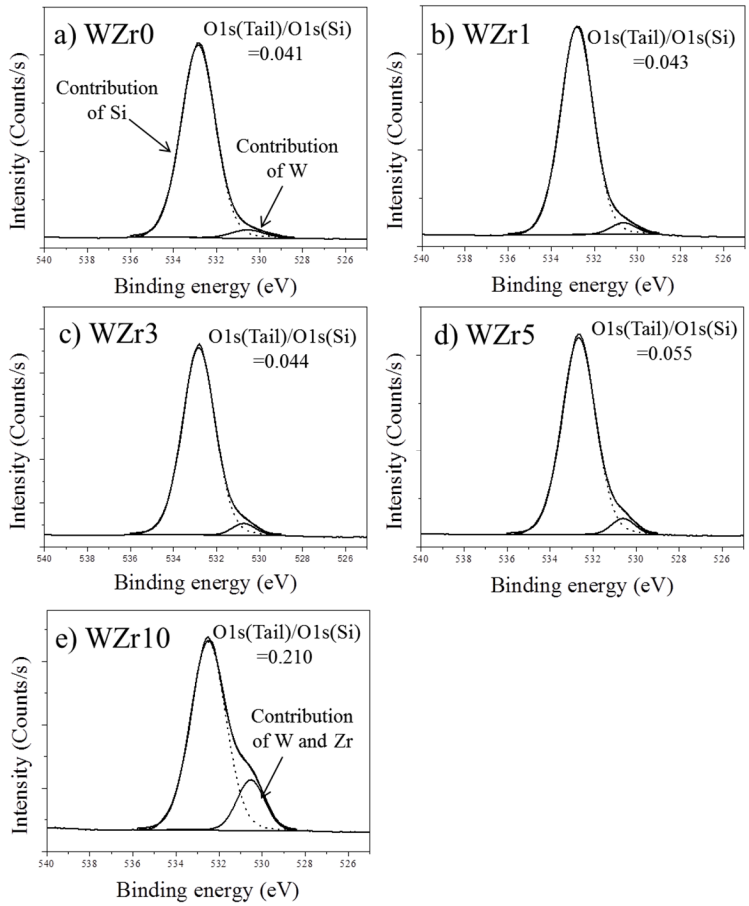

Figure 3-5. X-ray photoelectron O1s spectra of WZrX catalysts: a) WZr0, b) WZr1, c) WZr3, d) WZr5, and e) WZr10.

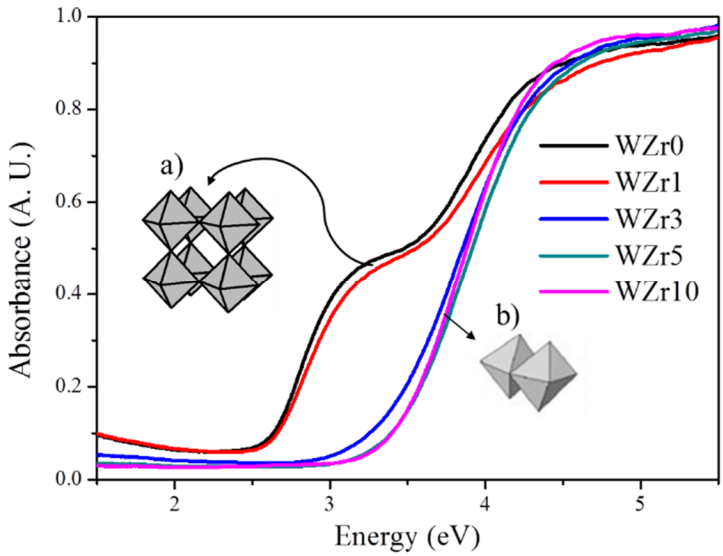

Figure 3-6. UV-Vis spectra of WZr catalysts: Assigned to a) monoclinic WO_3, and b) polytungstate and monotungstate.

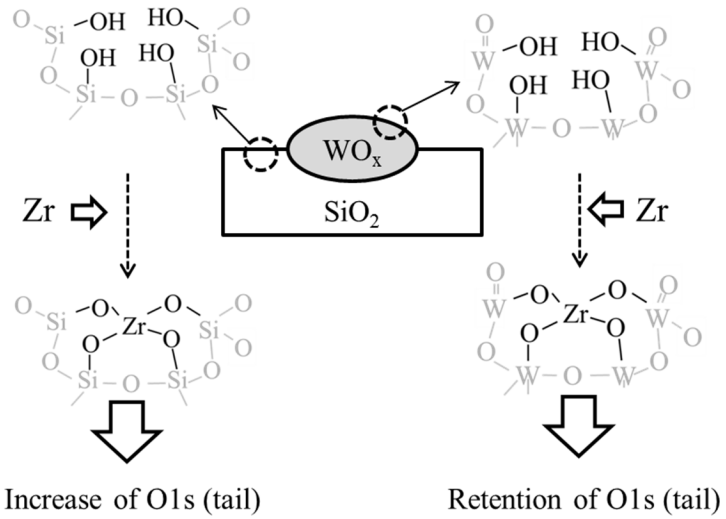

Scheme 3-1 Influence of zirconium location on O1s spectra.

3.3.3 Structure of WZrX catalysts

Based on textural properties, XPS and UV-Vis results, the structures of the WZrX catalysts are shown in scheme 3-2. The presence of monoclinic WO_3 on WZr0 and WZr1 was confirmed by TEM, XRD and UV-Vis. In addition, polytungstate is formed on these catalysts. From the XPS results, Zr is incorporated into tungstate rather than SiO_2 on WZr1 and WZr3. So, monoclinic WO_3 and Zr-WO_x clusters would be formed on WZr1. For WZr3, there are only Zr-WO_x clusters without monoclinic WO_3. Polytungstate or monotungstate in smaller sizes would be formed on WZr5, which was confirmed by the lower absorption edge energy. Thus, the maximum density of the Zr-WO_x clusters would be achieved at a Zr/W ratio of 0.3. A large amount of Zr is introduced into the SiO_2 of WZr10, so the tungstate is surrounded by ZrO_2-SiO_2 rather than SiO_2. Consequently polytungstate or monotungstate in smaller sizes are mainly formed on WZr10 with the collapse of the uniform pore structure.

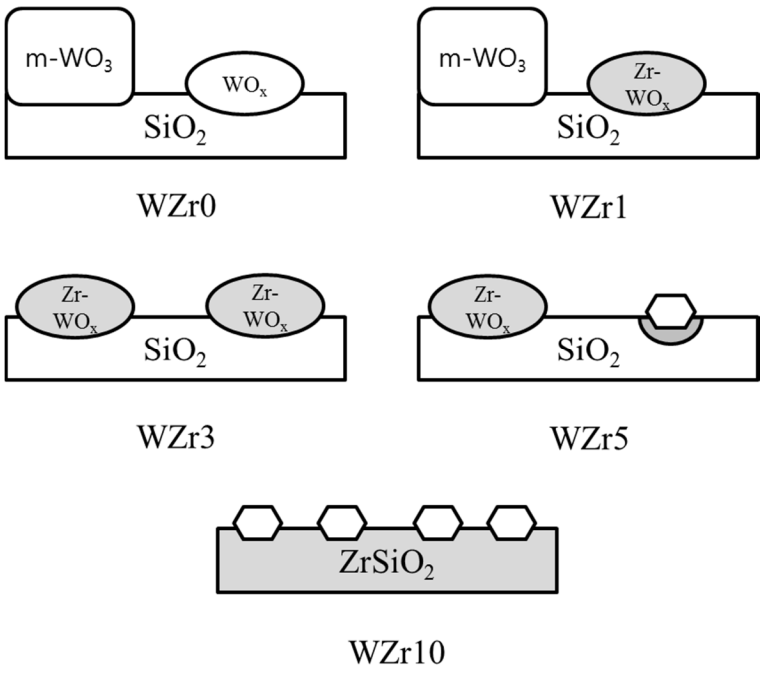

Scheme 3-2 Structures of the WZrX catalysts: Monoclinic WO_3 (m-WO_3), polytungstate (WO_x), Zr-WO_x clusters (Zr-WO_x, gray-filled), and small polytungstate and monotungstate (hexagon).

3.3.4 Acidic properties of WZrX catalysts

To insure the accurate quantification of Brønsted and Lewis acidity, the total amount of acid was estimated by NH_3 TPD and NH_3 *in-situ* FTIR was then used to determine the ratio of Brønsted and Lewis acid sites.

Figure 3-7 shows the NH_3 in-situ FTIR results for samples evacuated at 150°C. The peak maximum at 1450cm^{-1} is assigned to protonated NH_4^+ adsorbed to Brønsted acid sites. The peak of 1610cm^{-1} is assigned to NH_3 coordinatively bonded to Lewis acid sites [138]. Figure 3-8 shows the amount of Brønsted acid sites calculated from the NH_3 TPD and NH_3 *in-situ* FTIR results at each evacuation temperature. When evacuated at 30°C, the highest level of Brønsted acid sites was present on WZr5. While, at 150°C and 250°C, WZr3 contain higher amounts of Brønsted acid than the other catalysts. The Brønsted acid content for WZr0 is comparable to WZr5, except at 30°C. WZr1 and WZr10 show similar Brønsted acidities. Consequently, it can be concluded that stronger Brønsted acid sites were formed more on WZr3 to a greater extent.

It appears that the population of Zr-WO_x clusters is an important factor in terms of Brønsted acidity. In the case of WZr0, the fact that it has a higher Brønsted acidity than WZr1 can be attributed to the large number of W^{5+}-O-W^{6+} bonds, which could generate acidic protons. As discussed above, the WZr3 catalyst contained mainly Zr-WO_x clusters, while the other catalysts contained monoclinic WO_3 or tungstate in smaller sizes, and it showed a stronger Brønsted acidity than the other catalysts. The Brønsted acidities of WZr5 and WZr10 then decreased gradually because tungstate in smaller sizes was formed.

Thus, major factor influencing the Brønsted acidity of the WZrX catalysts is the population of Zr-WO_x clusters.

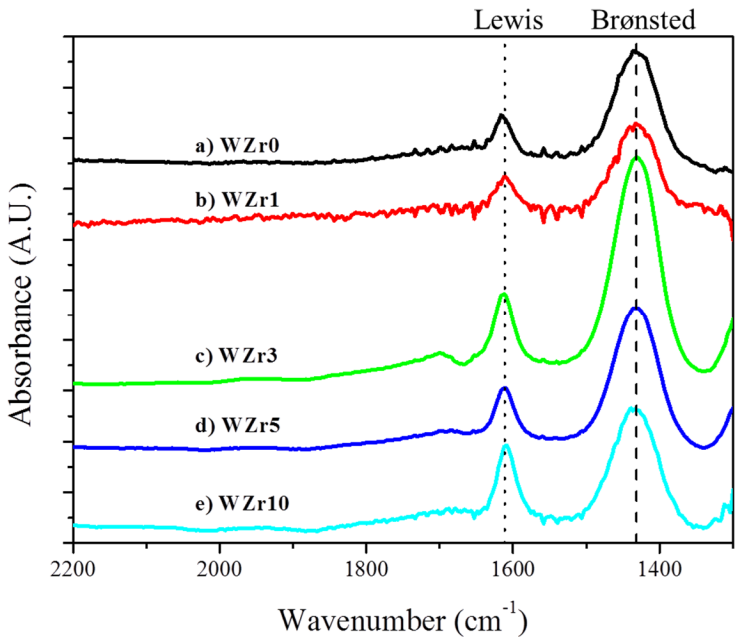

Figure 3-7. NH_3 in-situ FTIR of WZrX catalysts: Evacuation at 150 ºC.

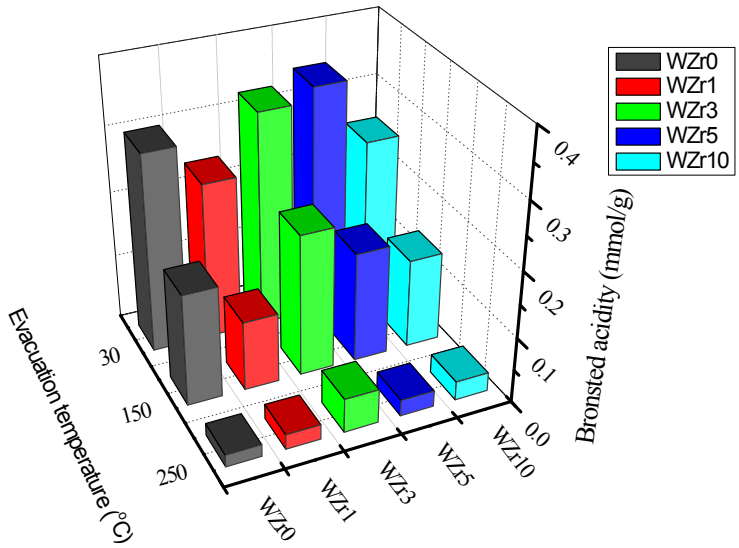

Figure 3-8. Contents of Bronsted acid sites for WZrX cataysts at each evacuation temperature.

3.3.5 Acid catalyzed reactions

It was known that esterification reactions are catalyzed by Brønsted acids. Several authors reported that Lewis acids also catalyzed this reaction [139, 140], but such catalysts are mostly supported metal chlorides, which have highly strong Lewis acid sites and can form HCl. While, supported metal oxides follow the mechanism of Brønsted acid catalyzed reactions [141].

Figure 3-9 shows the results for the prepared WZrX catalysts and control catalysts (HZSM-5, WO_x/ZrO_2) on the esterification of 1-butanol and acetic acid. Compared to the control catalysts, the WZrX catalysts showed a significantly higher activity, except for WZr10. WZr3 showed highest activity among the WZrX catalysts due to its stronger Brønsted acidity. The activities of WZr0 and WZr5 were almost the same. Significantly, the low activity of WZr10 can be explained by its relatively smaller pore size and low surface area even though it has a similar content of Brønsted acid sites as WZr1. The linear relationship between activity and Brønsted acid content at 150^{o}C verifies that the reaction is catalyzed by Brønsted acids.

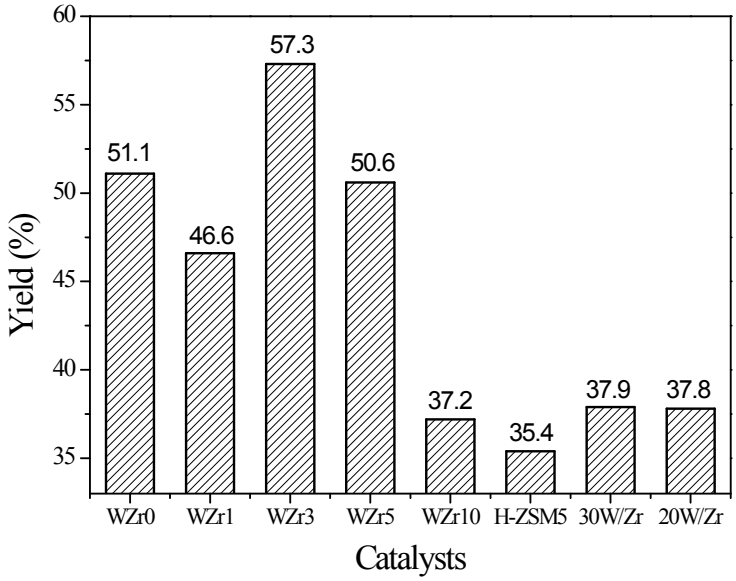

Figure 3-9. Esterification of 1-butanol and acetic acid: T=150ºC, time=4h, 1-butanol/acetic acid=1/1, catalyst 0.2 g.

Chapter 4. Summary and Conclusions

The dehydrative epoxidation of 2,3-butanediol into 2,3-epoxybutane and heterogeneous catalytic process for the production of 1,3-butadiene are reported. Among a series of supported basic metal oxides tested, a CsO_x/SiO_2 catalyst was found to be the most effective catalyst for the dehydrative epoxidation to produce 2,3-epoxybutane. The optimized catalyst with respect to loading amount of Cs_2O and calcination temperature (1 wt.% CsO_x/SiO_2 calcined at 823 K) exhibited specific activity of 59.3 h^{-1}. Based on the experimental evidences and the DFT results, the CsO_x/SiO_2 catalyst appears to be an outstanding catalyst for dehydrative epoxidation reactions for the following reasons: i) sufficiently strong base strength induced by the presence of cesium, ii) large ionic radius and low silicate dissolution that permit Cs^+ to exist on the surface and to be accessible to the reactant, iii) formation of stable basic sites in virtue of strong interactions between Cs^+ and surface oxygens caused by the low point of zero charge of SiO_2, and iv) relatively acidic protons of surface hydroxyl sites of SiO_2 which is advantageous for the elimination to H_2O. When the relative energies for different conformations (*gauche*- and *anti*-arrangement) of *meso*-2,3-butanediol is considered by the DFT calculations, *anti-meso*-2,3-butanediol is less stable than *gauche-meso*-2,3-butanediol in the gas phase (9 kJ/mol) and in the adsorption on the CsO_x/SiO_2 model surface (40 kJ/mol). However, the activation barrier for the dehydrative epoxidation of *anti-meso*-2,3-butanediol into *trans*-2,3-epoxybutane (160 kJ/mol; TS1 and path 1) is

much lower than that of *gauche-meso*-2,3-butanediol into *trans*-2,3-epoxybutane (292 kJ/mol; TS2 and path2) and *cis*-2,3-epoxybutane (276 kJ/mol; TS3 and path3). The above results allow us to conclude that the dehydrative epoxidation is mainly induced via S_N2-like stereospecific mechanism, resulting in the selective formation of *trans*-2,3-epoxybutane from *meso*-2,3-butanediol. Using the dehydrative epoxidation, the production of 1,3-butadiene from 2,3-butanediol using the heterogeneous catalytic system is proposed. Sequential processes consisting of dehydrative epoxidation, isomerization, and acid catalyzed dehydration can result in the highly selective production of 1,3-butadiene. It can conclude that dehydrative epoxidation can expand the scope of chemicals that can be produced from biomass-derived feedstocks by widening the dehydration route.

In order to replace conventional homogeneous mineral acid catalyst for the esterification reaction, mesoporous Zr-WO_x/SiO_2 catalysts with high surface areas and a high density of Zr-WO_x clusters was prepared. The sequential hydrolysis of zirconium and tungsten was used to insure the formation of pre-Zr-WO_x clusters. The Zr/W ratio was varied to find optimum conditions required for Zr-WO_x cluster formation. Except for a Zr/W ratio of 1, the prepared catalysts contained ordered cylindrical mesopores with a uniform size about 5 nm. Not only polytungstate, but inactive monoclinic WO_3 was also formed when for ratios of Zr/W<0.3. Below a certain Zr/W ratio (≈0.5), zirconium was primarily located on tungstate rather than SiO_2, which result in the formation of Zr-WO_x clusters. When the Zr/W ratio exceeded this value, less active monotungstate and polytungstate in smaller sizes were formed and

ordered mesopores sometimes collapsed. Based on the characterization results, it can be concluded that the optimum Zr/W ratio for producing a high density of Zr-WO_x clusters is ca. 0.3 (WZr3). At this ratio, a larger amount of strong Brønsted acid sites are formed. The catalytic performance of Zr-WO_x/SiO_2 catalysts for the esterification of 1-butanol and acetic acid was significantly improved compared to HZSM-5 and WO_x/ZrO_2. Among the Zr-WO_x/SiO_2 catalysts studied, the highest activity was found for a Zr/W ratio of 0.3 because of its high Brønsted acidity as the result of the high density of Zr-WO_x clusters.

Bibliography

[1] J. C. S. Ruiz, J. A. Dumesic, *Energy Environ. Sci.* **2011**, 4, 83-99.

[2] S. V. Vassilev, D. Baxter, L. K. Andersen, C. G. Vassleva, *Fuel* **2010**, 89, 913-933.

[3] J. G. Speight, *The Chemistry and Technology of Petroleum, Marcel Dekker* **1999** pp. 215-216, ISBN 0-8247-0217-4.

[4] S. Dutta, *ChemSusChem* **2012**, 5 2125-2127.

[5] L. Petrus, M. A. Noordermeer, *Green Chem*. **2006**, 8, 861-867.

[6] E. L. Kunkes, D. A. Simonetti, R. M. West, J. C. S. Ruiz, C. A. Gärtner, J. A. Dumesic, *Science* **2008**, 322, 417-421.

[7] M. E. Zakrzewska, E. B. Łukasik, R. B. Łukasik, *Chem. Rev*. **2011**, 111, 397-417.

[8] J. N. Chheda, Y. R. Leshkov, J. A. Dumesic, *Green Chem*. **2007**, 9, 342-350.

[9] R. Weingarten, G. A. Tompsett, W. C. Conner, G. W. Huber, *J. Catal.* **2011**, 279, 174-182.

[10] A. Dias, M. Pillinger, A. Valente, *J. Catal*. **2005**, 229, 414-423.

[11] M. Chidambaram, A. T. Bell, *Green Chem.* **2010**, 12, 1253-1262.

[12] Y. R. Leshkov, C. J. Barrett, Z. Y. Liu, J. A. Dumesic, *Nature* **2007**, 447, 982-985.

[13] L. Bui, H. Luo, W. R. Gunther, Y. R. Leshkov, *Angew. Chem. Int. Ed.* **2013**, 52, 8022-8025.

[14] J. Q. Bond, D. M. Alonso, D. Wang, R. M. West, J. A. Dumesic, *Science* **2010**, 327, 1110-1114.

[15] Y. Choi, D. S. Park, H. J. Yun, J. Baek, D. Yun, J. Yi, *ChemSusChem* **2012**, 5, 2460-2468.

[16] D. S. Park, B. K. Kwak, N. D. Kim, J. R. Park, J. H. Cho, S. Oh, J. Yi, *ChemCatChem* **2012**, 4, 836-843.

[17] D. Yun, T. Y. Kim, D. S. Park, Y. S. Yun, J. W. Han, J. Yi, *ChemSusChem* **2014**, 7, 2193-2201.

[18] A. Corma, S. Iborra, A. Velty, *Chem. Rev.* **2007**, 107, 2411-2502.

[19] A. Harden, G. S. Walpole, *Proc. Royal Soc.* **1906**, B77, 399–405.

[20] J.H. Cho, C. Rathnasingh, H. Song, B.W. Chung, H.J. Lee, D. Seung, *Bioprocess Biosyst. Eng.* **2012**, 35, 1081–1088.

[21] S. H. Han, J. E. Lee, K. Park, Y. C. Park, *N. Biotechnol.* **2013**, 30, 166–172.

[22] T. Hassler, D. Schieder, R. Pfaller, M. Faulstich, V. Sieber, *Bioresour. Technol.* **2012**, 124, 237–244.

[23] M. Y. Jung, C. Y. Ng, H. Song, J. Lee, M. K. Oh, *Appl. Microbiol. Biotechnol.* **2012**, 95, 461–469.

[24] M. Ehsani, M. R. Fernández, J. A. Biosca, A. Julien, S. Dequin, *Appl. Environ. Microbiol.* **2009**, 75, 3196-3205

[25] C. Y. Ng, M. Y. Jung, J. Lee, M. K. Oh, *Microb Cell Fact,* **2012**, 11, 68-81

[26] J. Lian, R. Chao, H. Zhao, *Metab. Eng.* **2014**, 23, 92-99

[27] H. Nan, S. O. Seo, E. J. Oh, J. H. Seo, J. H. D. Cate, Y. S. Jin, *Appl. Microbiol. Biotechnol.* **2014**, 98, 5757-5764.

[28] S. Atsumi, A. F. Cann, M. R. Connor, C. R. Shen, K. M. Smith, M. P. Brynidlsen, K. J. Chou, T. Hanai, J. C. Liao, *Metab. Eng.* **2008**, 10, 305-311.

[29] M. Inui, M. Suda, S. Kimura, K. Yasuda, H. Suzuki, H. Toda, S. Yamamoto, S. Okino, N. Suzuki, H. Yukawa, *Appl. Microbiol. Biotechonol.* **2007**, 77, 1305-1316.

[30] G. K. Donaldson, L. L. Huang, L. A. Maggio-Hall, V. Nagarajan, C. E. Nakamura, W. Suh, **2007** International Patent WO 2007/041269

[31] J. C. Liao, S. Atsumi, M. P. Brynildsen, A. F. Cann, K. J. Chou, C. R. Shen, K. M. Smith, T. Hanai, M. R. Connor **2008** International Patent WO 2008/124523

[32] U. Gunawardena, P. Meinhold, M. W. Peters, J. Urano, R. Feldman **2008** International Patent WO 2008/010124

[33] T. Buelter, A. Hawkins, K. Kersh, P. Meinhold, M. Peters, E. Subbian **2008** International Patent WO 2008/143704

[34] E. J. Steen, R. Chan, N. Prasad, S. Myers, C. J. Petzold, A. Redding, M. Ouellet, J. D. Keasling, *Microb. Cell. Fact*. **2008**, 7, 36.

[35] D. R. Nielsen, E. Leonard, S. H. Yoon, H. C. Tseng, C. Yuan, K. L. Prather, *Metab. Eng.* **2009**, 11, 262-273.

[36] Web page: http://www.butamax.com/renewable-fuel-technologies.aspx

[37] Web page: http://www.butalco.com/

[38] E. Celinska, W. Grajek, *Biotechnol. Adv.* **2009**, 27, 715.

[39] (a) N. Shlechter, D. F. Othmer, S. Marshak, *Ind. Eng. Chem.* **1945**, 37, 900; (b) N. Shlechter, D. F. Othmer, R. Brand, *Ind. Eng. Chem.* **1945**, 37, 905.

[40] J. Baek, T. Y. Kim, W. Kim, H. J. Lee, J. Yi, Green Chemistry 2014, 16(7), 3501-3507.

[41] T. A. Peters, N. E. Benes, A. Holme, J. T.F. Keurentjes, *Appl. Catal. A* **2006**, 297, 182-188.

[42] A. Corma, H. Garcia, S. Iborra, J. Primo, *J. Catal.* **1989**, 120, 78-87.

[43] M. Hino, K. Arata, *J. Chem. Soc. Chem. Commun.* **1988**, 1259–1260.

[44] D. G. Barton, S. L. Soled, G. D. Meitzner, G. A. Fuentes, E. Iglesia, *J. Catal.* **1999**, 181, 57.

[45] G. Larsen, E. Lotero, L. M. Petkovic, D. S. Shobe, *J. Catal.* **1997**, 169, 67.

[46] J.G Santiesteban, J.C Vartuli, S. Han, R.D Bastian, C.D Chang, *J. Catal.* **1997**, 168, 431.

[47] H. Duan, D. Sun, Y. Yamada, S. Sato, *Catal. Commun.* **2014**, 48, 1-4.

[48] S. Ramayya, A. Brittain, C. DeAlmeida, W. Mok, M. J. Antal, *Fuel* **1987**, 66, 1364-1371.

[49] P. J. Chong, G. Curthoys, *Zeolites* **1981**, 1, 41-51.

[50] K. Mori, Y. Yamada, S. Sato, *Appl. Catal. A* **2009**, 366, 304-308.

[51] D. Zhang, S. A. I. Barri, D. Chadwick, *Appl. Catal. A* **2011**, 400, 148-155.

[52] Z. Dai, B. Hatano, H. Tagaya, *Appl. Catal. A* **2004**, 258, 189-193.

[53] W. Zhang, D. Yu, X. Ji, H. Huang, *Green Chem.* **2012**, 14, 3441-3450.

[54] A.V. Tran, R. P. Chambers, *Biotechnol. Bioeng.* **1987**, 29, 343-351.

[55] G. Kresse, J. Furthmuller, *Phys. Rev. B* **1996**, 54, 11169-11186.

[56] J. P. Perdew, K. Burke, M. Ernzerhof, *Phys. Rev. Lett.* **1996**, 77, 3865-3868.

[57] P. E. Blöchl, *Phys. Rev. B* **1994**, 50, 17953-17979.

[58] S. Grimme, *J. Comput. Chem.* **2006**, 27, 1787-1799.

[59] F. Zhang, J. D. Gale, B. P. Uberuaga, C. R. Stanek, N. A. Marks, *Phys. Rev. B* **2013**, 88, 054112-054112-7.

[60] D. W. Sindorf, G. E. Maciel, *J. Am. Chem. Soc.* **1983**, 105, 1487-1493.

[61] I-S.Chuang, G. E. Maciel, *J. Phys. Chem. B* **1997**, 101, 3052-3064.

[62] L. T. Zhuravlev, *Langmuir* **1987**, 3, 316-318.

[63] J. B. Per, A. L. Hensley, Jr., *J. Phys. Chem*. **1968**, 72, 2926-2933.

[64] J. Handzlik, J. Ogonowski, *J. Phys. Chem. C* **2012**, 116, 5571-5584.

[65] A. F. Wright, A. J. Leadbetter, *Philos. Mag.* **1975**, 31, 1391-1401.

[66] H. W. Park, S. Park, D. R. Park, J. H. Choi, I. K. Song, *Korean J. Chem. Eng.* **2011**, 28, 1177-1180.

[67] A. Zecchina, S. Bordiga, C. Lamberti, G. Spoto, L. Carnelli, *J. Phys. Chem.* **1994**, 98, 9577-9582.

[68] D. H. Olson, N. KhoSrOvani, A.W. Peters, B. H. Toby, *J. Phys. Chem. B* **2000**, 104, 4844-4848.

[69] a) Y. Kim, R. J. Kirkpatrick, *Geochimica et Cosmochimica Acta* **1997**, 61, 5199-5208; b) Y. Kim, R. J. Kirkpatrick, R. T. Cygan, *Geochimica et Cosmochimica Acta* **1996**, 60, 4059-4074.

[70] G. Henkelman, H. Jonsson, *J. Chem. Phys.* **2000**, 113, 9978-9985.

[71] G. Henkelman, B. P. Uberuaga, H. Jonsson, *J. Chem. Phys.* **2000**, 113, 9901-9904.

[72] a) S. Sato, R. Takahashi, T. Sodesawa, N. Honda, *J. Mol. Catal. A* **2004**, 221, 177-183; b) S. Sato, F. Sato, H. Gotoh, Y. Yamada, *ACS Catal*. **2013**, 3, 721-734.

[73] A) H. Tsuneki, *Appl. Catal. A* **2001**, 221, 209-217; b) H. Tsuneki, K. Ariyoshi, *Appl. Catal. A* **2007**, 331, 95-99.; c) Y. Sun, H. Yan, D. Liu, D. Zhao, *Catal. Commun*. **2008**, 9,924-930.

[74] a) G. Connell, J. A. Dumesic, *J. Catal.* **1987**, 105, 285-298; b) P. Carniti, A. Gervasini, S. Bennici, *J. Phys. Chem. B* **2005**, 10, 1528-1536.

[75] a) W. H. Brown, C. S. Foote, B. L. Iverson, *Organic Chemistry fourth edition,* Thomson Brooks/Cole: Belmont, CA, **2005**; pp 213-214, 343; b) J. M. Hornback, *Organic Chemistry second edition*, Thomson Brooks/Cole: Belmont, CA, **2006**; pp 272.

[76] P. Burk, S. Tamp, *J. Mol. Struc-THEOCHEM* **2003**, 638, 119-128.

[77] I. Dzidic, P. Kebarle, *J. Phys. Chem.* **1970**, 74, 1466-1474.

[78] S. K. Searla, I. Dzidic, P. Kebarle, *J. Am. Chem. Soc.* **1969**, 91, 2810-2811.

[79] P. Burk, K.Sillar, I. A. Koppel, *J. Mol. Struc.-THEOCHEM* **2001**, 543, 223-231.

[80] M. Huang, A. Adnot, S. Kaliaguine, *J. Catal.* **1992**, 137, 322-332.

[81] W. J. Mortier, *J. Catal.* **1978**, 55, 138-145.

[82] D. Barthomeuf, *Catal. Rev.* **1996**, 38, 521-612.

[83] H. Hattori, *Chem. Rev.* **1995**, 95, 537-558.

[84] S. B. Waghmode, R. Vetrivel, S. G. Hegde, C. S. Gopinath, S. Sivasanker, *J. Phys. Chem. B* **2003**, 107, 8517-8523.

[85] T. Horiuchi, H. Hidaka, T. Fukui, Y. Kubo, M. Horio, K. Suzuki, T. Mori, *Appl. Catal. A* **1998**, 167, 195-202.

[86] R. Bal, K. Chaudhari, S. Sivasanker, *Catal. Letters* **2000**, 70, 75-78.

[87] a) Y. T. Chua, A. R. Mohamed, S. Bhatia, *Appl. Catal. A* **2008**, 343, 142-148; b) A. G. Dedov, G. D. Nipan, A. S. Loktev, A. A. Tyunyaev, V. A. Ketsko, K. V. Parkhomenko, I. I. Moiseev, *Appl. Catal. A* **2011**, 406, 1-12; c) U. Simon, O. Görke, A. Berthold, S. Arndt, R. Schomäcker, H. Schubert, *Chem. Eng. J.* **2011**, 168, 1352-1359.

[88] E. Lippmaa, M. Magi, A. Samoson, G. Engelhardt, A.R. Grimmer, *J. Am. Chem. Soc*. **1980**, 102, 4889-4893.

[89] P. W. J. G. Wijnen, T. P. M. Beelen, J. W. de Haan, C. P. J. Rummens, L. J. M. van de Ven, R.A. van Santen, *J. Non-Cryst. Solids* 1989, 109, 85-94.

[90] L. T., Zhuravlev, *Colloids Surf., A* **2000**, 173, 1-38.

[91] B. M. Reddy, A. Khan, *Catal. Rev.* **2005**, 47, 257-296.

[92] M. M. Bhasin, J. H. McCain, B. V. Vora, T. Imai, P. R. Pujadó, *Appl. Catal. A* **2001**, 221, 397-419.

[93] K. Nakagawa, M. Okamura, N. Ikenaga, T. Suzuki, T. Kobayashic, *Chem. Commun.*, **1998**, 1025-1026.

[94] M. Kosmulski, *Adv. Colloid. Interfac*. **2009**, 152, 14-25

[95] a) A. J. L. Jesus, M. T. S. Rosado, I. Reva, R. Fausto, M. E. Eusébio, J. S. Redinha, *J. Phys. Chem. A* **2006**, 110, 4169-4179; b) A. J. L. Jesus, M. T. S. Rosado, M. L. P. Leitão, J. S. Redinha, *J. Phys. Chem. A* **2003**, 107, 3891-3897.

[96] J. J. Mortensen, M. Parrinello, *J. Phys. Chem. B* **2000**, 104, 2901-2907.

[97] J. Handzlik, R. Grybos, F. Tielens, *J. Phys. Chem. C* **2013**, 117, 8138-8149.

[98] A. Rimola, D. Costa, M. Sodupe, J. F. Lambert, P. Ugliengo, *Chem. Rev.* **2013**, 113, 4216-4313.

[99] J. Tai, Q. Ge, R. J. Davis, M. Neurock, *J. Phys. Chem. B* **2004**, 108, 16798-16805.

[100] A) K. Thomke, *J. Catal.* **1976**, 44, 339-344; b) S. Delsarte, P. Grange, *Appl. Catal. A* **2004**, 259, 269-279; c) M.G. Cutrufello, I. Ferino, V. Solinas, A. Primavera, A. Trovarelli, A. Aurouxc, C. Picciauc, *Phys. Chem. Chem. Phys.* **1999**, 1, 3369-3375.

[101] T. Imanaka, Y. Okamoto, S. Teranishi, *Bull. Chem. Soc. Jpn.* **1972**, 45, 1353-1357.

[102] T. A. Peters, N. E. Benes, A. Holmen, J.T.F. Keurentjes, *Appl. Catal. A* **2006**, 297, 182.

[103] F.R. Chen, G. Coudurier, J.F. Joly, J.C. Vedrine, *J. Catal.* **1993**, 143, 616.

[104] R. Srinivasan, R.A. Keogh, D.R. Milburn, B.H. Davis, *J. Catal.* **1995**, 153, 123.

[105] J. M. Thomas, *Sci. Am.* **1992**, 266, 112.

[106] *US Pat.* 5 401 478, **1995**.

[107] *US Pat.* 5 552 128, **1996**.

[108] *US Pat.* 5 563 310, **1996**.

[109] *US Pat.* 5 453 556, **1995**.

[110] M. Scheithauer, T.K. Cheung, R.E. Jentoft, R.K. Grasselli, B.C. Gates, H. Knözinger, *J. Catal.* **1998**, 180, 1.

[111] D. G. Barton, S. L. Soled, E. Iglesia, *Top. Catal.* **1998**, 6, 87.

[112] C. D. Baertsch, S. L. Soled, E. Iglesia, *J. Phys. Chem. B*, **2001**, 105, 1320.

[113] C. D. Baertsch, K. T. Komala, Y. Chua, E. Iglesia, *J. Catal.* **2002**, 205, 44.

[114] S. Kuba, P. Lukinskas, R. Ahmad, F. C. Jentoft, R. K. Grasselli, B. C. Gates, H. Knözinger, *J. Catal.* **2003**, 219, 376.

[115] M. Scheithauer, R. K. Grasselli, H. Knözinger, *Langmuir*, **1998**, 14, 3019.

[116] J.C. Vartuli, J.G. Santiesteban, P. Traverso, N. Cardona-Martinéz, C.D. Chang, S.A. Stevenson, *J. Catal.* **1999**, 187, 131.

[117] D.C. Calabro, J.C. Vartuli and J.G. Santiesteban, *Top. Catal.* **2002**, 18, 231.

[118] R. D. Wilson, D. G. Barton, C. D. Baertsch, E. Iglesia, *J. Catal.* **2000**, 194, 175.

[119] D. G. Barton,M. Shtein,R. D. Wilson,S. L. Soled,E. Iglesia, *J. Phys. Chem. B*, **1999**, 103, 630.

[120] E. I. Ross-Medgaarden, W. V. Knowles, T. Kim, M. S. Wong, W. Zhou, C. J. Kiely, I. E. Wachs, *J. Catal.* **2008**, 256, 108.

[121] W. Zhou, E. I. Ross-Medgaarden, W. V. Knowles, M. S. Wong, I. E. Wachs, C. J. Kiely, *Nat. Chem.* **2009**, 1, 722.

[122] N. Soultanidis,W. Zhou,A. C. Psarras,A. J. Gonzalez,E. F. Iliopoulou,C. J. Kiely, I. E. Wachs, M. S. Wong, *J. Am. Chem. Soc.* **2010**, 132, 13462.

[123] S. H. Moon, H. Windawi and J. R. Katzer, *Ind. Eng. Chem. Fundam.* **1981**, 20, 396-399.

[124] L.M. Cornaglia, E.A. Lombardo, J.A. Anderson, J.L. Gracia Fierro, *Appl. Catal.* **1993**, 100, 37.

[125] J. Iglesias, J. A. Melero, L. F. Bautista, G. Morales, R. Sánchez-Vázquez, M. T. Andreola, A. Lizarraga-Fernández, *Catal. Today*, **2011**, 167, 46.

[126] A. Guti´errez-Alejandre, J. Ram´ırez, G. Busca, *Catal. Lett.* **1998**, 56, 29.

[127] E. I. Ross-Medgaarden, Israel E. Wachs, *J. Phys. Chem. C*, **2007**, 111, 15089.

[128] J. Macht, C. D. Baertsch, M. May-Lozano, S. L. Soledb, Y. Wang, E Iglesia, *J. Catal.* **2004**, 227, 479.

[129] X. Chen, G. Clet, K. Thomas, M. Houalla, *J. Catal.* **2010**, 273, 236.

[130] X. Carrier,E. Marceau, H. Carabineiro, V. Rodrı´guez-Gonza´ lezab, M. Cheabd, *Phys. Chem. Chem. Phys.* **2009**, 11, 7527.

[131] T. Yamamoto, A. Orita, T. Tanaka, X-Ray Spectrom. **2008**, 37, 226.

[132] M.A. Corte´s-Ja´come, C. Angeles-Chavez, E. Lo´pez-Salinas, J. Navarrete, P. Toribio, J.A. Toledo, *Appl. Catal. A*, **2007**, 318, 178.

[133] F. D. Gregorio, V. Keller, *J. Catal.* **2004**, 225, 45.

[134] M. Occhiuzzi, D. Cordischi, D. Gazzoli, M. Valigi, P. C. Heydorn, *Appl. Catal. A*, **2004**, 269, 169.

[135] C. Martin, P. Malet, G. Solana, V. Rives, *J. Phys. Chem. B*, **1998**, 102, 2759.

[136] J. E. Herrera, J. H. Kwak, J. Z. Hua, Y. Wang, C. H.F. Peden, J. Macht, E. Iglesia, *J. Catal.* **2006**, 239, 200.

[137] C. Sun, S. Liu, D. Liang, K. Shao, Y. Ren, Z. Su, *J. Am. Chem. Soc.* **2009**, 131, 1883.

[138] C. C. Hwang and C. Y. Mou, *J. Phys. Chem. C*, **2009**, 113, 5212-5221.

[139] A.S. Khder, E.A. El-Sharkawy, S.A. El-Hakam, A.I. Ahmed, *Catal. Comm.* **2008**, 9, 769.

[140] S. L. Barbosa, M. J. Dabdoub, G. R. Hurtado, S. I. Klein,A. C.M. Baroni, C. Cunha, *Appl. Catal. A*, **2006**, 313, 146.

[141] A. E. R. S. Khder, *Appl. Catal. A*, **2008**, 343, 109.

국 문 초 록

바이오매스를 이용한 정밀화학물질의 생산은 기존의 석유화학공정을 대체할 수 있는 방법으로서 각광을 받고있다. 석유와 다르게 바이오매스로부터 유래하는 원재료는 많은 양의 산소를 포함하고 있기 때문에 기존에 석유로부터 생산하던 화학물질을 얻기 위해서는 이 산소의 선택적인 제거가 매우 중요하다. 탈수반응, 에스테르화 반응과 같이 물이 제거되는 탈수적 반응들은 바이오매스 유래 물질로부터 산소를 제거함과 동시에 생성물질에 원하는 기능기를 도입할 수 있기 때문에 위의 목적에 부합하는 효과적인 방법이다. 이 논문에서는 바이오매스로부터 유래하는 C4 화학물질의 전환을 위한 비균일계 탈수적 촉매 공정에 대해 연구하였다.

첫 번째로 바이오매스로부터 유래하는 2,3-부탄디올을 2,3-에폭시부탄으로 전환시킬 수 있는 새로운 탈수반응(탈수적 에폭시화반응)과 이를 이용한 1,3-부타디엔 생산을 위한 비균일계 촉매공정에 대해 논의하고자 한다. 이 탈수반응은 염기성 물질이 담지된 촉매에서 활성을 보이며, 특히 세슘이 담지된 실리카(CsO_x/SiO_2) 촉매가 가장 높은 활성을 보이는 것으로 나타났다. CsO_x/SiO_2 촉매의 높은 활성에 대한 원인을 확인하기 위해 다양한 분석툴을 이용한 구조-활성 관계를

찾고자 하였다. 또한 새로운 반응이 어떤 메커니즘으로 일어나는지를 알기 위해 밀도범함수이론(density functional theory, DFT) 계산을 이용하여 이론적으로 해석하고자 하였다. 분석결과 CsO_x/SiO_2 촉매의 높은 활성의 원인은 다음과 같은 요소들이 복합적으로 작용하였음을 확인하였다: i) Cs^+의 담지로 인한 강한 산점의 생성, ii) Cs^+ 이온의 큰 크기로 인해 SiO_2 내부로 침투하지 않기 때문에 생성된 염기점이 표면에서 반응물과 용이하게 접촉가능, iii) SiO_2 담체와 Cs^+의 강한 결합으로 인한 안정적인 염기점의 생성, iv) 약한 산성을 띠는 SiO_2 표면이 탈수반응을 용이하게 함. 또한 탈수적 에폭시화반응은 meso-2,3-butanediol (R,S)이 trans-2,3-epoxybutane (R,R or S,S)으로 전환되는 키랄성의 변화를 가져오는 S_N2 유사 반응 메커니즘을 따르며, 이는 DFT모사 결과와도 일치하였다. 2,3-부탄디올의 탈수적 에폭시화반응을 통해 생성된 2,3-에폭시부탄은 다른 정밀화학물질의 생산에도 유용하게 활용될 수 있다. 염기성 리튬포스페이트 촉매를 이용하여 반응하였을 때, 2,3-에폭시부탄이 높은 선택도를 보이며 3-부텐-2-올로 전환되는 것을 확인하였다. 여기에 더해, 3-부텐-2-올은 1,3-부타디엔을 생산하기에 매우 적합한 전구체로서 작용하며, 산성을 띠는 중형기공성 알루미노실리케이트 촉매를 이용할 경우 매우 높은 수율을 나타내는 것을 확인하였다.

마지막으로, 산촉매작용을 통해 일어나는 1-부탄올의 에스테르화반응용 고활성촉매를 설계 및 제조하였다. 카르복실산과의 에스테르화를 통해 1-

부탄올은 다양한 종류의 에스터로 전환될 수 있는데, 이들은 환경친화적인 용매, 혹은 향수의 전구체로서 매우 유용하게 활용될 수 있다. 현재 대부분의 에스테르화 반응은 황산과 같은 균일계 산촉매를 이용하여 이루어지는데, 이런 균일계 산촉매의 사용은 반응기의 부식, 그리고 환경적인 문제를 야기한다. 따라서 현재의 문제점을 해결하기 위해서는 비균일계 촉매의 개발이 시급한 실정이다. 이와 관련하여 이 연구에서는 텅스텐산화물 담지 지르코늄 촉매에 주목했다. 이 촉매는 알코올의 탈수반응, 알칸의 이성질화 반응에 좋은 활성을 보이는 것으로 알려졌는데, 이는 촉매표면에 생성되는 Zr−WO_x 클러스터가 높은 산특성을 보이기 때문이라고 밝혀졌다. 하지만 현재 이 Zr−WO_x 클러스터를 높은 밀도로 가지고 있는 촉매를 제조하기 위한 방법에 대해서는 연구가 부족한 실정이다. 이 연구에서는 Zr−WO_x 클러스터를 높은 밀도로 제조하기 위한 중형기공성 Zr−WO_x/SiO_2 촉매를 제안하고, 이 촉매에서 Zr/W의 비율에 따른 구조와 산특성을 조사하였다. 순차적인 지르코늄과 텅스텐의 가수분해와 soft−templating을 통해 강한 산성을 나타내는 Zr−WO_x 클러스터가 균일하게 분포한 중형기공 구조의 물질을 제조하였다. 제조된 Zr−WO_x/SiO_2 촉매의 특성을 질소흡착, XRD, TEM, XPS, UV−Vis분광법, NH_3−TPD, *in−situ* FTIR로 분석하였다. 이 물질은 500 m^2/g 이상의 높은 표면적과 균일하게 정렬된 5 nm의 원통형 기공구조를 가지고 있었다. Zr/W의 비율이 0.5보다 작을 때 지르코늄은 주로 텅스테이트와 함께

존재하는 것이 확인이 되었으며, 이는 Zr−WO_x 클러스터가 주로 형성되었음을 의미한다. 가장 높은 Zr−WO_x 밀도는 Zr/W 비율이 0.3일 때 나타났으며, 또한 가장 강한 Brønsted 산특성을 보였다. 결과적으로 Zr/W 비율이 0.3인 Zr−WO_x/SiO_2촉매가 1−부탄올과 아세트산의 에스테르화 반응에 가장 높은 활성을 보였으며, 이 활성은 기존의 HZSM−5, WO_x/ZrO_2 촉매보다 월등하였다.

주요어: 비균일계 촉매작용, 탈수반응, 에스테르화반응, 반응 메커니즘, 촉매 프로세스
학 번: 2011-30277

List of publications

International Publications

International Academic Published Papers (First Author)

1. T. Y. Kim*, J. Baek*, C. K. Song, Y. S. Yun, D. S. Park, W. Kim, J. W. Han, J. Yi, "Gas-phase Dehydration of Vicinal Diols to Epoxides: From a Mechanism to a Practical Application", *Journal of Catalysis* 2015, 323, 85-99.

   (* Tae Yong Kim and Jayeon Baek contributed equally to this work)

2. D. Yun*, T. Y. Kim*, D. S. Park, Y. S. Yun, J. W. Han, J. Yi (*co-first author) , "A Tailored Catalyst for the Sustainable Conversion of Glycerol to Acrolein: Mechanistic Aspect of Sequential Dehydration", ChemSusChem 2014, 7(8), 2193-220.

   (* Tae Yong Kim and Danim Yun contributed equally to this work)

3. J. Baek*, T. Y. Kim*, W. Kim, H. J. Lee, J. Yi (*co-first author), "Selective production of 1,3-butadiene using glucose fermentation liquor", *Green Chemistry* 2014, 16(7), 3501-3507.

   (* Tae Yong Kim and Jayeon Baek contributed equally to this work)

4. T. Y. Kim, D. S. Park, Y. Choi, J. Baek, J. R. Park, J. Yi, "Preparation and characterization of mesoporous Zr-WO_x/SiO_2 catalysts for the esterification of 1-butanol with acetic acid", *Journal of Materials Chemistry* 2012, 22(19), 10021-10028.

International Academic Published Papers (Co-author)

1. J. Baek*, S. Park*, C. K. Song, T. Y. Kim, I. Nam, J. M. Lee, J. W. Han, and J. Yi, 'Radial alignment of c-channel nanorods in 3D porous TiO_2 for eliciting enhanced Li storage performance", *Chemical Communications* 2015, 51, 15019-15022.

2. H. Park, Y. S. Yun, T. Y. Kim, K. R. Lee, J. Baek, J. Yi, "Kinetics of the dehydration of glycerol over acid catalysts with an investigation of deactivation mechanism by coke", *Applied Catalysis B: Environmental* 2015, 176, 1-10.

3. Y. S. Yun, K. R. Lee, H. Park, T. Y. Kim, D. Yun, J. W. Han, J. Yi, "Rational Design of a Bi-functional Catalyst for the Oxydehydration of Glycerol: A Combined Theoretical and Experimental Study", *ACS Catalysis* 2015, 5, 82-94.

4. D. S. Park*, D. Yun*, T. Y. Kim, J. Baek, Y. S. Yun, J. Yi, "A Mesoporous Carbon-Supported Pt Nanocatalyst for the Conversion of Lignocellulose to Sugar Alcohols", *ChemSusChem* 2013, 6(12), 2281-2289.

5. D. S. Park, D. Yun, Y. Choi, T. Y. Kim, S. Oh, J.-H. Cho, J. Yi, "Effect of 3D open-pores on the dehydration of n-butanol to di-n-butyl ether (DNBE) over a supported heteropolyacid catalyst", *Chemical Engineering Journal*, 2013, 228, 889-895.

6. J. R. Park, B. K. Kwak, D. S. Park, T. Y. Kim, Y. S. Yun, J. Yi, "Effect of Acid Type in WO_X clusters on The Esterification of Ethanol with Acetic Acid", *Korean Journal of Chemical Engineering*, 2012, 29(12), 1695-1699.

Patents Application on File

1. 이종협, 백자연, 박수민, 송찬경, 김태용, 남인호, "삼차원 구조의 구형 타이타니아 제조방법", 특허 출원 10-2015-0133388 (2015.09.21)
2. 이종협, 김태용, 박대성, 최영보, 백자연, 박재률, "균일한 중형 기공을 갖는 복합 산화물 촉매, 그 제조 방법 및 상기 촉매를 이용하여 에스테르 화합물을 제조하는 방법", 특허 출원 10-2012-0053823 (2012.05.21)

International Conferences (First author)

1. T. Y. Kim, J. Baek, C. K. Song, Y. S. Yun, D. S. Park, W. Kim, J. Yi, "Production of 1,3-butadiene from 2,3-butanediol using cesium oxide supported silica catalyst", 24th

North American Meeting of the Catalysis Society, Pittsburgh, PA, USA, Jun. 14-19, 2015.

2. T. Y. Kim, J. Baek, C. K. Song, J. M. Lee, J. W. Han, and J. Yi, "Heterogeneous Catalytic Process for the Production of 1,3-Butadiene from 2,3-Butanediol", The 15th Korea-Japan Symposium on Catalysis, Busan, Korea, May. 26-28, 2015.

3. T. Y. Kim, J. Baek, C. K. Song, Y. S. Yun, D. S. Park, J. Yi, "Density Functional Theory Study on Conversion of Biomass Derived 2,3-Butanediol to 2,3-Epoxybutane", The Korean Society of Clean Technology 2014 Fall Meeting, Gyeongju, Korea, Sep. 24-26, 2014.

4. T. Y. Kim, J. Baek, W. Kim, W. K. Synn, H. J. Lee, J. Yi, "Novel catalytic routes for the selective production of 1,3-butadiene from biomass derived 2,3-butanediol", The 14th Japan-Korea Symposium on Catalysis, WINC Aichi, Nagoya, Japan, July 1-3.

5. T. Y. Kim, S. Yu, J. Baek, J. Yi, "Effect of Zr/W ratio on mesoporous Zr-WO_x/SiO_2 as a solid acid: Formation and optimization of Zr-WO_x clusters", 244th American Chemical Society National Meeting & Exposition, Philadelphia, PA, USA, Aug.19-23, 2012.

International Conferences (Co-author)

1. Y. S. Yun, K. R. Lee, T. Y. Kim, D. Yun, J. W. Han, J. Yi, "Bi-functional Mo-V-W-O catalysts for the one-step production of acrylic acid from glycerol and verification via first principle calculations", 24th North American Meeting of the Catalysis Society, Pittsburgh, PA, USA, Jun. 14-19, 2015.

2. D. Yun, T. Y. Kim, Y. S. Yun, J. M. Lee, J. W. Han, and J. Yi, "Ab initio study of the surface model of amorphous aluminosilicate", The 15th Korea-Japan Symposium on Catalysis, Busan, Korea, May. 26-28, 2015.

3. Y. S. Yun, T. Y. Kim, D. Yun, H. Park, J. M. Lee, J. W. Han, and J. Yi, "Mechanistic insight of hydrogenolysis of glycerol over Cu-based catalysts via ab initio

calculations", The 15th Korea-Japan Symposium on Catalysis, Busan, Korea, May. 26-28, 2015.

4. J. Baek, T. Y. Kim, Y. S. Yun, and J. Yi, "Heterogeneous Catalytic Conversions of Alcohols/polyols Derived from Biomasses to Fine Chemicals", The 15th Korea-Japan Symposium on Catalysis, Busan, Korea, May. 26-28, 2015.

5. S. Park, J. Baek, C. K. Song, T. Y. Kim, I. Nam, J. W. Han, and J. Yi, "Rational design of 3D TiO_2 for use in Li-ion battery", 227th ECS Meeting, Chicago, Illinois, USA, May. 24-28, 2015.

6. C. K. Song, J. Baek, T. Y. Kim, S. Yu, J. Yi, "Synthesis of 3D Hierarchical TiO_2 and Its Application to Phenol Photodegradation Reaction", The Korean Society of Clean Technology 2014 Fall Meeting, Gyeongju, Korea, Sep. 24-26, 2014.

7. J. Baek, T. Y. Kim, I. Nam, S. Park, S. Yu, S. Bae, S. Y. Lee, H. N. Umh, Y. H. Kim, J. Yi, "Production of valuable chemicals (1,3-butadiene) from biomass-based resources alternative to the petroleum", 248th American Chemical Society National Meeting & Exposition, San Francisco, CA, USA, Aug. 10-14, 2014.

8. D. S. Park, D. Yun, Y. S. Yun, H. Park, T. Y. Kim, J. Baek, J. Yi, "Direct conversion of lignocellulose to sugar alcohols over Pt supported on a new 3D mesoporous carbon", 247th American Chemical Society National Meeting & Exposition, Dallas, Texas, USA, Mar. 16-20, 2014.

9. D. S. Park, D. Yun, Y. Choi, T. Y. Kim, S. Oh, J.-H. Cho, and J. Yi, "Enhancement of Mass Transport over 3D Open-porous Dandelion-like Catalyst in Liquid-phase Heterogeneous Catalysis", 9th World Congress of Chemical Engineering, Coex, Seoul, Korea, August 18-23, 2014.

10. J. Baek, T. Y. Kim, W. Kim, W. K. Synn, H. J. Lee, J. Yi, "New synthetic pathway for the catalytic production of 1,3-butadiene using 2,3-butanediol and succinic acid derived from glucosic biomass", The 14th Japan-Korea Symposium on Catalysis, WINC Aichi, Nagoya, Japan, July 1-3.

11. D. Yun, D. S. Park, T. Y. Kim, S. Oh, Y. A. Shin, J. Yi, ”Preparation of DSS-SO_3H Catalyst for Stable Production of Acrolein from Glycerol”, The 14th Japan-Korea Symposium on Catalysis, WINC Aichi, Nagoya, Japan, July 1-3.

Domestic Conferences

1. 김태용, 백자연, 윤양식, 박대성, 문원균, 김우영, 한정우, 이종협, “비시널 디올의 탈수반응을 통한 에폭사이드 화합물의 생성 및 이를 통한 바이오매스 유래 2,3-부탄디올로부터 1,3-부타디엔 생산”, 추계 한국화학공학회, 대전컨벤션센터, 10. 23-24 (2014)
2. 윤양식, 이경록, 박홍석, 김태용, 윤다님, 서영종, 김왕규, 이중원, 한정우, 이종협, “글리세롤의 산화탈수반응을 위한 이원기능촉매 개발 및 적용”, 추계 한국화학공학회, 대전컨벤션센터, 10. 23-24 (2014)
3. 송찬경, 백자연, 김태용, 유성주, 이종협, “계층 구조를 가진 3차원 TiO2의 제조 및 이를 이용한 페놀 광분해 반응에의 응용”, 추계 한국청정기술학회, 경주 K호텔, 9 .24-26 (2014)
4. 김태용, 백자연, 송찬경, 윤양식, 박대성, 이종협, “밀도범함수이론을 이용한 바이오매스 유래 2,3-부탄디올의 2,3-에폭시부탄으로의 전환에 대한 연구”, 추계 한국청정기술학회, 경주 K호텔, 9. 24-26 (2014)
5. 윤다님, 김태용, 박대성, 윤양식, 이종협, 한정우, 오석일, 신용안, “글리세롤로부터 아크롤레인을 안정적으로 생산하기 위한 맞춤형 촉매 개발’, 춘계 한국화학공학회, 창원컨벤션센터, 4. 23-25 (2014)
6. 백자연, 김태용, 박대성, 박홍석, 송찬경, 이경록, 이종협, “글루코오스 발효액으로부터의 1,3-부타디엔 생성”, 춘계 한국화학공학회, 창원컨벤션센터, 4. 23-25 (2014)
7. 윤다님, 김태용, 박대성, 윤양식, 한정우, 이종협, “열린 기공 구조를 갖는 브뢴스테드 산촉매의 제조 및 글리세롤 탈수반응에의 적용’, 춘계 한국청정기술학회, 여수경도리조트, 3. 27-28 (2014)
8. 윤양식, 박홍석, 윤다님, 박대성, 김태용, 백자연, 이경록, 이종협, “계층구조를 갖는 나노크기의 고체산촉매 제조 및 응용”, 춘계 한국청정기술학회,

여수경도리조트, 3. 27-28 (2014)

9. 백자연, 김태용, 송찬경, 이종협, “글루코오스 발효액을 이용한 1,3-부타디엔 생성 반응”, 춘계 한국청정기술학회, 여수경도리조트, 3. 27-28 (2014)
10. 김태용, 백자연, 송찬경, 윤양식, 박대성, 한정우, 이종협, “바이오매스 유래 물질의 맞춤형 탈수반응을 위한 비시널 디올로부터 에폭사이드 유래 물질 생성”, 춘계 한국청정기술학회, 여수경도리조트, 3. 27-28 (2014)
11. 백자연, 송현돈, 김태용, 박대성, 윤다님, 윤양식, 박홍석, 이종협, “금 나노입자의 암모니아 보란을 이용한 4-니트로페놀 환원 반응에서의 실시간 전자이동 관찰”, 추계 한국청정기술학회, 제주한화리조트, 9. 25-27 (2013)
12. 윤양식, 박대성, 윤다님, 김태용, 오석일, 이종협, “무수소 조건에서의 글리세롤의 가수소분해 반응을 위한 중형기공 알루미나에 담지된 구리-니켈 이중금속촉매의 제조 및 적용’, 춘계 한국청정기술학회, 여수 경도리조트, 3. 28-29 (2013)
13. 김태용, 백자연, 김우영, 신우균, 이희종, 이종협, “고부가가치 1,3-부타디엔의 생산을 위한 바이오매스 유래 2,3-부탄디올의 전환 및 이를 위한 촉매 공정”, 춘계 한국청정기술학회, 여수경도리조트, 3. 28-29 (2013)
14. 백자연, 윤다님, 최영보, 김태용, 김우영, 이희종, 김영훈, 이종협, “이산화탄소/프로판을 원료로 사용하는 프로필렌 제조용 촉매 공정 개발 1. 고효율 촉매 설계 및 제조”, 추계 한국청정기술학회, 영남대학교, 11. 16 (2012)
15. 김태용, 박대성, 백자연, 최영보, 김영훈, 이종협, “바이오매스 유래 알코올과 유기산의 고부가가치용 촉매개발 연구”, 추계 한국청정기술학회, 영남대학교, 11. 16 (2012)
16. 김태용, 박대성, 최영보, 백자연, 이종협, “바이오매스로부터 고부가가치 화학물질 제조와 중형기공성 Zr-WO_x/SiO_2 촉매의 개발”, 춘계 한국청정기술학회, 연세대학교, 5.25 (2012)
17. 김태용, 박대성, 최영보, 백자연, 박재률, 이종협, “부탄올 에스테르화 반응을 위한 중형기공의 Zr-WO_x/SiO_2 촉매의 제조 및 특성 분석”, 춘계 한국화학공학회, 제주국제컨벤션센터, 4.25-27 (2012)
18. 박대성, 곽병규, 김태용, 박재률, 윤양식, 이종협, “다공성 구형 실리카에 담지된 헤테로폴리산 촉매의 제조 및 불균일 촉매반응에의 적용”, 추계 한국

화학공학회, 송도컨벤시아, 10. 26-28 (2011)

19. 곽병규, 박대성, 박재률, 윤양식, 김태용, 이종협, “폐글리세롤 수소첨가분해 반응용 $CuCr_2O_4$ 촉매에서 조촉매의 효과”, 추계 한국화학공학회, 송도컨벤시아, 10. 26-28 (2011)

공학박사 학위논문

Heterogeneous Catalytic Dehydrative Reactions for the Conversion of Biomass-derived C4 Chemicals

바이오매스로부터 유래하는 C4 화학물질의 전환을 위한 비균일계 탈수적 촉매반응

2016년 2월

서울대학교 대학원

화학생물공학부

김 태 용

Abstract

Heterogeneous Catalytic Dehydrative Reactions for the Conversion of Biomass-derived C4 Chemicals

Tae Yong Kim
School of Chemical and Biological Engineering
The Graduate School
Seoul National University

The utilization of biomass for the production of fine chemicals has been attracted as an alternative way to conventional petrochemical processes. As biomass-derived feedstocks contain abundant oxygen atoms, selective removal of oxygen is required to produce fine chemicals previously obtained from petroleum. Dehydrative reactions such as dehydration and esterification are effective to reduce oxygen content of biomass-derived feedstock as well as to produce desired functional groups. In this thesis, heterogeneous dehydrative reactions for the conversion of biomass-derived C4 chemicals including 2,3-butanediol and 1-butanol are studied.

At first, a novel type of dehydration reaction that produces 2,3-epoxybutane from 2,3-butanediol (dehydrative epoxidation) is discovered and explored. Among a number of tested basic catalysts, the CsO_x/SiO_2 catalyst showed outstanding performance for the dehydrative epoxidation of 2,3-butanediol and is considered to be the most promising catalyst for this type of reaction. In order to identify the superiority of the CsO_x/SiO_2 catalyst and a mechanism of the reaction, structure-activity relationships were studied along with density

functional theory (DFT) calculations. The following features are found to be responsible for the excellent activity of the CsO_x/SiO_2 catalyst: i) strong basic sites formed by Cs^+, ii) low penetration of Cs^+ into SiO_2 which permits basic sites to be accessible to the reactant, iii) stable basic sites due to the strong interactions between Cs^+ and SiO_2 surface, and iv) mildly acidic surface of SiO_2 which is advantageous for the elimination to H_2O. In addition, the dehydrative epoxidation involves an inversion of chirality (e.g. *meso*-2,3-butanediol (*R,S*) to *trans*-2,3-epoxybutane (*R,R* or *S,S*)), which is in agreement with DFT results that the reaction follows a stereospecific S_N2-like mechanism.

The 2,3-epoxybutane produced from the dehydrative epoxidation of 2,3-butanediol can be further utilized to produce fine chemicals. When 2,3-epoxybutane was reacted over basic lithium phosphate catalyst, isomerized product, 3-buten-2-ol, was obtained with high selectivity. Furthermore, it was found that 3-buten-2-ol is an ideal precursor for the production of 1,3-butadiene. Reaction of 3-buten-2-ol over acidic mesoporous aluminosilicate (Al-MCM-41) led to dominant formation of 1,3-butadiene via acid-catalyzed dehydration. On the basis of the results, heterogeneous catalytic process for the production of 1,3-butadiene from 2,3-butanediol is proposed.

Esterification of 1-butanol with carboxylic acid produces various esters which can be utilized to environmentally friendly solvents and precursors for fragrances. Esterification reactions are industrially conducted with homogeneous mineral acid catalysts, which causes process and environmental problems. Heterogeneous acid catalyst for the esterficiation reactions is essential to overcome the current problems. Zr-WO_x clusters on WO_x/ZrO_2 catalyst are known to be active sites for the acid catalyzed reactions, such as dehydration of alcohols and alkane isomerization reactions. However synthetic methods for producing high density of Zr-WO_x clusters with high surface areas are not currently available. A facile method for preparing mesoporous Zr-WO_x/SiO_2 is proposed and the effect of Zr/W ratio on its structure and acidity

was examined. Results showed that the sequential hydrolysis of zirconium and tungsten via soft-templating resulted in the formation of Zr-WO_x clusters with uniform mesopore structures and a high acidity. The prepared Zr-WO_x/SiO_2 was characterized by N_2 physisorption, XRD, TEM, XPS, UV-Vis spectroscopy, NH_3-TPD and in-situ FTIR. Catalytic performance for the esterification of 1-butanol with acetic acid was evaluated. The materials had a high surface area of over 500 m^2/g and ordered cylindrical pores with a uniform size of ca. 5 nm. Below a Zr/W ratio of ≈0.5, the zirconium was primarily associated with tungstate rather than SiO_2, which indicates the formation of Zr-WO_x clusters. The highest density of Zr-WO_x clusters was obtained at a Zr/W ratio of 0.3 with a strong Brønsted acidity. Consequently, Zr-WO_x/SiO_2, as a Zr/W ratio of 0.3 exhibited the highest activity with a significantly improved performance compared to HZSM-5 and WO_x/ZrO_2 catalysts.

Keywords: Heterogeneous catalysis, dehydration, esterification, reaction mechanism, catalytic process

Student Number: 2011-30277

Contents

List of Tables

List of Figures

List of Schemes

Chapter 1. Introduction

1.1 Biomass as a source for chemical production

With growing demand for sustainability of chemical processes, the catalytic conversion of biomass to value-added chemicals has been raised as an alternative to conventional petrochemical processes [1]. Since biomass-derived feedstocks contain abundant oxygen atoms (O/C ratio up to 0.6 for woody biomass [2]), as opposed to petrochemical feedstocks (O/C ratio less than 0.02 [3]), the selective removal of oxygen is a central challenge for producing valuable chemicals using biomass sources [4-6]. In this connection, dehydrative reactions, such as dehydration and esterification, play a key role in the reduction of abundant oxygen from biomass-derived feedstocks. For example, in the case of the production of HMF from glucose [7,8] and furfural from xylose [8-10], half of the oxygen atoms in sugars are effectively removed by dehydration reactions.

In the aspect of chemical structure, hydroxyl and carboxylic acid groups are two major chemical structure present in biomass-derived feedstocks. Therefore, dehydration and esterification reactions also have significance in the formation of desirable functional groups as well as the removal of oxygen atoms. Hydroxyl groups in biomass-derived feedstocks can be effectively converted into functional groups, such as C=C and C=O bonds, via dehydration. The formation of such functional groups by dehydration made it possible to produce

DMF [11,12], γ-valerolactone [13], alkanes and alkenes [14] from biomass-derived feedstocks. In addition, the consecutive dehydration of glycerol led to the formation a C=O bond (3-hydroxypropionaldehyde) followed by C=C bond formation, resulting in the production of acrolein which is a valuable precursor for the production of acrylic acid [15-17]. On the other hand, esterification reaction is useful to convert carboxylic acid group to ester group. The esterification can produce esters from biomass-derived carboxylic, acids such as lactic acid, succinic acid, itacconic acid, and glutamic acid. The produced esters are potentially useful to solvent liquid as they have non-toxic, bio-degradable, and high-boiling properties [18].

1.2 C4 feedstocks derived from biomass

2,3-Butanediol is the longest chain alcohol found as natural major end product of microbial fermentation along with butanol. Harden and Walpole first reported the production of 2,3-butanediol from microbial fermentation [19]. It is generally synthesized via mixed acid fermentation of pathogenic bacteria such as *Klebsiella pneumonia*, *Klebsiella oxytoca*, *Enterobacter aerogenes*, and *Paenibacillus polymyxa* [20-23]. These bacteria are useful to produce 2,3-butanediol with high yields and productivities, but large-scale fermentation is quiet difficult due to their pathogenic properties. The use of non-pathogenic *Saccharomyces cerevisiae* is considered to be desirable as an alternative. This microbial fermentation is proceeded through several intermediate compounds such as α-acetolactate, diacetyl, and acetoin (Figure 1-1). Other side products, i.e. ethanol, acetate, formate, lactate, and succinate are also synthesized depending on the applied conditions or types of microorganisms. However, microbial fermentation using *Saccharomyces cerevisiae* led to low productivity and yield so that several attempts to improve 2,3-butanediol production have been tried [24-27].

Butanol has been traditionally produced by ABE fermentation which is an anaerobic conversion of carbohydrates by metabolically engineered strains of *Clostridium* into acetone, butanol, and ethanol [28-35]. As two major global corporations, BP and Dupont reported to start butanol production by

fermentation of sugar beet in June 2006 and established the joint-venture Butamax^{TM} Biofuels LLC in 2009, the production of butanol is expected to grow rapidly. On October 2, 2013, Butamax announced that the production facilities for biobutanol has been constructed by simple retrofit of existing Highwater Ethanol' plant in Lamberton, Minnesota [36]. Biobutanol can be produced from cereal crops, sugar cane and sugar beet, etc, but can also be produced from cellulosic raw materials [37].

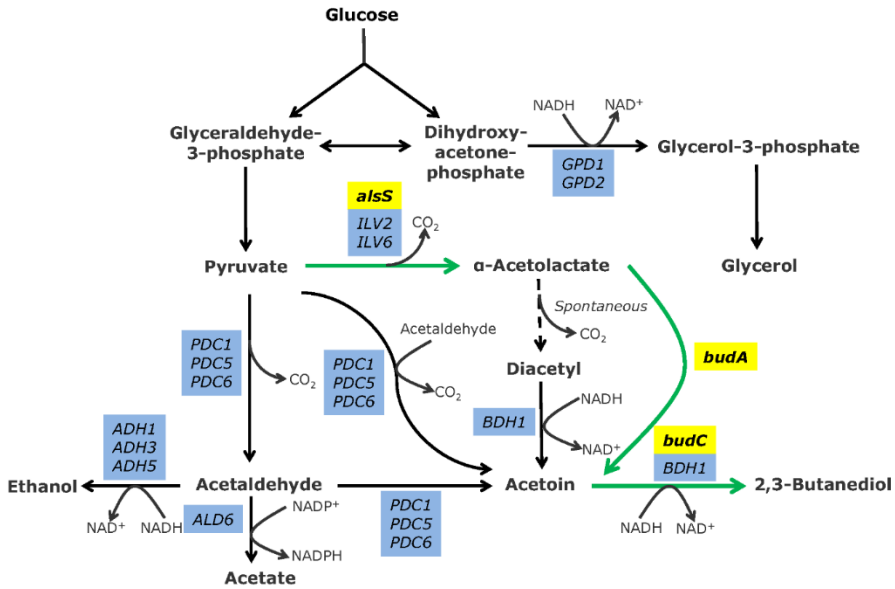

Figure 1-1. Metabolic pathways for the synthesis of 2,3-butanediol in *Saccharomyces cerevisiae*. Green arrow show the bacterial 2,3-butanediol synthesis pathway through α-acetolactate decarboxylase. Blue boxes contain the Saccharomyces cerevisiae innate genes, while yellow boxes indicate the foreign genes introduced to the engineered strains. Figure is reprinted from [35]

1.3 Catalytic dehydrative reactions

Different from petroleum based feedstocks, biomass derived feedstocks contain a plenty of oxygen as a form of alcohol, carboxylic acid, aldehyde, and ketone. Therefore, oxygen removal has to be involved in the conversion of biomass to produce fine chemicals that are derived from petroleum. The dehydrative reaction is advantageous solution to reduce oxygen content as well as to produce chemicals with desired functionality.

1.3.1 Dehydration of 2,3-butanediol and the production of 1,3-butadiene

1,3-butadiene is one of essential monomers for polymer synthesis, and has been solely produced via petrochemical process. Production of 1,3-butadiene from biomass derived feedstock is of great importance in that a renewable resource is utilized as opposed to a petrochemical process. In this regard, 2,3-butanediol has been recognized as an attractive biomass derived feedstock for 1,3-butadiene production [38], because elimination of two water molecules from 2,3-butanediol can lead to the formation of 1,3-butadiene.

Homogeneous catalytic process for the production of 1,3-butadiene from 2,3-butanediol was previously reported in 1945 by S. Marshak et al. [39], and was recently studied in more detail in our group [40]. This process is sequential

esterification of 2,3-butanediol and pyrolysis of produced ester. The esterification of 2,3-butanediol can take place with carboxylic acids like acetic acid and formic acid using H_2SO_4 as a homogeneous catalyst, and produces mono- and di-ester. The di-ester is thermally activated in the pyrolysis step, resulting in the formation of 1,3-butadiene. This process can produce 1,3-butadiene from 2,3-butanediol with high yield ~ 80%, but utilization of homogeneous mineral acid can cause corrosion, separation, and environmental problems. Therefore, a heterogeneous catalytic process is highly desired to realize the production of 1,3-butadiene from 2,3-butanediol.

Acid catalyzed dehydration is conventional and the first choice for heterogeneous catalytic dehydration of alcohols. However, in the case of 2,3-butanediol, the acid catalyzed dehydration resulted in formation of methyl ethyl ketone and isobutraldehyde, which contain unreactive C=O bonding and hamper further dehydration to 1,3-butadiene. Therefore, a novel catalytic route, not based on acid catalysis, is required to realize the heterogeneous catalytic pocess for the production of 1,3-butadiene from 2,3-butanediol.

1.3.2 Esterification of 1-butanol with acetic acid

Industrial esterification processes have utilized homogeneous acid catalysts such as H_2SO_4 and HCl.[41] The homogeneous process provides good productivity with cheap catalysts, but has drawbacks including difficult

separation and severe corrosion problems. Therefore, it is highly desirable to replace the current homogeneous process to heterogeneous one by adopting solid acid catalysts.

There are various options for solid acid catalysts, including zeolites, aluminosilicates, acidic oxides, supported heteropoly acids, ion-exchange resins, and so on. Peters et al. compared several commercial acid catalysts for the liquid phase esterification of acetic acid with butanol [41]. It was found that ion-exchange resins were better performed than zeolites and superacids. The apparent rate constant per acid site for ion-exchange resins, recalculated from data in ref 41, was $3.4 \cdot 10^{-6}$ and $7.1 \cdot 10^{-6}$ $m^3\ mol^{-2}\ s^{-1}$ for Amberlyst 15 and Smopex-101, respectively. These values are slightly lower than sulfuric acid ($2.0 \cdot 10^{-5}$ $m^3\ mol^{-2}\ s^{-1}$) and p-toluenesulfonic acid ($1.0 \cdot 10^{-5}$ $m^3\ mol^{-2}\ s^{-1}$), and are comparable with phosphomolybdic acid ($7.0 \cdot 10^{-6}$ $m^3\ mol^{-2}\ s^{-1}$). In contrast, the apparent rate constant per acid site for zeolites was considerably lower than ion-exchange resin, except for H-USY zeolite which has relatively large pores. The authors proposed that internal diffusion in pores of zeolite limited the reaction. Sulfated zirconia exhibited rate constant similar to Amberlyst 15, but its acid contents were 10-times lower than ion-exchange resin thus much more catalysts were required to achieve similar acid amount.

On the other hand, strength of acid sites is also important requirement for

appropriate catalyst. Corma et al. studied the influence of Si/Al ratio of HY zeolites on the esterification of ethanol with phenylacetic acid [42]. The authors observed increase in activity with increasing Si/Al ratio, which indicates that esterification only takes place at strongly acidic sites. Similar trend was also reported by Peters et al. [41].

On the basis of the literature survey, it can conclude that sufficiently large pore size and strong acid sites are required for esterification catalyst. These required properties make one image mesoporous material with high density of strong acid sites as an ideal catalyst for esterification reaction. Regarding to strongly acidic material, I focused on tungstated zirconia (WO_x/ZrO_2). Tungstated zirconia (WO_x/ZrO_2) catalysts have attracted interest, since Hino and Arata first discovered their strong acidity and low-temperature activity for light alkane isomerization [43] It has been reported to have a high activity for alkane isomerization and the dehydration of alcohols [44-46]. Furthermore, the higher thermal and chemical stabilities of WO_x/ZrO_2 make them attractive for use in a variety of industrial processes [43,46]. It is generally accepted that the strong acidity is due to the strong interaction between zirconia and tungstate or by the presence of Zr-WO_x clusters. Although the origin of strong acidity was identified, methods for improving the activity of WO_x/ZrO_2 catalysts are not available. High surface area mesoporous material combined with active site of WO_x/ZrO_2 can be an ideal catalyst for esterification reaction.

1.4. Objectives

Catalytic conversion of biomass to replace petrochemical processes has become an important issue in the field of catalysis. Current limitations in the conversion of biomass are closely related to the large oxygen contents in biomass. Removal of oxygen atoms is basically required to produce fine chemicals, but catalytic routes as well as known catalytic materials are insufficient to create efficient catalytic process for the biomass conversion.

In this regard, the objective of this thesis is achieving efficient catalytic conversion of biomass-derived 2,3-butanediol and 1-butanol through discovery of a novel catalysis, understanding of reaction mechanism, and development of highly active catalyst.

A novel dehydration reaction which produces 2,3-epoxybutane from 2,3-butanediol is first discovered and studied. Required characteristics for an active catalyst and reaction mechanism are proposed based on experimental results and theoretical calculations. On the basis of this novel reaction, heterogeneous catalytic process for the production of 1,3-butadiene from 2,3-butanediol is proposed.

Design and synthesis of an active catalyst for the esterification of 1-butanol with acetic acid is studied. The synthesized catalyst, mesoporous Zr-WO_x/SiO_2, exhibited high surface area and high density of strong acid site. Thanks to these properties, the catalyst showed promising catalytic performance.

Chapter 2. Dehydrative Epoxidation of 2,3-butanediol and Heterogeneous Catalytic Process for the Production of 1,3-butadiene

2.1 Introduction

2,3-butanediol is an attractive biomass-derived feedstock to produce C4 fine chemicals. Researches on the catalytic dehydration of 2,3-butanediol have received little attention, and only few studies have been reported on this issue. Several studies on dehydration of 2,3-butanediol to 3-buten-2-ol were reported [47], but most of the reports related to this subject have been limited to acid catalyzed dehydration, yielding aldehydes and ketones [48-54]. Such restricted uses and studies will not be sufficient to identify efficient reaction pathways for biomass conversion for replacing conventional petrochemical products. In this regard, the discovery of novel dehydration reactions of vicinal diols has the potential to open up new possibilities for the utilization of biomass, and thereby has the potential to expand the scope of chemicals that can be produced from biomass.

Herein, a novel dehydration reaction of 2,3-butanediol (**BD**), leading to the formation of 2,3-epoxybutane (**EB**), is reported. Since the reaction involves the formation of an epoxide ring with the elimination of H_2O, the reaction is referred as 'dehydrative epoxidation'. At first, dehydrative epoxidation of

vicinal diols, including ethylene glycol, 1,2-propanediol, and **BD**, was performed and was compared with previously reported dehydration reactions. A series of active catalysts were screened for the dehydrative epoxidation of **BD**, and the optimum catalyst was identified. The acidic-basic and physicochemical properties of the catalysts were characterized, in order to identify the cause of the difference in catalytic activity with respect to dehydrative epoxidation. In addition, the stereochemistry involved in dehydrative epoxidation was explored. DFT calculations were carried out to determine the energetics of the reaction, including the transition states as well as the configurations and adsorption of the molecules. On the basis of the experimental results and the DFT calculations, the active site of the catalyst and a reaction mechanism for dehydrative epoxidation is proposed. Using the dehydrative epoxidation, heterogeneous catalytic processes for the production of 1,3-butadiene from **BD** is proposed. The process is composed of sequential three reactions: dehydrative epoxidation of **BD** to **EB**, isomerization of **EB** to 3-buten-2-ol (**BO**), and acid-catalyzed dehydration of **BO** to 1,3-butadiene.

2.2 Experimental

2.2.1 Preparation catalysts

Sodium acetate trihydrate (TCI), potassium oxalate monohydrate (Samchun Chemical), cesium acetate (Samchun Chemical), magnesium nitrate hexahydrate (Fluka), calcium nitrate tetrahydrate (Sigma-Aldrich), strontium nitrate (Sigma-Aldrich), lanthanum nitrate hexahydrate (Junsei Chemical), and cerium nitrate hexahydrate (Kanto chemical) were used as precursors for supported basic metal oxide catalysts and were used without further purification. Al-MCM-41 (Aluminosillicate, mesostructured, Sigma-Aldrich) was used as received. The catalysts were prepared by the incipient wetness impregnation method. In typical procedures, at first, a predetermined amounts of precursor was dissolved in 3 ml of deionized water. The aqueous solution of precursor was then added drop-wise to 2.0 g of a support oxide (SiO_2 (Aerosil® 200), Al_2O_3 (Aeroxide® Alu C), and TiO_2 (Aeroxide® P25)) with vigorous mixing by hand for at least 20 min. To prevent a complete wetness, impregnation was conducted repeatedly by dosing a small quantity of precursor solution and followed by drying at room temperature. The impregnated powders were dried at 343 K overnight, and then be grounded and calcined at desired temperature (5 K/min) for 4h.

For the catalysts used in the screening of active materials (section 2.3.2), 10 wt.% (Cs_2O, CaO, SrO, La_2O_3, CeO_2), 2.4 wt.% (Na_2O), 3.6 wt.% (K_2O), and 3.1 wt.% (MgO) were loaded on a SiO_2 support, and the notation of M/SiO_2 is used. Calcination was carried out at 823 K for 4h. In sections 3.3 and 3.4, the

following notation is used to express the SiO_2 supported Cs catalysts: $xCsO_x/SiO_2$-y, where x is the wt.% of Cs_2O loading, and y is the calcination temperature (723 – 1023 K). The catalysts prepared using other supports are expressed in the same way.

Basic lithium phosphate (Li_3PO_4) was prepared by precipitation method. 1.82 g of sodium phosphate monobasic (0.015 mol, NaH_2PO_4, Sigma-Aldrich) and 1.28 g of lithium hydroxide monohydrate (0.030 mol, $LiOH{\cdot}H_2O$, Sigma-Aldrich) were separately dissolved in 15 ml and 10 ml of deionized water, respectively. Prior to precipitation, the former solution (NaH_2PO_4) was transferred to a 100 ml round-bottom flask. The contents were heated and the temperature was maintained at 313 K. The aqueous solution of $LiOH{\cdot}H_2O$ was then added drop-wise with vigorous stirring using a magnetic bar. A white precipitate was immediately formed when the solution was added. The mixed solution was aged at 313 K for 24 h. After the aging, the white precipitates were isolated on a filter, washed three times with 200 ml of de-ionized water, and dried at 343 K for overnight. Calcination of the dried precipitates were conducted at 673 K (5 K/min of ramping speed) for 6 h.

2.2.2 Reactivity tests

A fixed-bed quartz reactor was used to evaluate the catalytic performances of the catalysts for the dehydration of 2,3-butanediol, 1,2-propanediol, and ethylene glycol. Temperature were measured by a K-type thermocouple and were controlled with external electrical furnace. Reactions were performed

using 0.1 g of catalyst samples held on a porous quartz bed with aqueous solutions of 2,3-butanediol (Acros Organics, 98%, mixture of *racemic* and *meso* forms), *meso*-2,3-butanediol (Sigma-Aldrich), 1,2-propanediol, ethylene glycol (Alfa Aesar, 97%), *trans*-2,3-epoxybutane (Alfa Aesar, 97%), *cis*-2,3-epoxybutane (Alfa Aesar, 98%), 3-buten-2-ol (Alfa Aesar, 97%), and methyl ethyl ketone (J.T. Baker, 99.0%). The compositions of reactants in the aqueous solutions were 9.9 wt.% (2.1 mol%) for 2,3-butanediol, 8.3 wt.% (2.1 mol%) for 1,2-propanediol, 6.9 wt.% (2.1 mol%) for ethylene glycol, and 8.1 wt% (2.1 mol%) for the others in order to ensure a same space velocity of reactants (Space velocity (SV) = total flow rate / amounts of catalyst = 1.38 L/(min (g cat)). The reactor was heated to the desired temperatures (673 K) with ramping rate of 10 K/min and maintained for 30 min with a flow of dry N_2 (99.999%, 30 cm^3/min). The reactant solutions were then injected with a rate of 1.5 cm^3/h (1.64 mmol 2,3-butanediol/h) into a pre-heating zone which was maintained at 473 K and was connected to a top of the reactor. Effluent gases were passed through a helix type condenser and was collected in a sample tube containing 20 ml of deionized water. Acetonitrile was used as an external standard for quantification and added to products collected hourly. The products were analyzed using gas chromatography (Younglin ACME 6100 instrument) equipped with a FID detector and Rtx®-VRX capillary column (Restek, cat. # 19316). The data acquired at 2 h of the reaction was used to compare the catalytic activity of the catalysts. In case of the acid catalyzed dehydration of the intermediates, 1,3-butadiene in the effluent gases was analyzed using an on-line gas chromatograph (Donam DS 6200)

equipped with a FID detector and HayeSep C-ValcoPLOT® capilary column (VICI®, Product no. CFS-PC3053-200). The turnover frequency (TOF) and specific formation rates of products for supported catalysts were calculated by following equations:

$$\text{Turnover frequency } (\mathrm{h}^{-1}) = \frac{Converted \quad amounts \quad of \quad reactant \quad (mol/h)}{Loaded \quad amounts \quad of \quad metal \quad (mol)}$$

$$\text{Specific formation rate } (\mathrm{h}^{-1}) = \frac{Formed \quad amounts \quad of \quad product \quad (mol/h)}{Loaded \quad amounts \quad of \quad metal \quad (mol)}$$

2.2.3 Characterization

Temperature programmed desorption (TPD) of NH_3 was carried out using Micromeritics Autochem II chemisorption analyzer. Prior to the analysis, 0.1 g of sample was heated at 673 K for 1h under a He flow to remove adsorbed impurities. After cooling to 323 K, the sample was saturated with probe by a flow of 10.2% NH_3/He. The physisorbed probe was removed by flushing of He flow at 373 K. After the sample was cooled down to 323 K and the TCD signal was stabilized, the signal was recored with increasing the temperature from 323 K to 673 K at a rate of 10 K/min under a flow of He.

The Hammett indicator titration method was utilized to compare the base strength of the prepared catalysts. In typical procedure, the Hammett indicators were dissolved in methanol to obtain 0.05 M solutions. Prior to the titration, a determined amounts (10 mg) of a catalyst was heated at 423 K in vacuum oven to remove adsorbed species. Then, it was titrated by 400 μl of each indicator solution, and color change was recorded. Following four indicators were used:

Neutral red (pK_a = 6.8), phenolphthalein (pK_a = 8.2), 2,4-dinitroaniline (pK_a = 15.0), and 4-nitroaniline (pK_a=18.4). Benzoic acid titration method was employed to quantify the total basicity of the catalysts.

X-ray photoelectron spectroscopy (XPS) was carried out on a KRATOS AXIS electron spectrometer equipped with MgKα radiation. The binding energies were corrected using C_{1s} as an internal standard (284.6 eV). The peaks were fitted by mixed Gaussian-Lorentzian functions with substraction of Shirley type background using XPS peak fitting program (XPSPEAK 4.1).

^{29}Si cross polarization/magic angle spinning (CP/MAS) nuclear magnetic resonance (NMR) spectra of the samples were recorded on a Bruker AVANCE 400 WB (400 MHz) spectrometer operating at a frequency of 79.5 MHz. The magic angle spin speed used for ^{29}Si spectral recording was 5 kHz. ^{133}Cs MAS NMR spectra were recorded on the same instrument operating at a frequency of 52.5 MHz and 7 kHz of the magic angle spin speed. Electron spin resonance (ESR) spectra of the catalysts were recorded on a JEOL JES-TE200 spectrometer operating at 9.43 GHz of a microwave frequency and 1.0 mW of a microwave power. The differential scanning calorimetry (DSC) and thermogravimetric analysis (TGA) were performed on a TA instruments SDT Q600 analyzer. The temperature was increased from room temperature to 1173 K with a heating rate of 10 K/min under an air flow.

High resolution transmission electron micrograph (HR-TEM) images were obtained on a JEOL JEM-3010 microscope using bright field (BF) mode with an acceleration voltage of 300 kV. The X-ray diffraction (XRD) patterns were measured by a Rigaku D-MAX2500-PC powder X-ray diffractometer with Cu

Kα radiation (1.5406 Å) in an operating mode of 50 kV and 100 mA. An analytical high-angle annular dark-field scanning transmission electron microscope (HAADF-STEM, Tecnai F20-FEI, 200 kV) equipped with energy dispersive X-ray spectroscopy (EDS, Tecnai 136−5-EDAX) was used to explore the distribution of elements over the prepared catalysts. N_2 adsorption-desorption analyses were carried out using a Micromeritics ASAP-2010 instrument. The total surface area of the samples was calculated by the BET method (P/P_o = 0.1-0.2). The pore volume and pore size distributions were obtained from the desorption branches of the isotherms using BJH methods.

2.2.4 Computational details

Periodic density functional theory (DFT) calculations were carried out using the Vienna *ab initio* simulation package (VASP) [55]. The generalized gradient approximation (GGA) parameterized by Perdew-Burke-Ernzerhof (PBE) exchange-correlation functional was employed [56]. Ionic cores were described by the projector augmented wave (PAW) method [57]. Dispersion forces were included with the DFT-D2 Grimme's empirical correction [58]. The C6 (57.74 J nm^6/mol) and R0 (1.776 Å) parameters for cesium were taken from the data of F. Zhang et al [59]. The wave functions were constructed from the expansion of planewaves with an energy cutoff of 400 eV. A 1 × 1 × 1 Monkhorst-Pack *k*-point mesh was used to sample the Brillioun zone. All calculations were converged until the forces on all atoms were less than 0.03 eV/Å. The electronic optimization steps were converged self-consistently to < 2 × 10-4 eV.

In our calculations, β-cristobalite (001) was used to represent the surface of the amorphous SiO_2. It has been often used for the same purpose because the physical properties, including refractive index and bulk density, of β-cristobalite are close to those of amorphous SiO_2 [60,61]. Previous reports also have supported that (001) and (111) plane of β-cristobalite successfully describe the surface of amorphous SiO_2 [60-63]. Detailed explanation about the model can be found in the report of J. Handzlik et al.[64] I42d space group with Si in 4 (a) and O in 8 (d) crystallographic positions [65] was used as an initial structure for geometry optimization of bulk β-cristobalite. For the calculation of bulk optimization, the cutoff energy was increased to 520 eV and a 4 × 4 × 4 *k*-point mesh was used. The lattice constants of the fully optimized bulk structure are found to be 5.02 Å (a, b) and 7.38 Å (c), which is in agreement with the experimentally reported values of 5.04 Å (a, b) and 7.13 Å (c) [65]. The surface was constructed by cleaving (2 × 2 × 1) optimized bulk structure (a = b = 10.04 Å) along the (001) plane. To prevent in-physical electronic interactions, 20 Å of vacuum region between the slabs was added. Dangling oxygens on the surface were fully hydroxylated by adding equal number of hydrogens. The surface consisted of 8 layers (4 Si layers and 4 O layers). The top four layers were allowed to relax while the remaining four bottom layers were fixed. The surface of CsO_x/SiO_2 was constructed by replacing one of the hydrogen atoms with Cs atom since Cs ion in CsO_x/SiO_2 has same oxidation state (+1) as proton, and is capable to exchange with the proton [66-69]. Experimental evidences are also provided by XPS analysis of CsO_x/SiO_2 catalyst. The most stable geometries for the adsorption of *anti-meso*-2,3-

butanediol, *gauche-meso*-2,3-butanediol, *cis*-2,3-epoxybutane and *trans*-2,3-epoxybutane were obtained by systematically exploring the adsorption sites on the CsO_x/SiO_2 surface. The adsorption energies were calculated as follows: $\Delta E_{ads} = E_{adsorbate/surface} - E_{adsorbate} - E_{surface}$.

The transition state was located using climbing image-nudged elastic band (CI-NEB) method [70,71]. Seven equally spaced images were obtained by linear interpolation and used as initial trajectories for reaction path. In the CI-NEB calculations, the images was refined until the maximum atomic forces are converged within 0.06 eV/Å.

2.3 Results and discussion

2.3.1 The dehydrative epoxidation of vicinal diols

Acidic catalysts are frequently used as dehydration catalysts and were mainly adopted to use in the dehydration of vicinal diols. The dehydration of vicinal diols in the presence of an acidic catalyst preferentially produces aldehydes and ketones via a carbocation intermediate which is frequently observed in acid catalysis [48-54]. On the other hand, S. Sato et al. utilized the rare-earth and transition-metal oxides for the dehydration of vicinal diols including 1,2-propanediol, 2,3-butanediol (**BD**), and 1,2-butanediol [47,72]. In the reports, main products of reaction over the rare-earth metal oxides were aldehydes and ketones as similar to the acid catalyzed dehydration. When transition metal oxides were utilized, they found that ZrO_2 catalyst is capable of selectively producing 3-buten-2-ol (**BO**) via dehydration of **BD** [47].

In contrast to the above dehydration reactions, the reaction of vicinal diols over a basic CsO_x/SiO_2 catalyst resulted in the formation of new dehydration products (Table 2-1). Epoxides including epoxyethane, 1,2-epoxypropane, and 2,3-epoxybutane (**EB**) were produced from ethylene glycol, 1,2-propanediol, and **BO**, respectively. The reaction of 1,2-propanediol and **BD** also produced unsaturated alcohols (2-propen-1-ol and **BO**, respectively), whereas unsaturated alcohols were not produced in the case of the reaction of ethylene glycol due to the shorter carbon chain. Comparing the reaction results of the vicinal diols (Figure 2-1), the extent of conversion became higher with the length of the carbon chain of the reactant. This is attributed to increased

amounts of epoxides and unsaturated alcohols that are produced. Aldehydes and ketones presented opposite trend and their yields decreased slightly with the longer carbon chain length. Consequently, dehydrative epoxidation takes place more easily for vicinal diols with longer carbon chain.

Considering the fact that typical dehydration leads to the formation of C=C or C=O bonds, the formation of epoxides is clearly a distinguishing result, since a strained intramolecular C-O bond was formed. Sequence of this reaction may be similar to the dehydration of monoethanolamine to ethyleneimine which involves a formation of similar 3-membered ring via dehydration [73]. However, it is important to note that the dehydration of monoethanolamine to ethyleneimine can be induced by SiO_2 catalyst, whereas the formation of epoxides from vicinal diols cannot be. There is definitely distinct catalysis on the formation of epoxides from vicinal diols. Discovering a catalysis that is used in the formation of epoxides from the dehydration of the vicinal diols could be an important issue.

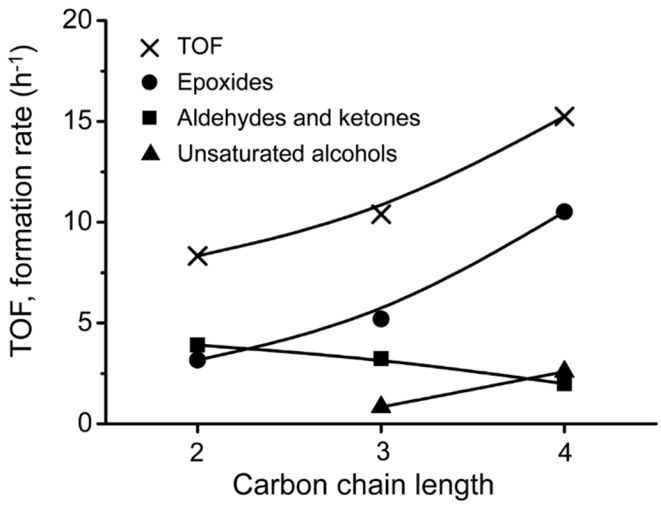

Figure 2-1. Compositional changes in dehydration products with respect to the carbon chain length of the vicinal diols: Carbon chain length of 2, 3, and 4 represents ethylene glycol, 1,2-propanediol, and 2,3-butanediol **BD**, respectively. Reaction condition: Fixed-bed flow reactor, T_{rxn} = 673 K, SV = 1.38 L/(min (g cat)).

Table 2-1 Catalytic reaction of vicinal diols over the CsO_x/SiO_2.[a]

Reactant	Turnover frequency (h^{-1})[b]	Products / Specific formation rate (h^{-1})[c]			
		Epoxide	Unsaturated alcohol	Ketone	Aldehyde
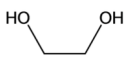 ethylene glycol	8.3 (36)	 epoxyethane	-	-	 acetaldehyde
		4.4 (38)	-	-	3.9 (47)
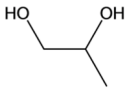 1,2-propanediol	10.4 (45)	 epoxypropane	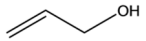 2-propen-1-ol	 acetone	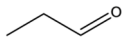 propionaldehyde
		5.2 (50)	0.8 (8)	0.9 (9)	2.3 (22)
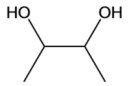 2,3-butanediol (**BD**)	15.3 (66)	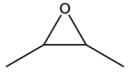 2,3-epoxybutane (**EB**)	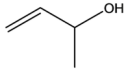 3-buten-2-ol (**BO**)	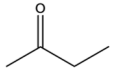 methyl ethyl ketone (**MEK**)	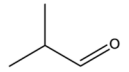 Isobutyraldehyde (**IBA**)
		10.5 (69)	2.6 (17)	1.7 (11)	0.3 (2)

[a] Fixed-bed flow reactor, T_{rxn} = 673 K, SV = 1.38 L/(min (g cat)). [b] he values in parentheses are the conversion of reactant (%). [c] he values in parentheses indicate product selectivity (%).

2.3.2 Dehydrative epoxidation of 2,3-butanediol: Screening of basic metal oxides

To explore the dehydrative epoxidation reaction in more detail, a series of active materials for the reaction is tested. A number of SiO_2 supported catalysts were prepared using alkali, alkaline-earth, and rare-earth metal oxides as basic metal oxides. Acidic Al-MCM-41 was also tested as a reference catalyst. In these experiments, **BD** was used as representative vicinal diol. Since it was confirmed that **BO** is secondary product which is originated from **EB**, the specific activity for the dehydrative epoxidation was compared based on the sum of specific formation rate for **EB** and **BO**. Chemical names, structures, and abbreviations for reactants and products appeared in the conversion of **BD** are summarized in Scheme 2-1.

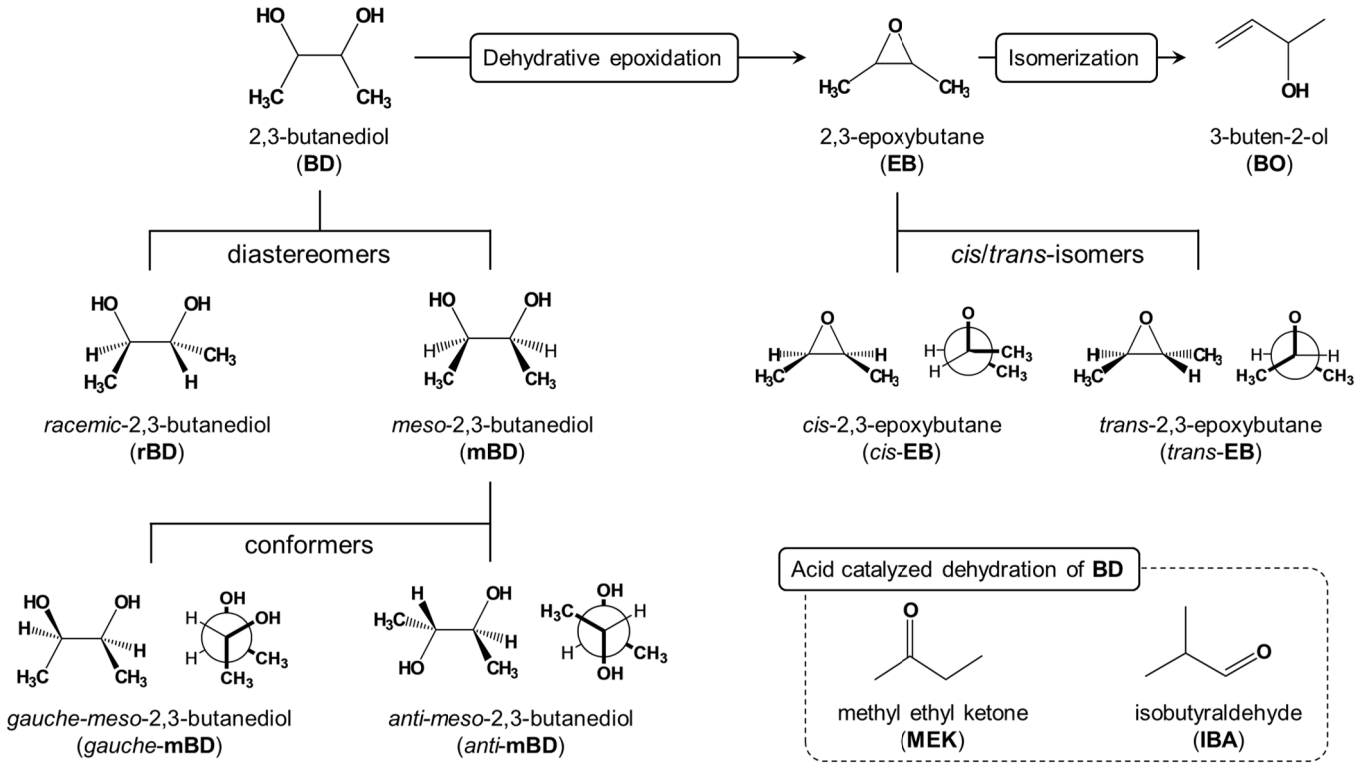

Scheme 2-1. Chemicals included in this study on the dehydration of 2,3-butanediol (**BD**). Names, abbreviations (in parentheses), and structures of reactants and possible products are present.

2.3.2.1 Reactivity tests

In the results for the SiO_2 supported alkali metal oxides (Table 2-2. entry 1-3), KO_x/SiO_2 showed selective formation of **EB** and **BO**, but with considerably lower activity than CsO_x/SiO_2. Specific formation rate of **EB** and **BO** for NaO_x/SiO_2 was 4-fold lower than KO_x/SiO_2. Accordingly, the specific activity for dehydrative epoxidation increased in the order of increasing atomic number of the alkali metal oxides. Meanwhile, the SiO_2 supported alkaline-earth and rare-earth metal oxides (entry 4-8) produced **MEK** and **IBA** mainly. Any trace amounts of **EB** and **BO** were not detected for MgO_x/SiO_2, LaO_x/SiO_2, CeO_x/SiO_2. Only CaO_x/SiO_2 and SrO_x/SiO_2 were capable of producing **EB** and **BO**, but their specific activities were lower than those of the supported alkali metal oxides. Therefore, alkaline-earth and rare-earth metal oxides were considered poorly effective for the dehydrative epoxidation than alkali metal oxides. In the reaction for Al-MCM-41 catalyst (acidic catalyst, entry 9), **MEK** and **IBA** were exclusively produced, as previously reported [53].

Table 2-2 Catalytic performance of the catalysts on the dehydration of 2,3-butanediol.[a]

Entry	Catalysts[b]	Turnover frequency (h^{-1})[c]	Specific formation rate (h^{-1})[d]				Specific activity (h^{-1})[e]
			2,3-epoxybutane (**EB**)	3-buten-2-ol (**BO**)	Methyl ethyl ketone (**MEK**)	Isobutyraldehyde (**IBA**)	
1	NaO_x/SiO_2	4.0 (19)	0.4 (10)	0.2 (5)	2.2 (54)	0.4 (9)	0.6 (2.9)
2	KO_x/SiO_2	4.5 (21)	1.6 (36)	0.5 (12)	1.3 (29)	0.4 (8)	2.1 (10.1)
3	CsO_x/SiO_2	15.3 (66)	10.5 (69)	2.6 (17)	1.7 (11)	0.3 (2)	13.1 (56.8)
4	MgO_x/SiO_2	21.5 (100)	0	0	14.2 (66)	3.9 (18)	0
5	CaO_x/SiO_2	8.2 (89)	0.2 (2)	0.4 (5)	5.0 (62)	1.2 (14)	0.6 (6.2)
6	SrO_x/SiO_2	9.7 (57)	0.3 (3)	0.5 (5)	6.6 (68)	1.0 (10)	0.8 (4.6)
7	LaO_x/SiO_2	26.7 (100)	0	0	19.5 (73)	4.0 (15)	0
8	CeO_x/SiO_2	28.2 (100)	0	0	20.9 (74)	4.2 (15)	0
9	Al-MCM-41[f]	79.7 (100)	0	0	46.2 (58)	23.1 (29)	0

[a] Fixed-bed flow reactor, T_{rxn} = 673 K, SV = 1.38 L/(min (g cat)). [b] Loaded basic metal oxides are denoted by a symbol. [c] The values in parentheses are the conversion of 2,3-butanediol (%). [d] The values in parentheses indicate product selectivity (%). [e] Sum of specific formation rate for 2,3-epoxybutane (**EB**) and 3-buten-2-ol (**BO**). The values in parentheses are the yield of **EB** and **BO**. [f] T_{rxn}=573 K.

2.3.2.2 Acid and basic properties of the screened catalysts

It appeared that dehydrative epoxidation is significantly influenced by the type of loaded basic metal oxides. In order to identify the causes of the catalytic difference among the screened catalysts, the acidic and basic properties of the catalysts were correlated with the reaction results.

Figure 2-2 show the NH_3 TPD results for the catalysts. The loading of basic metal oxides on the SiO_2 support resulted in an increase in acidic sites. This increase would be similar to the formation of acidic sites on heteroatom doped silicate materials [74]. The amounts of acidic sites that are formed vary considerably, depending on the type of loaded metal oxides. MgO_x/SiO_2, CaO_x/SiO_2, and LaO_x/SiO_2 have relatively high amounts of acidic sites, and the SiO_2 supported alkali metal oxides and strontium oxide have medium amounts of acidity. CeO_x/SiO_2 contained a quite low level of acidic sites. The formation of additional acidic sites could cause the considerable formation of **MEK** and **IBA** for the SiO_2 supported alkaline-earth metal oxides and rare-earth metal oxides, as **MEK** and **IBA** are major products of acid catalyzed dehydration. Since Brønsted acidic catalysts were reported to be effective in the formation of **MEK** and **IBA** [53,54], the type of acidic sites formed in these catalysts is predicted to be Brønsted acidic sites. Compared to Al-MCM-41, these SiO_2 supported catalysts produced much smaller amounts of **IBA**. The ratio of **MEK** to **IBA** for Al-MCM-41 was found to be about 2 whereas that for the alkaline-earth and rare-earth metal oxides was considerably higher (ranging from 3.7 to 6.8). The smaller amounts of **IBA** for the SiO_2 supported alkaline-earth and

rare-earth metal oxides implies that acidic sites weaker than those in Al-MCM-41 were formed in these catalysts, because **IBA** is formed via a methyl group rearrangement,[53] which is closely related to the formation of a carbocation [75]. In contrast, much less **MEK** and **IBA** were formed on the SiO_2 supported alkali metal oxides, which indicates that the formed acidic sites by the loading of alkali metal oxides are different from those for alkaline-earth and rare-earth metal oxides, and are probably weak Lewis acidic sites.

The trend for the specific formation rate of **EB** and **BO** among the SiO_2 supported catalysts is also important to note in relation to the base strength of the catalysts. The base strength of alkali, alkaline-earth, and rare-earth metal oxides generally follows the theoretical basicity trend of electronegativity (EN). This relationship of base strength and EN has been frequently reported in metal oxides and hydroxides [76-79], ion-exchanged zeolites [80-84], and supported metal oxides [85,86]. The EN values in the Pauling scale for loaded metals are in decreasing order from Mg (1.31), Ce (1.12), La (1.1), Ca (1.0), Sr (0.95), Na (0.93), K (0.82), to Cs (0.79), which is the opposite trend of base strength. When the specific formation rate of **EB** and **BO** for the SiO_2 supported catalyst is compared with EN values of loaded metal (Figure 2-3), the specific activity tended to increase with decreasing order of EN. Therefore, this relationship indicates that stronger basic sites are more advantageous for dehydrative epoxidation. The specific activity of NaO_x/SiO_2 deviated slightly from the trend because of the significantly decreased surface area of the catalyst (13, 101, 115 m^2/g for NaO_x/SiO_2, KO_x/SiO_2, CsO_x/SiO_2, respectively). A Hammett indicator titration method was utilized to confirm the base strength and total basicity of

the SiO_2 supported catalysts. The results of the Hammett indicator titration method are consistent with the base strength scale by EN of the loaded metal as the catalysts which consisted of a metal oxide with a high EN value showed a lower base strength (MgO_x/SiO_2, LaO_x/SiO_2, and CeO_x/SiO_2). However, the poor resolution of the method due to limitations in the availability of indicators made it difficult to distinguish the base strength of the catalysts within $8.2 < H_- < 15.0$. Comparing the base strength determined by Hammett indicator titrations and activity for the dehydrative epoxidation, the catalysts with strong basic sites of $H_- > 8.2$ were clearly able to trigger the dehydrative epoxidation reaction.

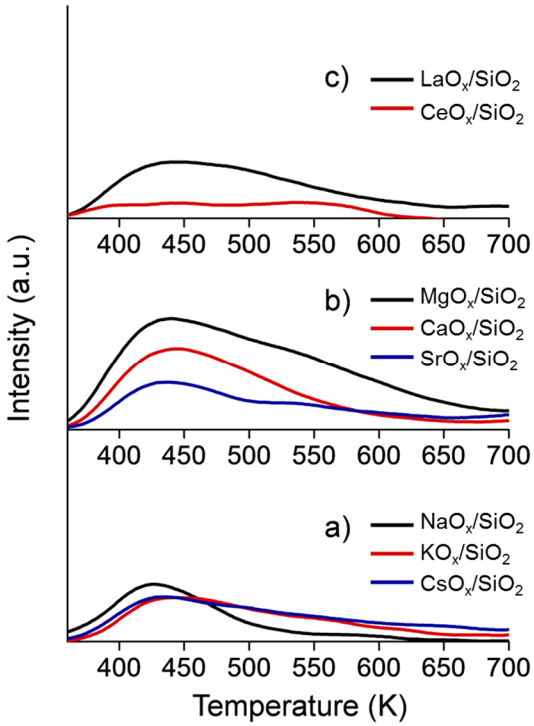

Figure 2-2. NH_3-TPD profiles of the SiO_2 supported basic metal oxide catalysts: a) alkali metal oxides, b) alkaline-earth metal oxides, and c) rare-earth metal oxides.

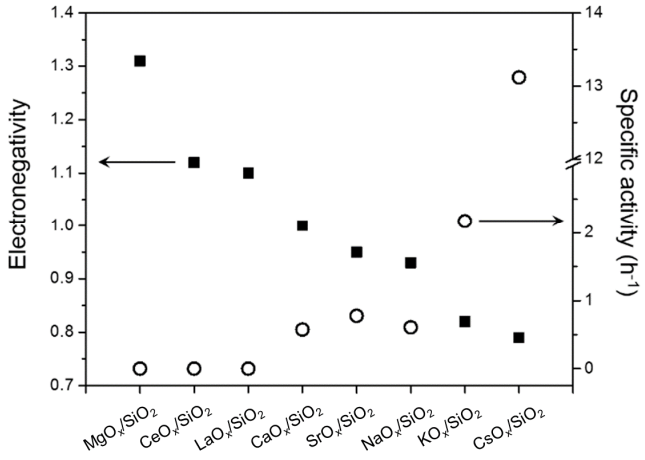

Figure 2-3. Relationship between electronegativity (closed rectangle, left y axis) and the specific activity (open circle, right y axis) for the SiO_2 supported catalysts.

2.3.2.3 Structural characterization of the SiO_2 supported alkali metal oxide catalysts

Among the alkali metal oxides, CsO_x/SiO_2 was found to be exceptionally active for dehydrative epoxidation. This can be attributed, in part, to the stronger basicity of Cs than Na and K. However, difference in base strength does not appear to be sufficient to explain the exceptional performance of CsO_x/SiO_2. To identify other causes for this exceptional performance, the structural characteristics of the supported alkali metal oxides (NaO_x/SiO_2, KO_x/SiO_2, and CsO_x/SiO_2) are compared as well.

The chemical states of alkali metal atoms in the catalysts were analyzed by XPS and ESR (Figure 2-4 and 2-5, respectively). The results indicate that alkali metal atoms on the catalysts are present as metal cations (M^+), and did not exhibit any paramagnetic or diamagnetic properties, indicating the absence of superoxide (O_2^-) and peroxide (O_2^{2-}) species.

HR-TEM and STEM images of the SiO_2 supported alkali metal oxide catalysts are shown in Figure 2-6. The images show the absence of crystalline alkali metal oxide phases and also show that the catalysts are microscopically homogeneous. No evidence was found to the formation of separated particulates or a crystalline phase. The absence of a crystalline phase was also supported by the results of XRD analysis. EDS mapping of the CsO_x/SiO_2 catalyst clearly shows that the Cs atoms are well dispersed within the catalyst. The morphology of the SiO_2 supported catalysts is similar to each other and is nearly identical to bare SiO_2.

In contrast, the results of N_2 adsorption-desorption analyses revealed that the pore structure and specific surface area of the catalysts are considerably different from one another. The BET surface area of the catalysts was 115, 101, and 13 m^2/g for CsO_x/SiO_2, KO_x/SiO_2, and NaO_x/SiO_2, respectively. In the isotherm plots (Figure 2-7), a Type IV isotherm and a H3 hysteresis loop at P/P_0 = 0.8 – 1.0 indicates that inter-particular porosity is common for these catalysts. The inter-particular porosity decreased in the order of Cs < K < Na. This indicates that SiO_2 particles were agglomerated by the loading of alkali metal oxides, the extent of which is in the order of Cs < K < Na. Moreover, the significant decrease in the surface area of NaO_x/SiO_2 can be attributed to the transformation of amorphous SiO_2 to cristobalite by high temperature calcination as a frequently observed in Na-SiO_2 system [87].

Local structures of the SiO_2 supported alkali metal oxide catalysts were explored by means of ^{29}Si CP/MAS NMR (Figure 2-8). In the results, the bare support (SiO_2) shows a characteristic peak at -108 ppm which is assigned to Q^4 species of Si [88]. The slightly asymmetric shape (to positive chemical shift) of the peak indicates that Q^3 species also exist in the support material. When sodium or potassium oxide was loaded on the support, the Q^3 peak (-95 ppm) clearly increased. This change in the spectrum suggests that the highly cross-linked silica network is disrupted by sodium and potassium, resulting in the formation of branching sites. In contrast, the shape of the NMR spectrum for CsO_x/SiO_2 was nearly identical to that of the bare support. The different extent of change in the local silicate structure can be attributed to the strength of silicate dissolving ability of alkali metal cations which is in the order of Cs^+ <

$Na^+ < K^+$ [89]. Considering this trend of dissolving ability, the ionic radii of K^+ (152 pm) which is smaller than Cs^+ (182 pm), and the coarse framework of amorphous silica, K^+ can more easily penetrate into the bulk layer of the support than Cs^+ (Na^+ is not compared since NaO_x/SiO_2 has a considerably lower specific surface area). Experimental evidence for the degree of penetration from XPS spectra of the O 1s orbital of KO_x/SiO_2 and CsO_x/SiO_2 is found as follows: When alkali metal oxides were loaded on the support, a new peak at near 530.5 eV (O_{Alk}) was appeared in O_{1s} spectra due to the interaction of alkali metal cations with nearby oxygen atoms. When the O_{Alk} and alkali metal cations are quantified, the atomic ratio of O_{Alk} and alkali metal cations for KO_x/SiO_2 was determined to be 6.6, which is higher than that for CsO_x/SiO_2 (3.2). This result indicates that K^+ is surrounded by a larger number of oxygen atoms than Cs^+, which means that more K^+ is located in the bulk layer of the SiO_2 support. The penetrated K^+ (and generated basic sites) in KO_x/SiO_2 would be not accessible for the reaction. Consequently, this structural difference between KO_x/SiO_2 and CsO_x/SiO_2 could contribute to the outstanding performance of CsO_x/SiO_2.

Based on these results, it can be concluded that outstanding performance of CsO_x/SiO_2 among the SiO_2 supported alkali metal oxide catalysts can be attributed to i) stronger basic sites induced by the loading of Cs^+, ii) lower agglomeration of SiO_2 particles and less decrease in specific surface area, and iii) sufficiently large ionic radius and lower extent of silicate dissolution that allows Cs^+ to exist on the surface of the catalyst.

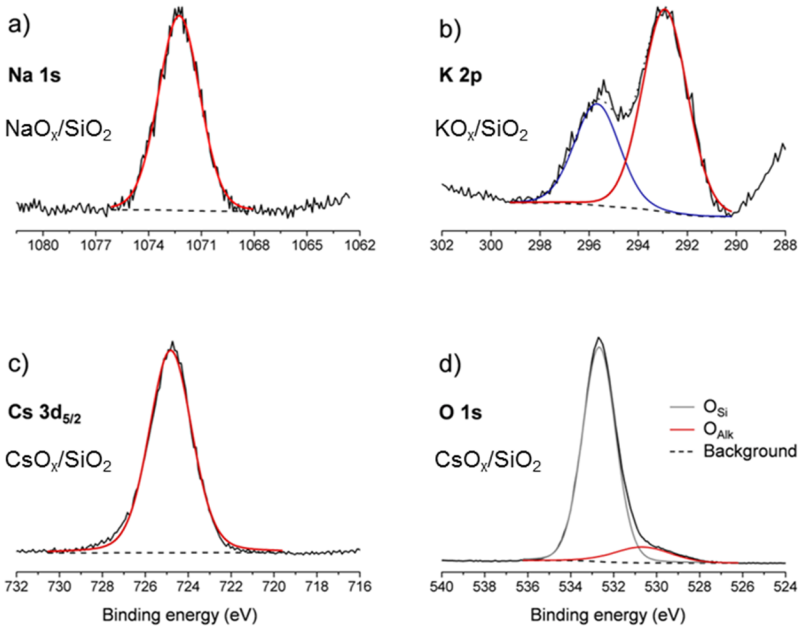

Figure 2-4. XPS spectra of the supported alkali metal oxides: a) Na 1s of NaO_x/SiO_2, b) K 2p of KO_x/SiO_2, c) Cs $3d_{5/2}$ of CsO_x/SiO_2, and d) O 1s of CsO_x/SiO_2.

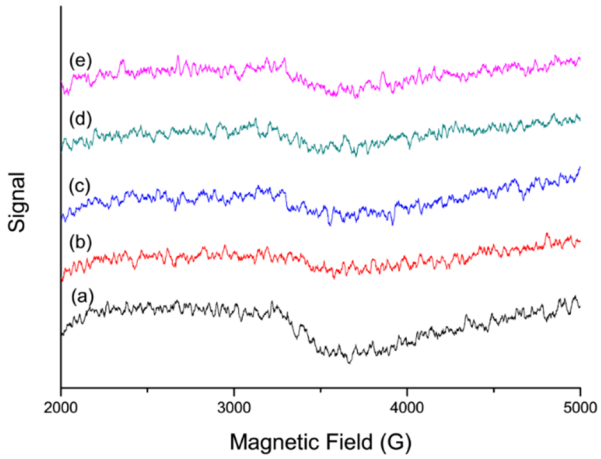

Figure 2-5. ESR spectra of a) NaO_x/SiO_2, b) KO_x/SiO_2, c) CsO_x/SiO_2, d) $10CsO_x/Al_2O_3$-823, and e) $10CsO_x/TiO_2$-823.

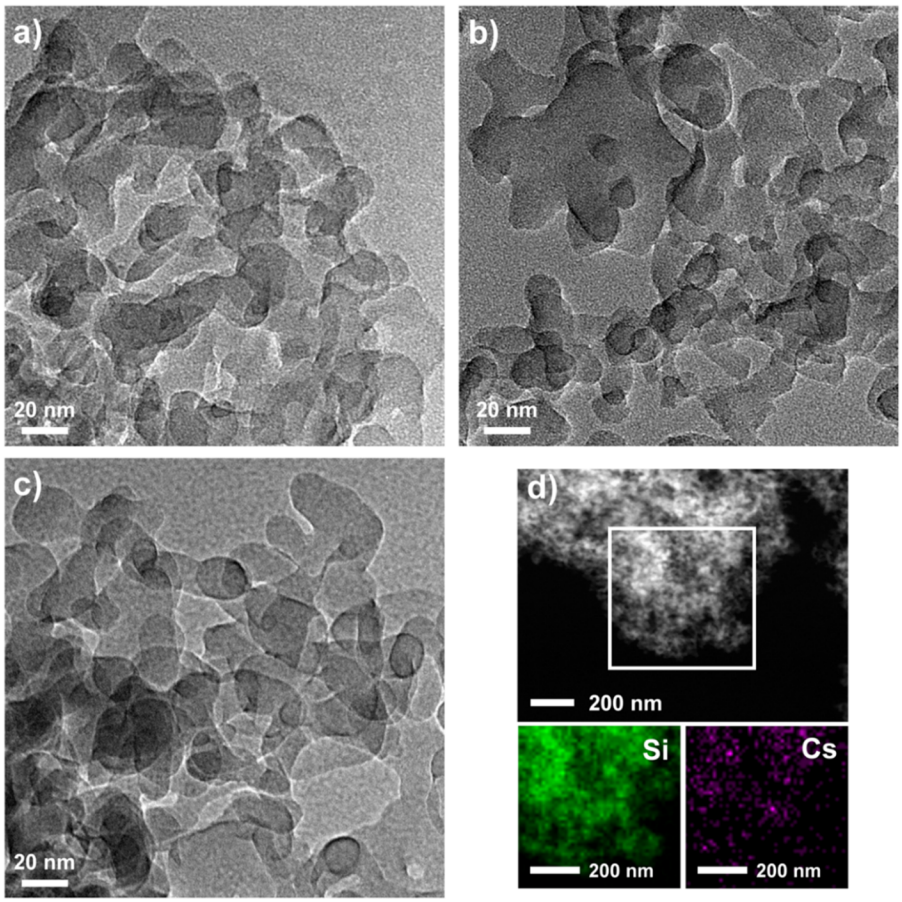

Figure 2-6. HR-TEM images of a) NaO_x/SiO_2, b) KO_x/SiO_2, c) CsO_x/SiO_2, and d) HAADF-STEM image of CsO_x/SiO_2 and their corresponding elemental mapping images of Cs (purple), Si (green).

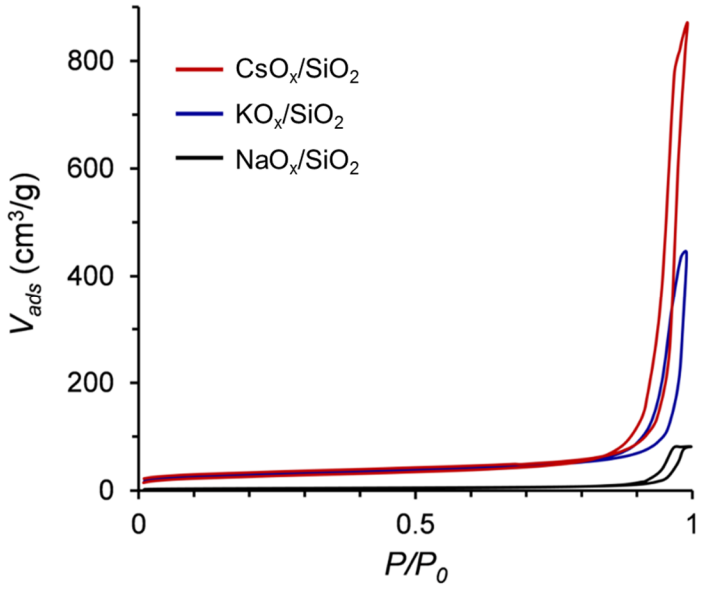

Figure 2-7. Isotherm plots of N_2 adsorption-desorption analyses for the SiO_2 supported alkali metal oxide catalysts.

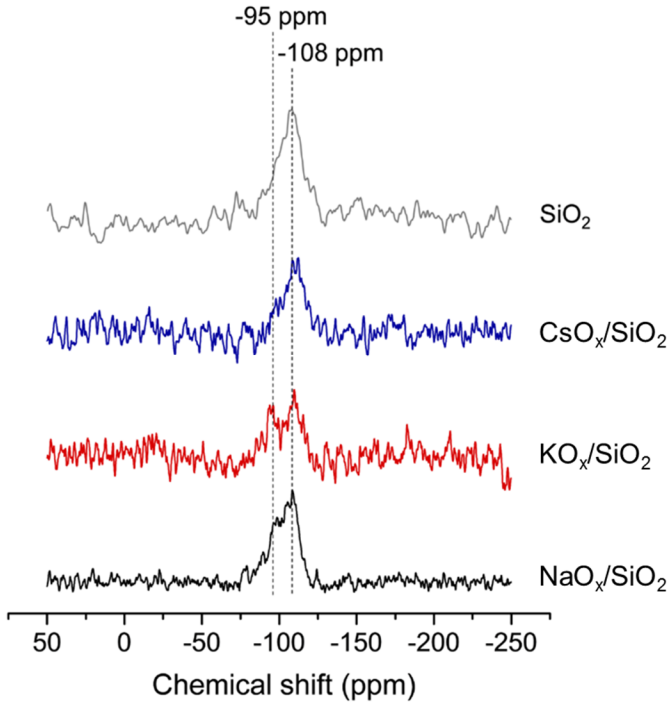

Figure 2-8. ^{29}Si CP/MAS NMR spectra of the SiO_2 supported alkali metal oxide catalysts.

2.3.3 Effect of preparation conditions in CsO_x/SiO_2 catalyst system

To further understand the CsO_x/SiO_2 catalyst system in more detail, I studied the effect of preparation conditions including Cs_2O wt.% loading and calcination temperature on the catalytic performance and the structure of the catalysts (the notation of $xCsO_x/SiO_2$-y is used to express the x wt.% loading of Cs_2O and y K of calcination temperature). Furthermore, a stability test was performed for the optimum catalyst.

2.3.3.1 Cs_2O wt.% loading

Figure 2-9a show the isotherm plots of N_2 adsorption-desorption analyses for the CsO_x/SiO_2 catalysts with different amounts of loaded Cs_2O. With increasing Cs_2O wt.% loading, the specific BET surface area is continuously decreased from 177 m^2/g ($1CsO_x/SiO_2$-823) to 147 ($5CsO_x/SiO_2$-823), 115 ($10CsO_x/SiO_2$-823), and 49 m^2/g ($20CsO_x/SiO_2$-823). Some extent of this decrease in surface area can be attributed to increased amounts of Cs_2O. However, the effective SiO_2 surface area is also decreased (179, 155, 127, and 61 m^2/g for 1, 5, 10, and $20CsO_x/SiO_2$-823, respectively), which indicates that an increase in Cs_2O content significantly influences the structure of the SiO_2 support. In Figure 2-9a, the hysteresis at P/P_0 = 0.7~1.0 shifted to a higher P/P_0 value and is considerably decreased with increasing Cs_2O contents from 10 wt.% to 20 wt.%. This shift means that inter-particular porosity disappears due to agglomeration of SiO_2 particles. In the results of XRD analysis (Figure 2-10), the peak

assigned to amorphous SiO_2 (22°) is shifted to higher angle (24.5° for $20CsO_x/SiO_2$-823), indicating that large Cs atoms are intercalated between SiO_2 particles during the agglomeration process.

The effect of Cs_2O wt.% loading on catalytic activity are shown in Figure 2-11 as a function of the surface density of Cs atoms. The results clearly show an increasing trend of specific activity with decreased surface density. The specific activity was 7.5 h^{-1} at a high surface density of 17 Cs/nm^2 ($20CsO_x/SiO_2$-823), and was increased by 6-fold to 44.2 h^{-1} for 0.24 Cs/nm^2 ($1CsO_x/SiO_2$-823). Importantly, such a high activity at very low surface density indicates that isolated Cs atoms on SiO_2 make up the active center for dehydrative epoxidation. Moreover, the distance between active sites is also a crucial factor for the dehydrative epoxidation, as evidenced by a continuous increase in specific activity with decreasing surface density.

2.3.3.2 Calcination temperature

An increase in calcination temperature at a constant loading of Cs_2O (1 wt.%) also affected the textural properties of the catalysts (Figure 2-10b). Below a calcination temperature of 923 K, the CsO_x/SiO_2 catalysts exhibits similar BET surface areas (174, 177, and 187 m^2/g for 723, 823, and 923 K of calcination temperature, respectively). At a calcination temperature of 1023 K, the catalyst loses surface area significantly (123 m^2/g). This considerable decrease in surface area can be attributed to the condensation of silanol groups as evidenced by differential scanning calorimetry anaylsis (Figure 2-12). An endothermic

region is present in the range of 373 ~ 633 K, which is attributed to the removal of surface adsorbates such as water molecules. In the range of 633 ~ 983 K, the process is exothermic, and can be caused by the oxidation of carbonaceous substances which are produced from acetate groups of the cesium precursor. At temperatures over 983 K, the endothermic process becomes dominant, due to the condensation of silanol groups in the surface of SiO_2 [61, 90]. The XRD patterns of these catalysts were almost identical and were different from the patterns for the catalysts with different Cs_2O loading because only small amounts of Cs_2O (1 wt.%) were loaded.

In Table 2-3 (entry 1-4), the specific activity of the catalysts was considerably affected by a calcination temperature. Although similar specific BET surface area was estimated after the calcination at 723, 823, and 923 K, the specific activity was higher for catalysts prepared at higher temperature. In contrast, the calcination at 1023 K led to a decrease in the catalytic activity of the catalyst ($1CsO_x/SiO_2$-1023). The decreased activity caused by calcination at 1023 K can be attributed to the decreased surface area, which leads to a higher surface density of Cs atoms. On the other hand, an increase in specific activity calcination for 723 ~ 923 K could be related to carbonaceous species which are produced from the cesium precursor. As evidenced by the result of a DSC analysis (Figure 2-12), the oxidation of carbonaceous species is occurred in the range of 633 ~ 983 K. Therefore, carbonaceous species can be removed insufficiently in this range of a calcination temperature. Remained carbonaceous species can cover active sites and thereby can cause a decrease in the catalytic activity.

2.3.3.3 Stability test

Using the optimum catalyst ($1CsO_x/SiO_2$-923), a long-time reaction test was performed to evaluate the stability of the catalyst. The specific activity at initial time (2 ~ 6 h) decreased rapidly from 59.3 h^{-1} to 40.1 h^{-1}. The specific activity then decreased slightly with time, and became constant for 32.7 ~ 35.8 h^{-1} after 13 h of reaction. The rapid decrease in activity at the initial time can be attributed to a decrease in basic sites caused by the leaching of Cs atoms.

Table 2-3 Catalytic performance of the supported cesium oxide catalysts on the dehydration of 2,3-butanediol.[a]

Entry	Catalysts	Surface density (Cs/nm^2)	Specific formation rate (h^{-1})			Specific activity (h^{-1})[b]
			2,3-epoxybutane (**EB**)	3-buten-2-ol (**BO**)	Methyl ethyl ketone (**MEK**)	
1	$1CsO_x/SiO_2$-723	0.24	23.7	8	7.2	31.6
2	$1CsO_x/SiO_2$-823	0.24	34.8	9.4	9.2	44.2
3	$1CsO_x/SiO_2$-923	0.23	47.8	11.5	15.8	59.3
4	$1CsO_x/SiO_2$-1023	0.35	36.2	8.7	9.6	44.8
5	$0.5CsO_x/Al_2O_3$-923	0.32	t.a.	t.a.	126	t.a.
6	$0.25CsO_x/TiO_2$-923	0.59	t.a.	t.a.	292	t.a.
7	$10CsO_x/SiO_2$-823	3.7	10.5	2.6	1.7	13.1
8	$10CsO_x/Al_2O_3$-823	5.1	0.9	0.9	0.9	1.8
9	$10CsO_x/TiO_2$-823	9	1.6	0.6	2.9	2.2

[a] Fixed-bed flow reactor, T_{rxn} = 673 K, SV = 1.38 L/(min (g cat)). [b] Sum of specific formation rate for 2,3-epoxybutane (**EB**) and 3-buten-2-ol (**BO**).

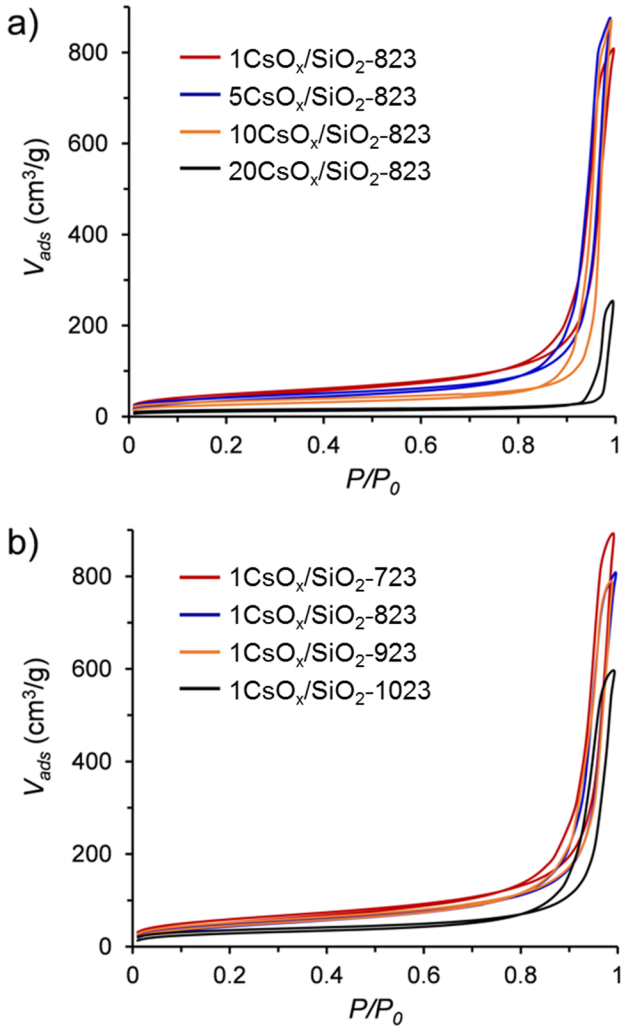

Figure 2-9. Isotherm plots of N_2 adsorption-desorption analyses for the prepared CsO_x/SiO_2 catalysts: a) the catalysts with different Cs_2O wt.% loading calcined at 823 K, b) $1CsO_x/SiO_2$ catalysts calcined at different temperatures.

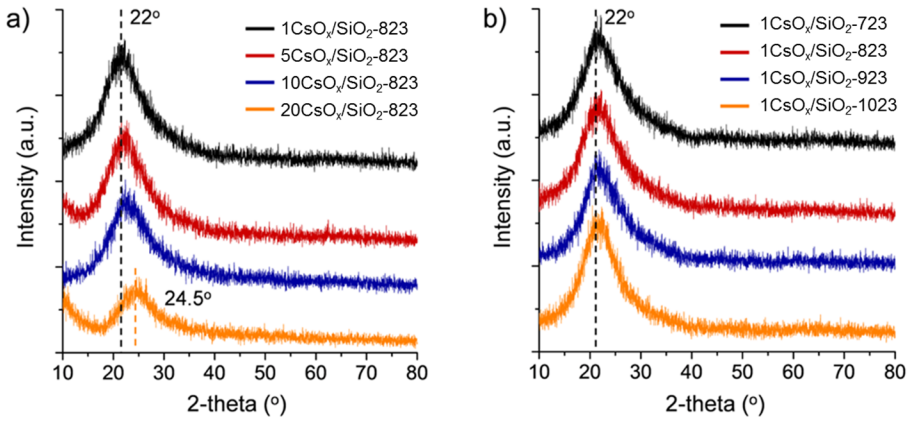

Figure 2-10. XRD patterns of the prepared CsO_x/SiO_2 catalysts: a) the catalysts with different Cs_2O wt.% loading calcined at 823 K, b) $1Cs/SiO_2$ catalysts calcined at different temperatures.

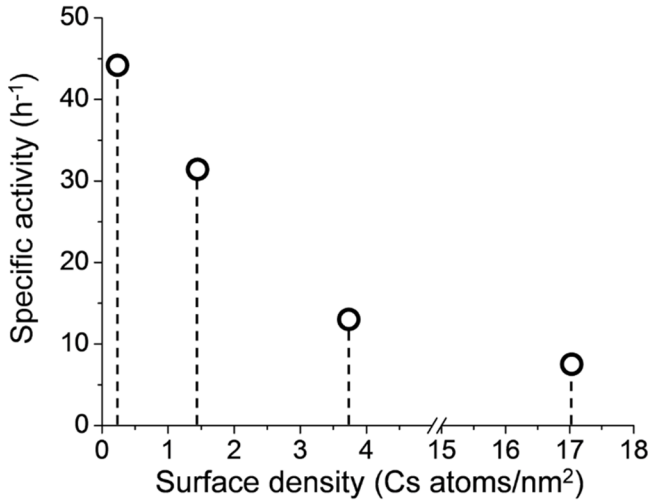

Figure 2-11. The specific activity of the CsO_x/SiO_2 catalysts calcined at 823 K as a function of surface density: $1CsO_x/SiO_2$-823 (0.24 Cs/nm^2), $5CsO_x/SiO_2$-823 (1.45 Cs/nm^2), $10CsO_x/SiO_2$-823 (3.74 Cs/nm^2), and $20CsO_x/SiO_2$-823 (17.0 Cs/nm^2).

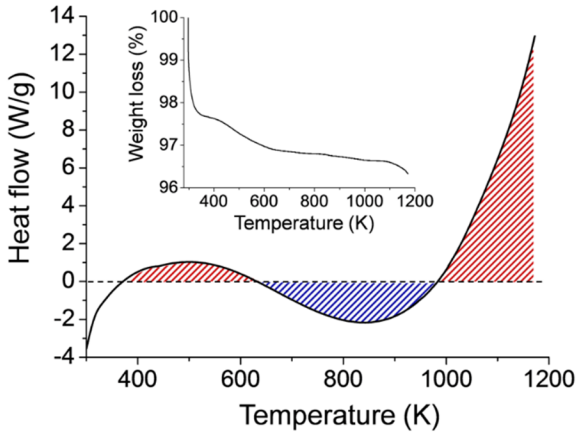

Figure 2-12. Profile for the differential scanning calorimetry analysis of the as-prepared $1CsO_x/SiO_2$. Red and blue stripe zones indicate endothermic and exothermic process, respectively. Inset shows the thermogravimetric data.

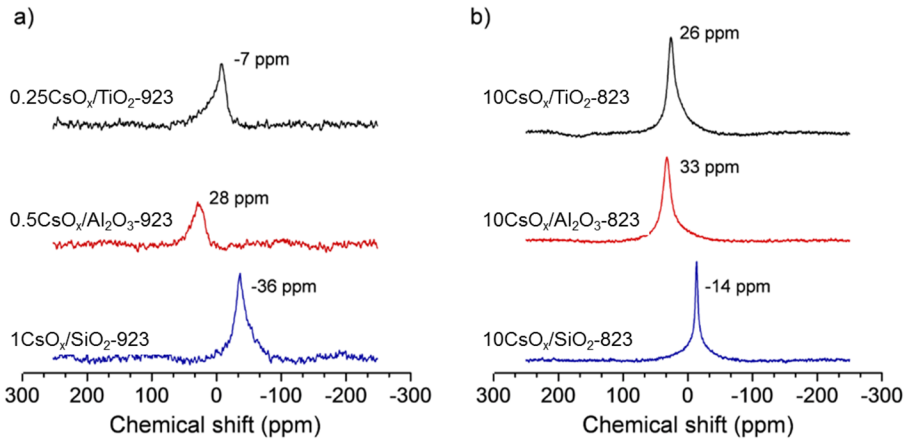

Figure 2-13. ^{133}Cs MAS NMR spectra of the supported cesium oxide catalysts: a) low surface density, b) high surface density.

2.3.4 Effect of support: Significance of the SiO_2 support

The significance of the support in the dehydrative epoxidation was further investigated by a comparison of catalysts using different supports (Al_2O_3 and TiO_2). CsO_x/Al_2O_3 and CsO_x/TiO_2 catalysts were prepared at two different conditions to compare their catalytic activity at low and high surface densities. Similar to the CsO_x/SiO_2 catalyst, Cs atoms were present as Cs^+ The textural properties of the prepared catalysts were characterized by means of N_2 adsorption-desorption, HR-TEM, and XRD analyses. In brief, crystalline cesium oxides were not observed in the catalysts, and the inter-particular porosity of the catalysts were similar (Type IV isotherm and H3 hysteresis loop at P/P0 = 0.8 – 1.0), ensuring that the internal diffusion of reactants was not a determining factor for catalytic activity.

When Al_2O_3 and TiO_2 were utilized as the support instead of SiO_2, the catalytic activity for the dehydrative epoxidation was significantly decreased compared to CsO_x/SiO_2 catalysts (Table 2-3. Entry 3, 5-9). At low surface density, $0.5CsO_x/Al_2O_3$-923 (entry 5) and $0.25CsO_x/TiO_2$-923 (entry 6) produced trace amounts of **EB** and **BO**, as opposed to $1CsO_x/SiO_2$-923. These two catalysts exhibited a considerably high specific formation rate of **MEK** and **IBA**. This rate would be an overestimated value, as the formation of **MEK** and **IBA** can be attributed to the intrinsically reactive sites of Al_2O_3 and TiO_2 rather than the basic sites formed by Cs atoms [91-93]. Moreover, by-products, such as 3-hydroxy-2-butanone, 2,3-butanedione, t-butanol, and 2-butanol were also detected. These products can be formed via a combination of side reactions,

such as dehydrogenation, hydrogenation, and undesired dehydration reactions. For CsO_x/Al_2O_3 and CsO_x/TiO_2 at a high surface density level (entry 8 and 9), the formation of **MEK** and **IBA** was suppressed due to a decrease in the exposed surface of Al_2O_3 and TiO_2, and quantifiable amounts of **EB** and **BO** were produced as well. However, the specific activity was still considerably lower than that for the CsO_x/SiO_2 catalysts.

It appeared that not only the loaded Cs atoms, but the SiO_2 support also plays a crucial role in catalyzing dehydrative epoxidation. This significance of SiO_2 indicates that the properties of a basic site can vary considerably, depending on the support, or another promotional effect of a support occurs. In this regard, the base strength and local environment of Cs atoms in the supported Cs catalysts were compared to determine how strong the influence of a support is on the properties of a basic site.

The base strength of the catalysts were compared by a Hammett indicator titration method. Among the catalysts, $10CsO_x/Al_2O_3$ exhibited the strongest base strength of $H_- > 15.0$. Other catalysts showed the comparable base strength of $8.2 < H_- < 15.0$, except for $0.25CsO_x/TiO_2$-923 that the base strength was determined to be $6.8 < H_- < 8.2$. The results indicate that the base strength can be considerably affected by the type of support.

The local structure of Cs^+ on the supported cesium oxide catalysts was examined by ^{133}Cs MAS NMR spectroscopy. At a low surface density (Figure 2-13a), Cs atoms in $1CsO_x/SiO_2$ are more negatively shielded (-36 ppm) than those in $0.5CsO_x/Al_2O_3$ (28 ppm) and $0.25CsO_x/TiO_2$ (-7 ppm). This order of chemical shift is also observed for the catalysts with a high surface density

(Figure 2-13b), but the characteristic peak was slightly shifted to a positive value (-14, 33, and 26 ppm for $10CsO_x/SiO_2$, $10CsO_x/Al_2O_3$, and $10CsO_x/TiO_2$, respectively). The values of the chemical shift for the CsO_x/SiO_2 and CsO_x/Al_2O_3 catalysts are similar to the reported values of Cs^+ exchanged silicate and boehmite [69]. It is important to note that the chemical shift is closely related to the interaction between Cs^+ and surface oxygen, the extent of which becomes stronger for a more negative chemical shift. Therefore, the more shielded (negative) chemical shift for CsO_x/SiO_2 catalysts indicates that Cs^+ in CsO_x/SiO_2 is more tightly bonded to surface oxygen than Cs^+ in CsO_x/Al_2O_3 and CsO_x/TiO_2. In addition, the positive shift for a high surface density means that the interaction is weakened when the distance between Cs atoms becomes shorter. Since the ionic radius of cesium is large (181 pm), Cs^+ which is weakly bonded to the surface would hinder the adsorption of reactant molecule on surface basic sites, resulting in a decreased activity. In addition, Cs^+ can be unstable when reaction conditions involve water molecules due to rapid leaching [69]. The variation in chemical shift for different supports can be attributed to the surface charge of the supports. The point of zero charge (PZC) for Al_2O_3 (Aeroxide® AluC) and TiO_2 (Aeroxide® P25) is 9 and 6.4, respectively, and these values are considerably higher than the 2.7 of PZC for SiO_2 (Aerosil® 200) [94]. The higher PZC value for Al_2O_3 and TiO_2 means that a less negative surface charge is present, which can result in weaker interactions between Cs^+ and surface oxygen atoms. This trend in PZC values is also in agreement with the trend for chemical shifts.

Based on these results, the type of support can have an effect on base strength, accessibility of basic sites, and stability of Cs^+ ions. However, the results do not clearly explain the extraordinary effect of SiO_2 support because base strength of $10CsO_x/Al_2O_3$ is stronger than that of CsO_x/SiO_2 catalysts, and the extent of difference in the local environment of Cs^+ ion does not appear to be so significant. Hence, there would be other promotional function of SiO_2 support that makes CsO_x/SiO_2 outstanding in the dehydrative epoxidation. The promotional function of the SiO_2 support is further discussed in section 2.3.6.3, based on the results of DFT calculations.

2.3.5 Stereochemistry in the dehydrative epoxidation

The *cis*/*trans* ratio of epoxide **EB** in the products presents an important stereochemical footprint during the dehydrative epoxidation. In our experiments, a mixture of isomers of **BD** was used (*meso*: 77%, *racemic*: 23%), and the *trans*-**EB** was dominant in the products (Figure 2-14a). For precise information, pure *meso*-2,3-butanediol (**mBD)** was utilized as a reactant, and thereby the proportion of *trans*-**EB** increased to 96% from 80% for the mixed isomers of **BD**. Based on these results, it appears that the **mBD** is selectively converted to *trans*-**EB** via the dehydrative epoxidation. Similarly, *cis*-**EB** could be derived from *racemic*-2,3-butanediol (**rBD**) as well. This indicates that the reaction is stereoselective or stereospecific since configuration of one chiral center is inverted ((*R,S*) of **mBD** to (*S,S* or *R,R*) of *trans*-**EB**, and (*S,S* or *R,R*) of **rBD** to (*R,S*) of *cis*-**EB)**.

Regarding the conformations and related energies of **mBD**, it was reported that a *gauche*-arrangement of O-C-C-O (*gauche*-**mBD**) is much favored in the gas phase over the anti-arrangement (*anti*-**mBD**) due to the stabilization by intramolecular hydrogen bonding and/or so called "*gauche* effect" [95]. Comparing the dihedral angle of the C-C-C-C for diol **mBD** and epoxide **EB**, the structure of *gauche*-**mBD** is similar to that of *cis*-**EB** rather than *trans*-**EB**. In order to have the selective conversion of stable *gauche*-**mBD** to *trans*-**EB**, the dehydrative epoxidation of **mBD** should involve a rotation on the C_2-C_3 axes of the molecule during the reaction.

There are three possible paths for the selective conversion with *gauche*-**mBD**: A rotation followed by dehydration, simultaneous rotation and dehydration, and dehydration followed by rotation (Figure 2-14b. path 1, path 2, and path 3, respectively). Feasibility of each path was examined by DFT calculations and is discussed below. In addition, the path 3 was verified experimentally to be infeasible as a reaction of *cis*-**EB** produced negligible quantity of *trans*-**EB** (1% yield).

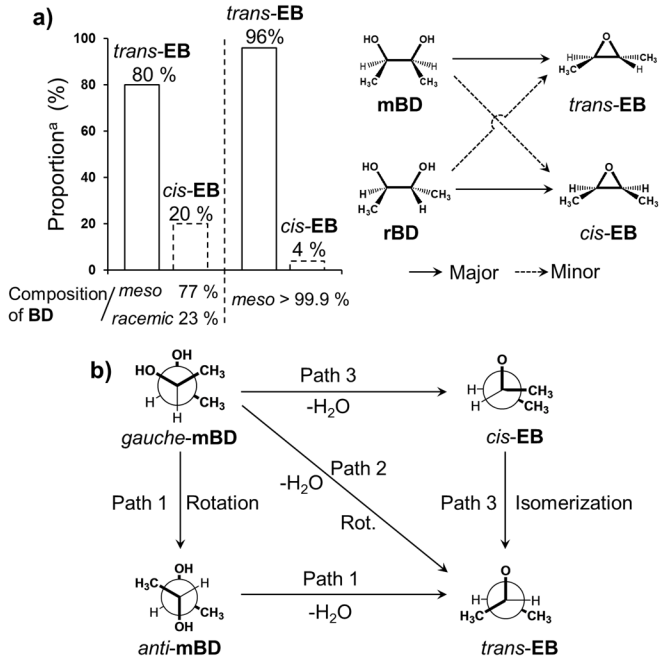

Figure 2-14. a) Conformational effect of the reactant on the dehydration of 2,3-butanediol **BD**, b) Possible paths for selective formation of *trans*-**EB** from *gauche*-**mBD**.

2.3.6 Mechanism of the dehydrative epoxidation reaction

To further understand the dehydrative epoxidation and its reaction mechanism, DFT calculations were performed on the model surface of CsO_x/SiO_2 catalyst. In this investigation, the stereochemistry in the dehydrative epoxidation was considered.

2.3.6.1 DFT calculations: meso-2,3-butanediol in the gas-phase and in the adsorption on the model surface of CsO_x/SiO_2

DFT calculations were performed at the PBE-D2 level of theory. In order to model the surface of the CsO_x/SiO_2, a SiO_2 surface was first constructed based on previous reports [64,96-98] and Cs ion was then exchanged with proton of surface silanol group. The site of exchange plays the role of a basic site (O_{base}). For efficient calculations, the surface density of 1.0 Cs/nm^2 was utilized instead of the value for the optimum catalyst (0.24 Cs/nm^2 for $1CsO_x/SiO_2$-923). Detailed descriptions of the modelled CsO_x/SiO_2 surface are shown in Figure 2-15. Table 2-4 summarizes relative energies and important geometrical parameters obtained from the DFT calculations.

The gas-phase structures of **mBD** with different conformations were optimized and the activation barrier for the rotation of *gauche*-**mBD** to *anti*-**mBD** was calculated. The structure of *gauche*-**mBD** is quite similar to that of previous reports [95] which showed the existence of intramolecular hydrogen bonding between adjacent hydroxyl groups. This intramolecular hydrogen bonding is not present in the structure of *anti*-**mBD**. For this reason, *gauche*-

mBD is more stable than *anti*-**mBD** (9 kJ/mol). It was reported that *gauche*-**mBD** exclusively presented in the gas-phase about 90% at a temperature of 298 K due to this difference of energy [95]. In order to have a rotation from the most stable *gauche*-**mBD** to *anti*-**mBD**, somewhat high energy barrier of 22 kJ/mol is required.

Through the systematic screening of the surface adsorption sites for *anti*-**mBD** and *gauche*-**mBD**, the most stable adsorption geometries for *anti*-**mBD** and *gauche*-**mBD** were found (Figure 2-16). It is important to note that the presence of interactions between H_α and O_{base} site has a considerable effect on the adsorption energy of the molecule. When the interaction between H_α and O_{base} is absent, the adsorption is weakened and the adsorption energy changes up to –61 kJ/mol. Therefore, the basic site (O_{base}) is a major adsorption site on the CsO_x/SiO_2 catalyst. The adsorption energies (ΔE_{ads}) for *anti*-**mBD** and *gauche*-**mBD** were –118 kJ/mol and –158 kJ/mol, respectively. Therefore, *gauche*-**mBD** is energetically favored over *anti*-**mBD** in the adsorption on CsO_x/SiO_2 surface as well as in the gas-phase. The stronger adsorption of *gauche*-**mBD** can be primarily attributed to the larger extent of hydrogen bonding with the surface. In case of the *gauche*-**mBD** adsorption, O_α–H_α is adsorbed on O_{base} site with hydrogen bonding (O_{base}---H_α, 1.72 Å), and another O_β-H_β site enters into two types of hydrogen bonding situations with H_{Si} and O_{Si} (O_β---H_{Si}, 1.55 Å; O_{Si}---H_β, 1.66 Å). In contrast, the adsorption of *anti*-**mBD** is only involved in two hydrogen bonding situations with the CsO_x/SiO_2 surface (O_{base}---H_α, 1.63 Å; O_β---H_{Si}, 1.60 Å). The fact that the *anti*-arrangement is intrinsically less stable

than *gauche*-arrangement in the gas-phase (9 kJ/mol) is also one reason for the smaller adsorption energy of *anti*-**mBD**.

The adsorption geometries of **mBD** allude the expected role of basic site as well as importance of surface hydroxyl site on dehydrative epoxidation. In the geometries, the bond lengths of O_{α}-H_{α} and C_3-O_{β} are slightly elongated upon the adsorptions (Table 2-4), which means that the strength of those bonds are weakened.

Table 2-4 Relative energies and structural parameters for the optimized geometries of the molecules in gas phase, the adsorption, and the transition states of the reaction. Calculations were performed at the PBE-D2 level of theory.

Model	Molecule	ΔE^a / kJ/mol	Dihedral angle[b] (O_α-C_2-C_3-O_β)	Dihedral angle[b] (C_1-C_2-C_3-C_4)	Hydrogen bonding and bond length[c] / Å				
					O_{base}-H_α	O_β-H_{Si}	O_{Si}-H_β	O_α- H_α	C_3-O_β
Gas phase	*gauche*-**mBD**	0	61°	60°	-	-	-	-0.97	-1.43
	anti-**mBD**	9	180°	178°	-	-	-	-0.97	-1.44
	cis-**EB**	105	-	0°	-	-	-	-	-
	trans-**EB**	94	-	152°	-	-	-	-	-
Adsorption	*gauche*-**mBD**	-158	65°	61°	1.72	1.55	1.66	-1	-1.44
	anti-**mBD**	-118	163°	164°	1.63	1.6	-	-1.02	-1.46
	cis-**EB**	-57	-	1°	-	1.56[d]	-	-	-
	trans-**EB**	-68	-	154°	-	1.58[d]	-	-	-
Transition States	TS1	42 (160)	(162°)	152°	-1.14	-1.06	-	1.3	2.14
	TS2	134 (292)	(92°)	105°	-1.05	-1.03	2.13	1.55	2.56
	TS3	118 (276)	(27°)	7°	2.71	1.67	1.58	1.7	2.38

[a] Energies relative to *gauche*-**mBD** in gas phase and bare surface of CsO_x/SiO_2 (ΔE_{ads} for adsorption). Values in parentheses for transition states are activation energies (ΔE_A). [b] Numbering of carbon is denoted from left to right. O_α and O_β indicate hydroxyl oxygen atoms of 2,3-butanediol. [c] Hydrogen bonding length is noted without parentheses, and chemical bond length is given in parentheses. [d] Distance between O_α and H_{Si1}.

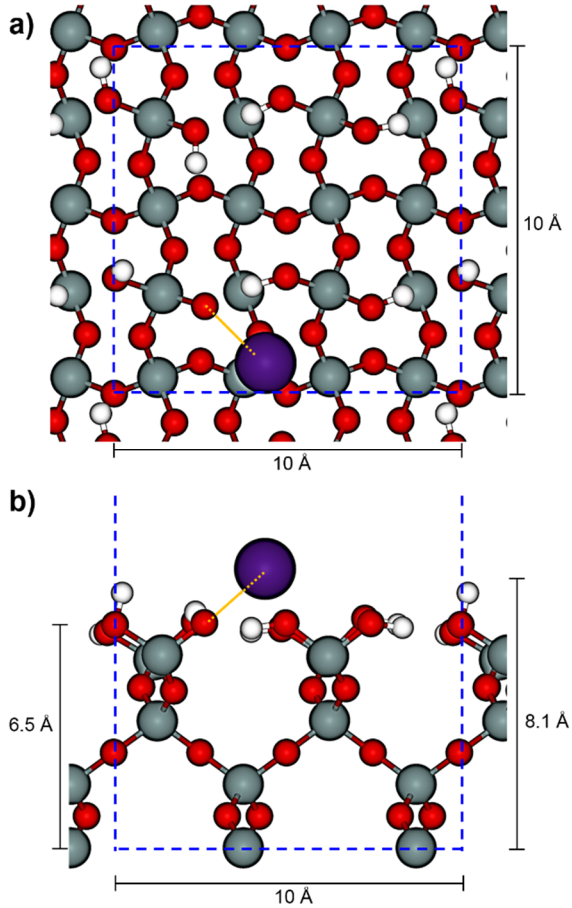

Figure 2-15. Periodic supercell of CsO_x/SiO_2 model surface. Blue dotted line indicates periodic boundary of the system. Bond distance between O_{base} and Cs^+ (represented by orange line) is 2.88 Å, which is quite similar value with experimental distance of Cs-O (2.86 Å) in Cs_2O [78].

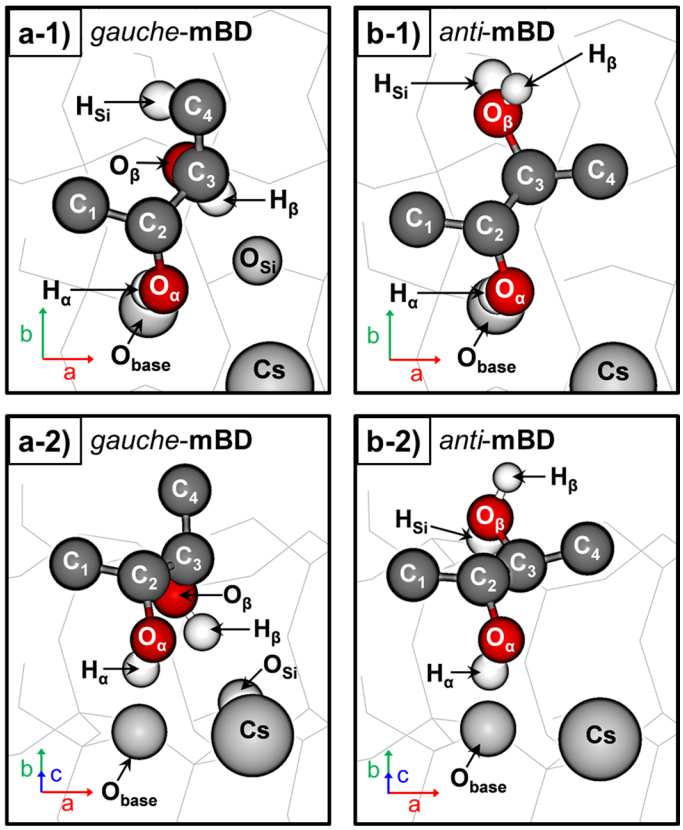

Figure 2-16. The most stable geometries for the adsorption of *gauche*-**mBD** (a-1, top view; a-2, rotated view) and *anti*-**mBD** (b-1, top view; b-2, rotated view) on the model surface of CsO_x/SiO_2. Hydrogen atoms attached to carbon atoms are not present for a clear description. O_{base}, H_{Si}, and O_{Si} represent basic site, silanol proton, and surface oxygen of SiO_2, respectively. O_α-H_α and O_β-H_β indicate hydroxyl groups of **mBD**. Calculations were performed at the PBE-D2 level of theory.

2.3.6.2 DFT calculations: Clarification of the mechanism for the dehydrative epoxidation of 2,3-butanediol

Figure 2-17 presents transition state structures for the dehydrative epoxidation of **mBD** with different conformational changes and a relative energy diagram over reaction coordinates. The three calculated transition states (Figure 2-17a, b, and c) correspond to the dehydration reaction of the paths in Figure 2-17b (path 1, path 2, and path 3, respectively. They are briefly summarized at the top of Figure 2-17).

Considering the energy diagram at initial stage of reaction coordinate (Figure 2-17d), the path 1 is relatively unfavorable than the other paths because of the required energy for the rotation from *gauche*-**mBD** into *anti*-**mBD** (22 kJ/mol) and relatively unstable geometries for *anti*-**mBD** (values for energy difference between *anti*-**mBD** and *gauche*-**mBD** are 9 and 40 kJ/mol in the gas phase and in the adsorption, respectively). However, the activation barrier (ΔE_A) for TS1 (160 kJ/mol) in the path 1 is significantly lower than that for TS2 (292 kJ/mol) and TS3 (276 kJ/mol). It is important to note that the difference in ΔE_A (TS1 vs. TS2 and TS3) is much larger than the difference between *anti*-**mBD** and *gauche*-**mBD** in the gas phase and in the adsorption. Therefore, the path 1 is the energetically most probable path for the dehydrative epoxidation although adsorption geometry for *gauche*-**mBD** is more stable than that for *anti*-**mBD**. These results explain why the dehydrative epoxidation of **mBD** selectively produces *trans*-**EB**.

When the transition state structure is considered for the most probable path (TS1, Figure 2-17a), it is found that surface hydroxyl site of SiO_2 is involved to produce H_2O during the dehydrative epoxidation. In the structure, the silanol hydrogen (H_{Si}) is transferred to the O_β-H_β hydroxyl group, resulting in the elimination of H_2O from *anti*-**mBD**. Simultaneously, the O_{base} accepts the H_α, making the O_α nucleophilic prior to forming an epoxide ring. Hence, the structure indicates that both the surface hydroxyl site and the basic site are required for the dehydrative epoxidation of **mBD**. As similar to the structure of TS1, the transition state structure in path 2 (Figure 2-17b. TS2, *gauche*-**mBD** to *trans*-**EB**) also showed the involvement of the silanol hydrogen (H_{Si}) in the elimination of H_2O. However, the distortion of carbon backbone is quite different in this case. Dihedral angle of C_1-C_2-C_3-C_4 in TS1 is 152°, which is almost identical to that for *trans*-**EB** (152° in gas-phase, 154° after adsorption). In contrast, the dihedral angle in TS2 is 105.0° which is significantly distorted from the value for *trans*-**EB**. Single point calculations on the organic molecules in TS1 and TS2 estimates the extent of distortion at 77 kJ/mol. This value is comparable to 92 kJ/mol for the difference in transition state energy ($E_{TS2} - E_{TS1}$), which indicates that the distortion in the organic molecule is a major contributor to the higher activation barrier of TS2. As opposed to TS1 and TS2, the participation of a silanol hydrogen did not occur in the transition state structure of path 3 (Figure 2-17c TS3, gauche-**mBD** to cis-**EB**). H_α is directly transfered to the O_β-H_β hydroxyl group, leading to the elimination of H_2O.

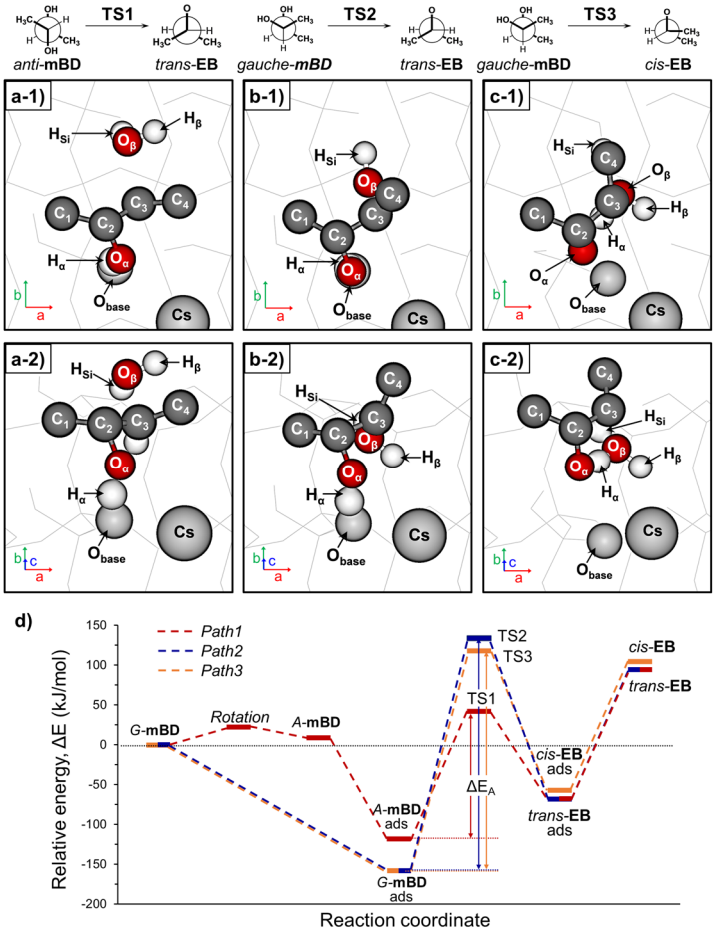

Figure 2-17. Transition state structures of *anti*-**mBD** to *trans*-**EB** (a-1. top view; a-2. rotated view), *gauche*-**mBD** to *trans*-**EB** (b-1. top view; b-2. rotated view), and *gauche*-**mBD** to *cis*-**EB** (c-1. top view; c-2. rotated view); Hydrogen atoms attached to carbon atoms are not present for a clear description. d) Total energy diagram for the dehydrative epoxidation of **mBD** over the model surface of CsO_x/SiO_2. (*anti*-, *gauche*-, adsorption, and transition state are shortened as *A*-, *G*-, ads, and TS, respectively). Calculations were performed at the PBE-D2 level of theory.

2.3.6.3 Discussion.

In the optimized adsorption geometries and transition state structure from the DFT calculations, it was found that not only the basic site, but also the surface hydroxyl site of the support are involved in dehydrative epoxidation. Importantly, the involvement of the surface hydroxyl site could explain the promotional effect of the support discussed in section 3.4. The proton in the hydroxyl site participates in the elimination of H_2O, indicating that the acidity of the proton could be important in this function. In this regard, the point of zero charge (PZC) of support is closely related to the acidity of protons of surface hydroxyl sites as the surface charge of oxides can typically change by the gain and loss of a proton. A low PZC means that the surface of the oxide favors a negatively charged state by losing its proton. Therefore, since the PZC of SiO_2 is lower (2.7), the surface hydroxyl site of SiO_2 would contain a more acidic proton than Al_2O_3 and TiO_2 (PZC = 9 and 6.4, respectively) and could be more effective in terms of the elimination of H_2O. It is noteworthy that the trend in PZC values of the supports is consistent with the trend for specific activity among $10CsO_x/SiO_2$-823, $10CsO_x/Al_2O_3$-823, and $10CsO_x/TiO_2$-823. Based on these results, it can be concluded that the promotional effect of the support originates from the role of the surface hydroxyl site in the elimination of H_2O, and the relatively higher acidity of protons in the surface hydroxyl sites of the SiO_2 support contributes the outstanding performance of CsO_x/SiO_2 on the dehydrative epoxidation.

On the basis of experimental data and DFT calculations, an S_N2-like

mechanism for dehydrative epoxidation of **mBD** is proposed (Scheme 2-2). The dehydrative epoxidation of **mBD** results in the selective formation of *trans*-**EB**, since the reaction with the conformational change of **mBD** in an *anti*-arrangement of O-C-C-O to *trans*-**EB** has a considerably lower activation barrier than the other conformational change. In this conformational change, the chirality of the carbon from which the hydroxyl group is eliminated is inverted by the backside attack of an anionic oxygen ((*R,S*) of **mBD** to give (*R,R*) of *trans*-**EB** in this model case). This inversion is quite similar to that for an S_N2 type of substitution reaction [95] and suggests that the reaction is stereospecific. The mechanism of the dehydrative epoxidation is quite different from typical dehydration reactions which proceed via an elimination mechanism (E1, E2) [100]. The dehydrative epoxidation of other vicinal diols could occur in a manner similar to that for **mBD**. The sequence of the proposed mechanism is analogous to that for the dehydration of monoethanolamine to ethyleneimine which involves both weak acid and basic sites [73]. However, the higher basicity of the $-NH_2$ group in monoethanolamine would make the reaction easier to be induced, even by SiO_2, thus making it different from dehydrative epoxidation.

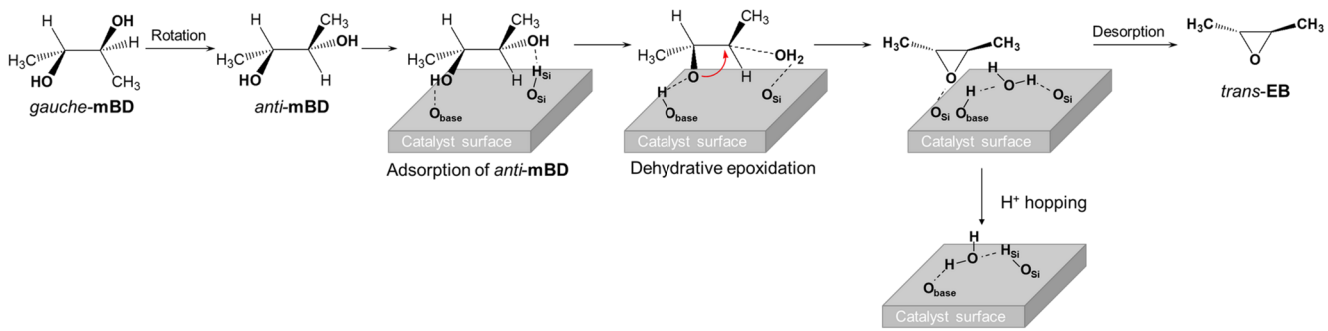

Scheme 2-2. The proposed mechanism for the dehydrative epoxidation of *meso*-2,3-butanediol: S_N2-like stereospecific production of *trans*-2,3-epoxybutane via cooperative catalysis of the basic site and the nearby hydroxyl (silanol) site.

2.3.7 Conversion of 2,3-epoxybutane into 1,3-butadiene

2.3.7.1 Precursor for 1,3-butadiene production

Compared to the products from acid catalyzed dehydration of **BD** (i.e. **MEK** and **IBA**), **EB** is much reactive due to the presence of epoxide ring. This reactivity can provide the chance for further dehydration into 1,3-butadiene. However, reaction of **EB** over acidic Al-MCM-41 catalyst resulted in dominant formation of **MEK** and showed low selectivity toward 1,3-butadiene (19% yield at total conversion, Figure 2-18). On the other hand, **BO** which is isomerized product of **EB** was very attractive precursor as high 1,3-butadiene yield of 97% was achieved with this reactant. Based on these results, **EB** itself is not suitable precursor for the production of 1,3-butadiene, and the isomerization of **EB** to **BO** is essential prior to the subsequent dehydration.

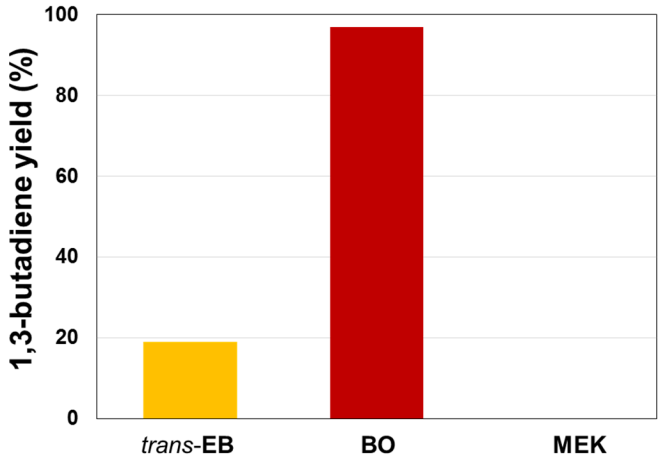

Figure 2-18. Results for reaction of *trans*-**EB**, **BO**, and **MEK** over acidic Al-MCM-41 catalyst. Reaction condition: Fixed-bed flow reactor, T_{rxn} = 523 K for *trans*-**EB** and **BO**, 623 K for **MEK**, SV = 1.38 L/(min (g cat)).

2.3.7.2 Isomerization of 2,3-epoxybutane to 3-buten-2-ol

Basic lithium phosphate (Li_3PO_4) was utilized as an catalyst for the isomerization of **EB** to **BO**. This catalyst was previously utilized in the isomerization of propylene oxide into allyl alcohol [19], which process is analogous to the isomerization of **EB** to **BO**.

Reaction results using *cis*-**EB** and *trans*-**EB** are shown in Figure 2-19. Both the *cis*- and *trans*-**EB** were selectively converted to **BO**, but the use of *trans*-**EB** resulted in a more selective reaction (92, 75 % for *trans*-**EB** and *cis*-**EB**, respectively). In the case of *trans*-**EB** isomerization, **BO** was major product and **MEK** was minor product. In contrast, the reaction of *cis*-**EB** produced *trans*-**EB** and **rBD** as well as **BO** and **MEK**. This difference between *cis*- and *trans*-**EB** could be caused by relative stability of **EB** molecule. In the selction 2.3.5, it was found that *trans*-**EB** is more energetically stable than *cis*-**EB** (11 kJ/mol). Therefore, at certain transition state, *cis*-**EB** can isomerize to *trans*-**EB** spontaneously, but *trans*-**EB** cannot.

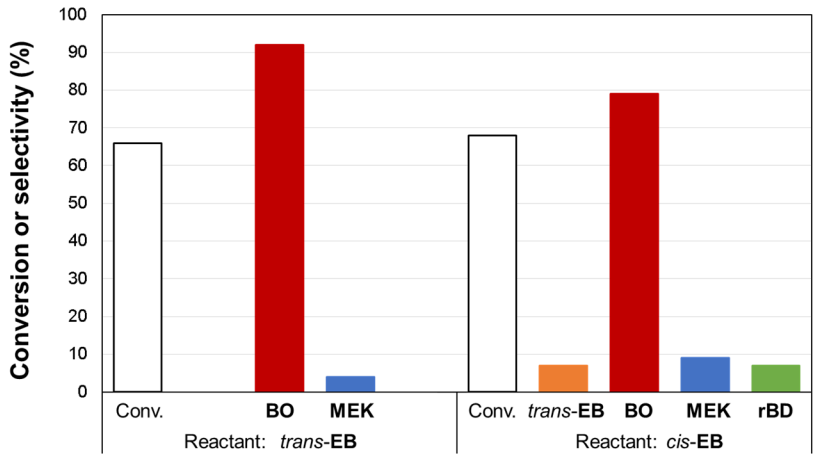

Figure 2-19. Resultis for reaction of *trans*-**EB** (left) and *cis*-**EB** (right) over basic lithium phosphate catalyst. Reaction condition: Fixed-bed flow reactor, T_{rxn} = 623 K, SV = 1.38 L/(min (g cat)).

2.3.8 Heterogeneous catalytic process for the production of 1,3-butadiene

On the basis of this study, heterogeneous catalytic process is proposed as Scheme 2-3. At the first reactor, the dehydrative epoxidation of **BD** over CsO_x/SiO_2 catalyst produces **EB** and **BO** with high selectivity. Since the boiling point (BP) of **BD** (184 ºC) is considerably higher than **EB**, **BO**, and **MEK** (55, 97, and 80 ºC, respectively), unreacted 2,3-butanediol could be easily recovered. **EB** in the low BP products is further isomerized to **BO** at the second reactor. The downstream of the second reactor contains **EB**, **BO**, and **MEK**. As difference in BP between **EB** and **MEK** is higher than that between **BO** and **MEK**, separating **EB** from the downstream is easier to be carried out. The separated **EB** is recycled to the second reactor, and **BO** is further dehydrated into 1,3-butadiene at the third reactor. The produced 1,3-butadiene has considerably low boiling point of -4.5 ºC, thus separation between 1,3-butadiene and **MEK** could be easily undertaken.

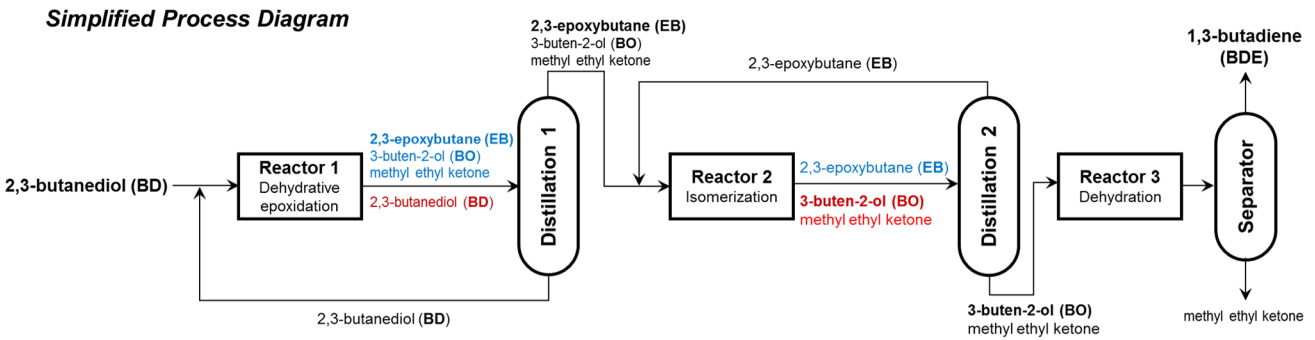

Scheme 2-3. The proposed process diagram for the heterogeneous catalytic conversion of 2,3-butanediol to 1,3-butadiene.

Chapter 3. Mesoporous Solid Acid Catalyst for the Esterification of 1-butanol with Acetic Acid

3.1 Introduction

The development of new solid acid catalysts has been essential in terms of replacing conventional homogeneous catalysts which are not only harmful to the environment, but also cause process problems [102]. A number of solid acids have been examined for this purpose, but all have certain limitations. For example, the small pores (< 2 nm) of zeolites make them difficult to use in reactions that involve the use of high molecular weight components. Sulfated zirconia catalysts, well known superacids, become deactivated during reactions, with the release of volatile sulfur-containing pollutants [103,104]. Solid acids based on supported metal oxides are potential candidates for replacing conventional mineral acids and chlorided Pt/Al_2O_3, which are harmful to the environment [105]. Among these types of catalysts, tungstated zirconia (WO_x/ZrO_2) catalysts have attracted interest, since Hino and Arata first discovered their strong acidity and low-temperature activity for light alkane isomerization [43]. It has been reported to have a high activity for alkane isomerization and the dehydration of alcohols [44-46]. The higher thermal and chemical stabilities of WO_x/ZrO_2 make them attractive for use in a variety of industrial processes [43,46]. They have the potential for use in commercial processes, including the selective catalytic reduction of NO_x to N_2, the

formation of xylene from toluene and methanol, and the oligomerization of lower molecular weight alkanes to gasoline, diesel and lubricants [106-109].

Not only the application of WO_x/ZrO_2 catalysts, but also the origin of their activity has been investigated by various characterization methods. Many investigators have attempted to find correlations between the structure of tungstate and catalytic activity [44,46,110-122]. Several proposed models and general surface species, including monotungstate, polytungstate and crystalline WO_3 have been proposed. The proposed active sites are as follows: i) slightly reduced polytungstate formed in-situ generated strong acid sites during reactions [44,111-113,138,139], ii) a balance between strong Brønsted acidity and Lewis acidity is required for a high activity [46,116,117], iii) zirconium incorporated tungstate clusters formed on WO_x/ZrO_2 produce charge compensating protons as strong Brønsted acids [110,114,115,120-122]. Regardless of the proposed models, it is generally accepted that the strong acidity is due to the strong interaction between zirconia and tungstate or by the presence of Zr-WO_x clusters. However, even though extensive research into the active site has been reported, methods for improving the activity of WO_x/ZrO_2 catalysts are generally not available. In addition, the low surface area of ZrO_2 (< 100 m^2/g) is a disadvantage in catalytic reactions, especially liquid phase reactions.

In order to improve WO_x/ZrO_2 catalysts, ordered mesoporous Zr-WO_x/SiO_2 with a high surface area and a high density of Zr-WO_x clusters is prepared. To optimize the density of the Zr-WO_x clusters, the Zr/W ratio was varied to control the tungstate species on the catalysts. Using this procedure it was

possible to investigate not only the enhanced population of Zr-WO_x clusters, but also to obtain quantitative information, which results in a better understanding of the catalysts. The structure of the tungstate present on the prepared catalysts was characterized using a variety of characterization methods. Qualitative and quantitative data of acidity were collected to find the influence of the structure of tungstate, especially Zr-WO_x clusters. Finally, the performance of the materials as an acid catalyst was examined for the esterification of 1-butanol with acetic acid and the results were compared with conventional solid acids.

3.2 Experimental

3.2.1 Preparation of mesoporous Zr-WO_x/SiO_2

Sodium tungstate dihydrate ($Na_2WO_4•2H_2O$), zirconium butoxide solution ($Zr(OC_4H_9)_4$), tetraethyl orthosilicate (TEOS) were purchased from Sigma-Aldrich; and hydrochloric acid (35-37%) was purchased from Samchun chemical.

To facilitate the formation of Zr-WO_x clusters, the sequential hydrolysis of zirconium and tungsten was introduced to the preparation procedure. A typical Zr-WO_x/SiO_2 synthesis was as follows: P123 (3.26 g, 0.562 mmol) was dissolved in H_2O (100 ml, 5.56 mol) and stirred until a clear solution was obtained. HCl (8.6 ml, 0.089 mol) was then added to the solution. A zirconium butoxide ethanol solution (v/v=1) was added dropwisely to the solution with vigorous stirring. Due to the rapid hydrolysis and condensation of zirconium butoxide in water, a white precipitate was formed immediately and gradually disappeared with stirring. After the solution became clear, an aqueous solution of sodium tungstate (3 ml) was added dropwisely and the solution stirred for 1h to insure the formation of pre-Zr-WO_x clusters. To obtain the same weight percent of tungstate (30 wt%) with different Zr/W ratio, amount of $Zr(OC_4H_9)_4$ and $Na_2WO_4•2H_2O$ were adjusted to 0~4.48 mmol and 3.47~4.48 mmol, respectively. TEOS (6.9 ml, 31 mmol) was then introduced and heated at 40 ^oC for 24 h with stirring. Subsequently, hydrothermal treat was carried out at 100 ^oC for 24 h without stirring. Resultant precipitate was filtered and washed by

ethanol and de-ionized water several time to remove sodium ion and remained acid. The filtered precipitate was dried at 80 ºC overnight and then calcined at 550 ºC for 3 h. The catalysts are denoted simply as 'WZrX', where X indicates the atomic amount of Zr relative to 10 W atoms (i.e. WZr1, atomic ratio of Zr/W=1/10).

3.2.2 Characterization

The N_2 physisorption were carried out on a Micrometrics ASAP-2010 system. The total surface area of the samples was calculated by the BET method (P/P_o=0.1~0.2). The pore volume and pore size distributions were obtained from the desorption branches of the isotherms using BJH methods. High resolution transmission electron micrograph (HR-TEM) images were obtained on a JEOL JEM-3010 microscope using bright field (BF) mode with an acceleration voltage of 300 kV. The X-ray diffraction (XRD) patterns were measured by a Rigaku D-MAX2500-PC powder X-ray diffractometer with Cu Kα radiation (1.5406 Å) in an operating mode of 50kV and 100mV.

X-ray photoelectron spectroscopy (XPS) spectra were recorded using a KRATOS AXIS electron spectrometer equipped with MgKα radiation. All of the binding energy of the peaks was referred to the C1s at 284.6 eV. Binding energies were reported within an experimental error of ±0.2 eV. Ultraviolet-visible (UV-Vis) spectra were recorded with a Jasco V670 spectrometer with diffuse reflectance spectroscopy (DRS) unit. The powdery sample was loaded into a quartz cell, and spectra were collected at 200-1000 nm referenced to KBr.

NH_3 temperature programmed desorption (TPD) was carried out using Micrometrics Autochem II chemisorption analyzer. Prior to the analysis, a 0.1g of sample was treated at 400 ^oC for 1h under a He flow. After cooling to 50 ^oC, the sample was saturated by treatment with a 10.2% NH_3/He flow. The physisorbted NH_3 was eliminated by flushing with a stream of He at 100 ^oC. After cooling to 50 ^oC, the TCD signal was recorded while the temperature was increased to 600 ^oC at a rate of 10 ^oC/min under a flow of He. In-situ FTIR spectra of NH_3 adsorption were measured with a Midac spectrometer (model 2100). A self-supported pellet containing about a 50 mg sample was placed in an In-situ IR cell, designed by Moon et al.[123] The pellet was pretreated at 250 ^oC under a He flow for 1 h. After cooling to room temperature, the pellet was exposed to NH_3 gas of 20 Torr pressure for 3 min. Desorption of NH_3 was performed by evacuation at different temperatures (30, 150 and 250 ^oC). The spectrum was recorded after desorption at each temperature. To quantify the Bronste/Lewis acidity, the previously reported peak area-amount correlation is used [124]. NH_4^+ symmetric stretching (~1450 cm^{-1}, Brønsted acid site) is typically seven-times more sensitive to asymmetric deformation of NH_3 coordinated to a Lewis acid site (~1610 cm^{-1}). To adjust for this, the peak area of the Brønsted acid site was divided by 7. In order to quantify the amounts of Bronsted acid sites, it was assumed that total acid amounts obtained from NH_3 TPD were similar to amounts of NH_3 remained after evacuation at 30^oC (in-situ FTIR).

3.2.3 Acid catalyzed reaction

Esterification of 1-butanol and acetic acid was carried out on a closed autoclave reactor with magnetic stirrer. Typically, 18.5ml of 1-butanol (200 mmol) and 11.5ml of acetic acid (200 mmol) were added to reactor. A 0.2 g sample was then introduced to the reactant. The reactor was heated to 150ºC and maintained for 4 h. Product was separated from the catalysts and analyzed by gas chromatography (Younglin ACME 6100 instrument) equipped with a FID detector and a HP-Innowax capillary column.

3.3 Results and discussion

3.3.1 Textural properties

Detailed pore structure and surface area of the materials were investigated by N_2 physisorption and the results are shown in Figure 3-1 and Table 3-1. An isotherm plot and pore size distribution of the catalysts are shown in Figure 3-1. The WZr0 to WZr5 samples show a Type IV isotherm and H1 hysteresis loop between P/P_0=0.6~0.8. This is caused by ordered cylindrical pores similar to mesoporous silicate, i.e., SBA-15. However, the WZr10 sample showed a broader hysteresis loop. Correspondingly, the WZr0 and WZr5 samples had a uniform pore size of about 5 nm and WZr10 had a smaller pore size with a non-uniform distribution. The different hysteresis loop and corresponding pore structure might be due to the penetration of zirconium into SiO_2 framework, as previously reported [117].

Table 3-1 shows the BET surface area, average pore size, and pore volume of the prepared catalysts. Except for WZr5 and WZr10, a high BET surface area of over 500 m^2/g was found. Compared to WZr0, the BET surface area increased slightly by the addition of a small amount of zirconium (WZr1), but then decreased gradually with increasing amounts of zirconium. The average pore size of the WZrX catalysts was about 5.3nm, except for WZr10, which has a smaller size of about 4.4 nm.

Three possible crystalline phases could be present on WO_x/ZrO_2, namely, monoclinic WO_3, tetragonal ZrO_2 and monoclinic ZrO_2 phases [45,120]. The

crystalline structures of ZrO_2 are not crucial factors for activity. However, the formation of monoclinic WO_3 is known as a 'boundary point of decreasing activity' on the volcano relationship between activity and WO_x loading [120]. XRD data for the prepared catalysts reveal the presence of monoclinic WO_3 for WZr0 and WZr1 (Figure 3-2 a, b). WZr3, WZr5 and WZr10 showed only a broad peak near 25° due to silica. No peaks corresponding to crystalline ZrO_2 were found for any of the catalysts. It is known that tungstate inhibits the crystallization of zirconia [45,120]. Similarly the addition of zirconium inhibits the aggregation of tungstate and results in the elimination of crystalline WO_3. Importantly, gradual shift of the peak appeared from amorphous SiO_2 also supports the insertion of Zr in SiO_2 framework.

To verify the results of N_2 physisorption and XRD, transmission electron microscopy was carried out to directly image the prepared catalysts. The results were consistent with the N_2 physisorption and XRD results. For WZr0 and WZr1, monoclinic WO_3 was formed and separated from mesoporous silica (Figure 3-3 inset) and an ordered cylindrical pore was found on WZr0 to WZr5, while the presence of cylindrical pores in WZr10 was unclear.

Table 3-1 Textural properties of the WZrX catalysts.

Catalysts	Surface area (m^2/g)	Average pore size (nm)	Pore volume (cm^3/g)
WZr0	575	5.3	0.805
WZr1	629	5.1	0.874
WZr3	558	5.3	0.814
WZr5	477	5.5	0.699
WZr10	346	4.4	0.413

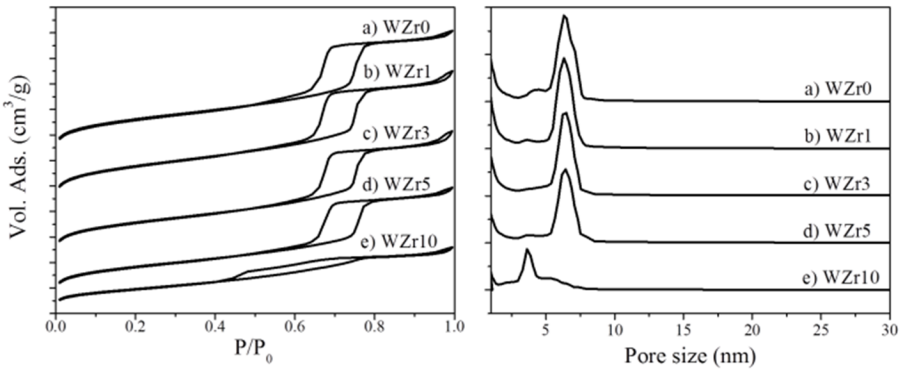

Figure 3-1. Isotherm plot (left) and pore size distribution (right): a) WZr0, b) WZr1, c) WZr3, d)WZr5, and e) WZr10.

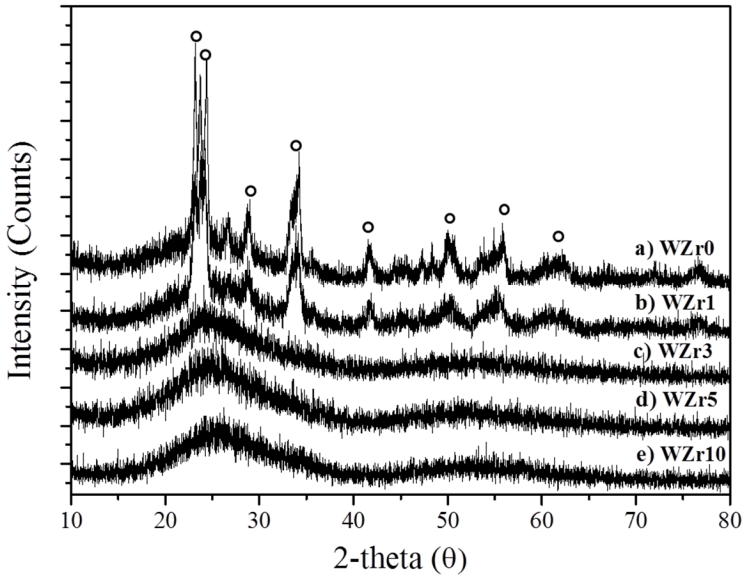

Figure 3-2. XRD patterns of WZrX catalysts: Monoclinic WO_3 (circle).

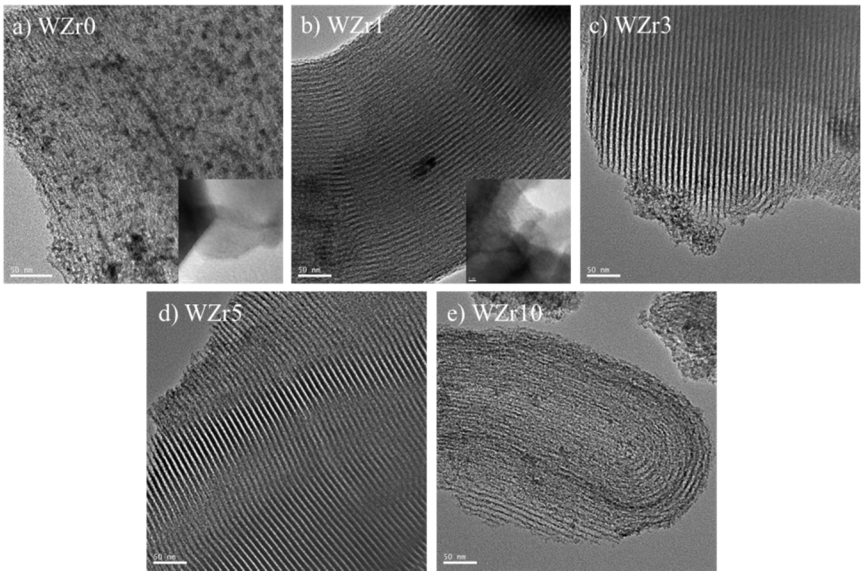

Figure 3-3. TEM images of WZrX catalysts: a) WZr0, b) WZr1, c) WZr3, d) WZr5, and e) WZr10.

3.3.2 The nature of tungstate on WZrX catalysts

X-ray photoelectron spectroscopy has been used to correlate the oxidation state and acidity of WO_x/ZrO_2 catalysts [132-134]. M.A. Corte´s-Ja´come et al. reported a trend in the XPS results for WO_x/ZrO_2 catalysts prepared at different calcination temperatures [132]. They confirmed that a large portion of the W^{5+} was present in the case of catalysts calcined at 560 ^oC, while no W^{5+} was found for samples calcined at 700 ^oC. Some of the W^{5+} was formed again when the preparation was calcined at 800 ^oC. Among these catalysts, calcination at 700 ^oC resulted in the largest amount of Brønsted acidity, but there was no clear relation between the oxidation state of W and acidity. However, it is obvious that the state of W is an important factor and that it could affect the acidity of tungstate.

XPS results for the WZrX catalysts revealed not only changes in the oxidation state, but also important evidence for the presence of Zr-WO_x clusters. Figure 3-4 shows XPS spectra of the W4f region. W4f consists of two spin-orbit components. The peak at 35.7±0.2 eV and 37.8±0.2 eV is assigned to W^{6+} species [132]. The W^{5+} species show two peaks at 34.7±0.2 eV and 36.8±0.2 eV. A relatively large amount of tungsten (about 17 %) exists as W^{5+} on WZr0. Full width at half maximum of the peak for W^{6+} (2.88 eV) is larger than that for the other catalysts, which indicates that a more diverse state of tungstate was formed. A small amount of added zirconium results in a significant decrease in the amount of W^{5+} (8%) as well as the narrowing of the W^{6+} peak (FWHM=2.32 eV). The same trend was found for increasing amounts of Zr for WZr3, WZr5

and WZr10. It is interesting to note that the presence of Zr has a significant effect on the oxidation state of W, which supports the strong interaction between Zr and W.

O1s spectra of the WZrX catalysts provided important evidence for the location of zirconium (Figure 3-5). Because zirconium was not included in the WZr0 catalyst, there would be two peaks, from SiO_2 and WO_X, in the O1s region. As can be seen in Figure 3-5, the O1s spectrum is clearly distinguished by the two peaks (532.8, 530.6 eV). The binding energy of each peak is similar to that of SiO_2 (532.6~533.3 eV) and WO_3 (530.2~530.8eV), which can be reasonably deconvoluted. Herein, O1s (Si) and O1s (tail) are denoted for the larger peak (532.8 eV) and the smaller one (530.6 eV), respectively.

Because WZr0 contains no zirconium, the O1s (tail) peak is solely contributed by tungstate. When the amount of zirconium in the catalysts is increased, the growth of O1s (tail) would be expected to be due to the similar binding energy of ZrO_2 (530.2~530.9 eV) and WO_3 (530.2~530.8 eV). However, the area ratio of O1s (tail) and O1s (Si) is almost the same for WZr0, WZr1, and WZr3 (0.041, 0.043, and 0.044, respectively). The ratio slightly increases to 0.055 for WZrX 5, and then suddenly increases to 0.21 for WZr10. This trend reveals important structural information related to the catalysts, especially the location of Zr.

Scheme 3-1 describes the influence of Zr insertion on different locations. When Zr is located on tungstate, the oxygen of W-O-Zr would be not much different from the original W-O-H or W-O-W due to the similar O1s binding energy of WO_3 and ZrO_2. Hence, the O1s (tail)/O1s (Si) ratio is retained. However, the situation is different when Zr is included in the SiO_2 framework.

Because the O1s binding energy is significantly different between SiO_2 and ZrO_2, O1s (tail) would be increased. Based on this assumption, this explains that the similar O1s (tail)/O1s (Si) ratio of WZr0, WZr1 and WZr3 is due to Zr is located on tungstate rather than on the SiO_2 framework. A slight increase in the ratio for WZr5 means that Zr starts to form in silicate as well as tungstate. For WZr10, the ratio is significantly increased to 0.21, which would result in a disordered cylindrical pore structure (consistent with the TEM images).

Tungstate based catalysts, including WO_x/ZrO_2, have been extensively studied, in attempts to determine the active site and to correlate the structure with activity [115,119,120,126-132]. Raman spectroscopy data for WO_x/ZrO_2 revealed that the presence of Zr-WO_x and tungstate with Keggin like structures [115,119,127]. Previous investigators attempted to determine the nature of the coordination and bonding of tungstate present in active WO_x/ZrO_2 [130,131]. Even though no significant differences between active and non-active catalysts were found, it was revealed that tungstate is mainly comprised of 'edge-shared octahedra' rather than corner-shared octahedra. Among the various characterizations, ultraviolet-visible spectroscopy also has been utilized to investigate the structure of tungstate [115,119,120,126-128]. On tungstate based materials, a sharp absorption between 2.6 eV and 3.6 eV is typically found, which is caused by ligand-to-metal charge transfer ($O_{2p} \rightarrow W_{5d}$) [119]. The absorption edge energy (Eg) is affected by several factors: i) the tungstate domain size (confinement effect), ii) the structure of the tungstate, iii) effect of the support [119]. There might be some differences in the tungstate structure between well-studied WO_x/ZrO_2 catalysts and our WZrX catalysts because of

the presence of silicate. However, both WO_x/ZrO_2 and WO_x/SiO_2, which have been previously studied, showed edge-shared units with Keggin-like structures [130,131,135]. It would therefore be expected that the local structure of WZrX catalysts would not differ substantially from that of WO_x/ZrO_2.

In Figure 3-6, two shoulders in WZr0 and WZr1 indicate the different tungstates are formed. The first shoulder of absorption edge energy (Eg)≈2.5 eV is assigned to monoclinic WO_3, and the second to polytungstate.[119] Because monoclinic WO_3 is presented, it is hard to obtain the Eg value of polytungstate in these catalysts. However, compared to WZr3, WZr5, and WZr10, a second shoulder starts at a lower energy. Hence, the Eg of polytungstate on the two catalysts is lower than the others. Different from WZr0 and WZr1, monoclinic WO_3 (Eg≈2.5eV) disappears on WZr3, WZr5 and WZr10, which is consistent with the TEM and XRD findings. The second shoulder, which is unclear in the case of WZr0 and WZr1, is clearly present. The Eg value is 3.3 eV for WZr3 and 3.4 eV for WZr5 and WZr10, which is assigned to presence of a polytungstate W-O-W linkage [119]. The absorption edge energy of WZr3 is higher than that for the supported 20 wt% WO_x/ZrO_2 (Eg=3.0eV). This can be attributed to the influence of the support rather than structure or domain size of tungstate. E. Iglesia et al. reported that the Eg of monotungstate present on WO_x/ZrO_2 (3.49 eV) and WO_x/Al_2O_3 (3.95 eV) was much lower than isolated molecular monotungstate, Na_2WO_4 (4.89 eV), due to tungstate-support interactions which cause increase in the effective domain size [119]. As is well known, different from Al_2O_3 and ZrO_2, the interaction between silica and tungstate is weak even when monoclinic WO_3 is formed using a very

low concentration of tungstate [119,126,136]. Hence the effect of the silica support on the increase in effective domain size would be expected to be lower than ZrO_2 and Al_2O_3, which would result in a higher Eg value. The very similar Eg values of WZr5 and WZr10 could be explained by differences in the effect of the support on the catalysts. As already shown by the XPS results, only a small amount of Zr was contained by the SiO_2 framework for WZr5, so the effect of the support would be almost the same as WZr3. However situation was somewhat different for WZr10 because large amounts of Zr were introduced. The surroundings of tungstate on WZr10 are mixed ZrO_2-SiO_2 rather than SiO_2. Therefore, it resulted an increase in the effective domain size due to effect of ZrO_2, thus decreasing the absorption edge energy.

Compared to the Keggin structured model tungstate (ammonium metatungstate, phosphotungstic acid), the Eg of WZr3 and WZr5 is slightly higher (3.0eV vs 3.3, 3.4eV). It is known that the Eg of tungstate is linearly correlated with the average number of covalent bridging W-O-W bonds [127]. The $N_{W\text{-}O\text{-}W}$ for a Keggin structure is 4. Because of the Keggin-like structure present on WO_x/ZrO_2 and WO_x/SiO_2, the $N_{W\text{-}O\text{-}W}$ of WZr3 and WZr5 would be lower than 4, consequently resulting in a lower domain size for tungstate. Zhou et al. recently demonstrated the presence of Zr-WO_x clusters through direct imaging using HAADF-STEM [121]. They reported that Zr-WO_x clusters present on WO_x/ZrO_2 are comprised of sub-nanometre tungstate with a 3D structure. Because it is known that the molecular size of Keggin structured 12-tungstate is about 1 nm [137], the slightly lower $N_{W\text{-}O\text{-}W}$ for WZr3 and WZr5 is in agreement with previous research findings.

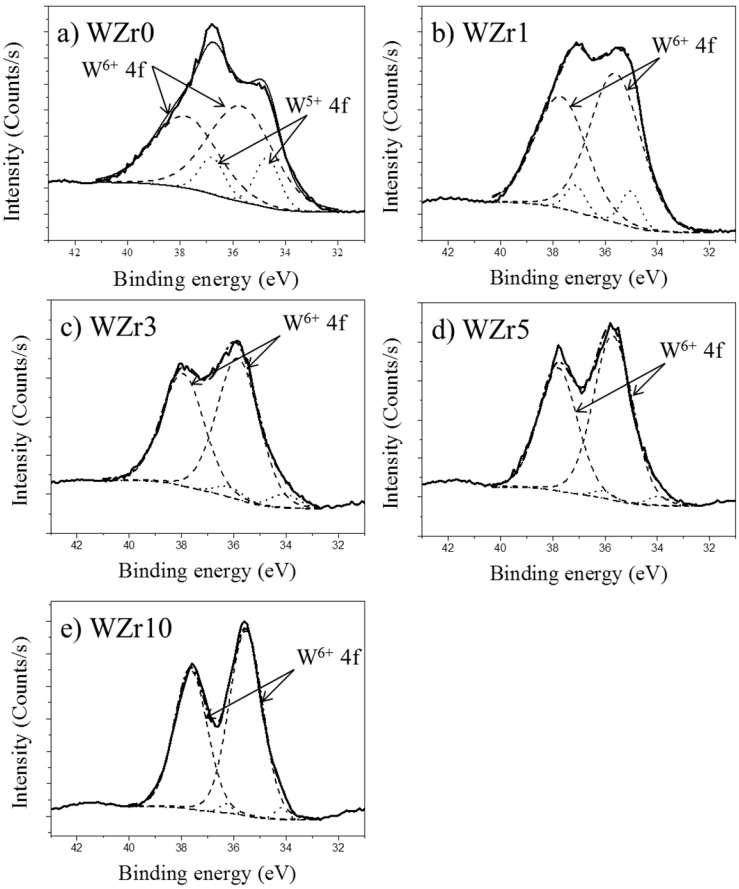

Figure 3-4. X-ray photoelectron W4f spectra of WZrX catalysts: a) WZr0, b) WZr1, c) WZr3, d) WZr5, and e) WZr10.

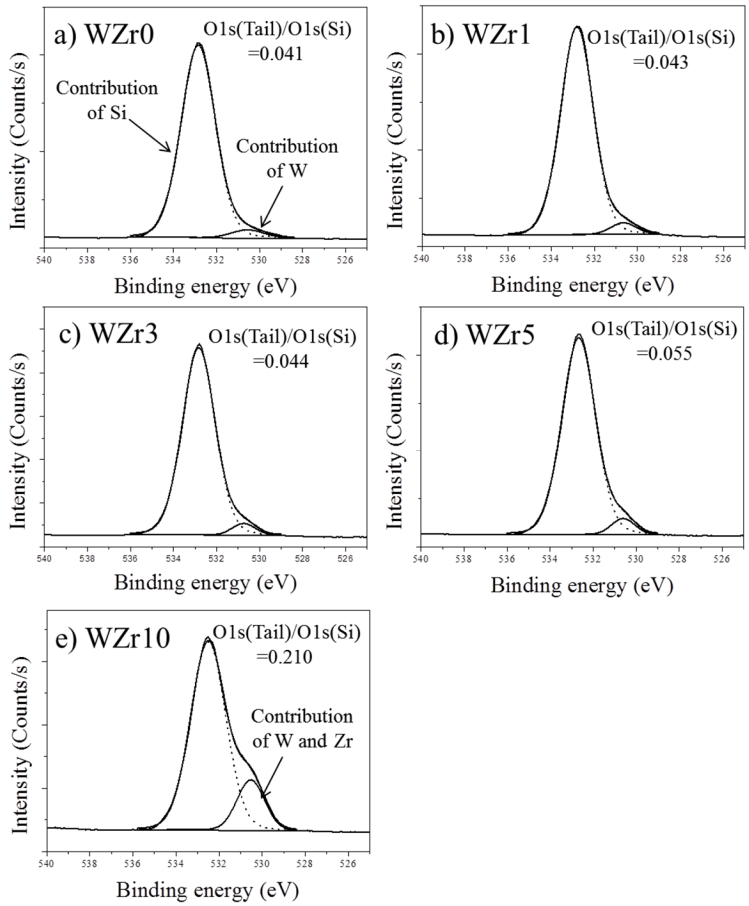

Figure 3-5. X-ray photoelectron O1s spectra of WZrX catalysts: a) WZr0, b) WZr1, c) WZr3, d) WZr5, and e) WZr10.

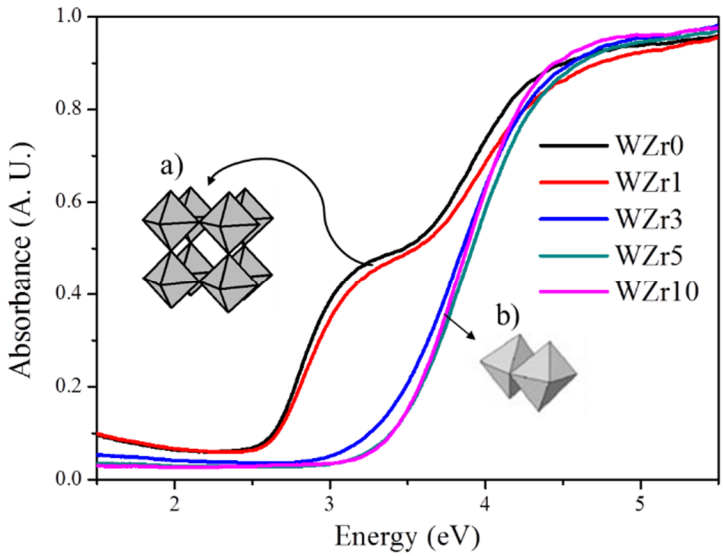

Figure 3-6. UV-Vis spectra of WZr catalysts: Assigned to a) monoclinic WO_3, and b) polytungstate and monotungstate.

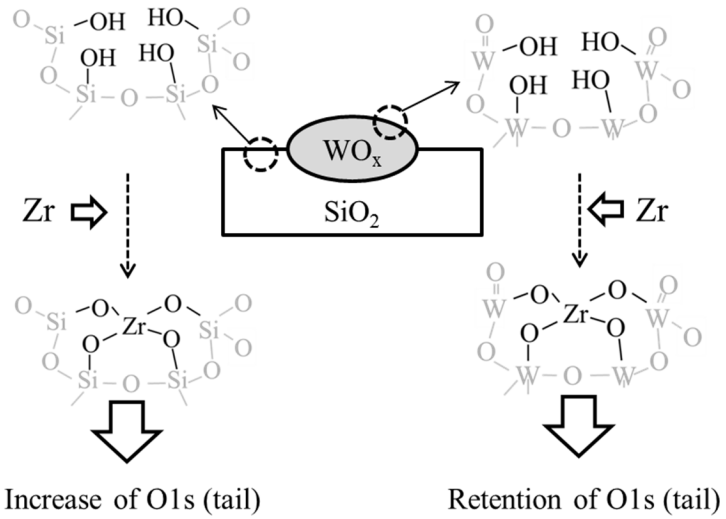

Scheme 3-1 Influence of zirconium location on O1s spectra.

3.3.3 Structure of WZrX catalysts

Based on textural properties, XPS and UV-Vis results, the structures of the WZrX catalysts are shown in scheme 3-2. The presence of monoclinic WO_3 on WZr0 and WZr1 was confirmed by TEM, XRD and UV-Vis. In addition, polytungstate is formed on these catalysts. From the XPS results, Zr is incorporated into tungstate rather than SiO_2 on WZr1 and WZr3. So, monoclinic WO_3 and Zr-WO_x clusters would be formed on WZr1. For WZr3, there are only Zr-WO_x clusters without monoclinic WO_3. Polytungstate or monotungstate in smaller sizes would be formed on WZr5, which was confirmed by the lower absorption edge energy. Thus, the maximum density of the Zr-WO_x clusters would be achieved at a Zr/W ratio of 0.3. A large amount of Zr is introduced into the SiO_2 of WZr10, so the tungstate is surrounded by ZrO_2-SiO_2 rather than SiO_2. Consequently polytungstate or monotungstate in smaller sizes are mainly formed on WZr10 with the collapse of the uniform pore structure.

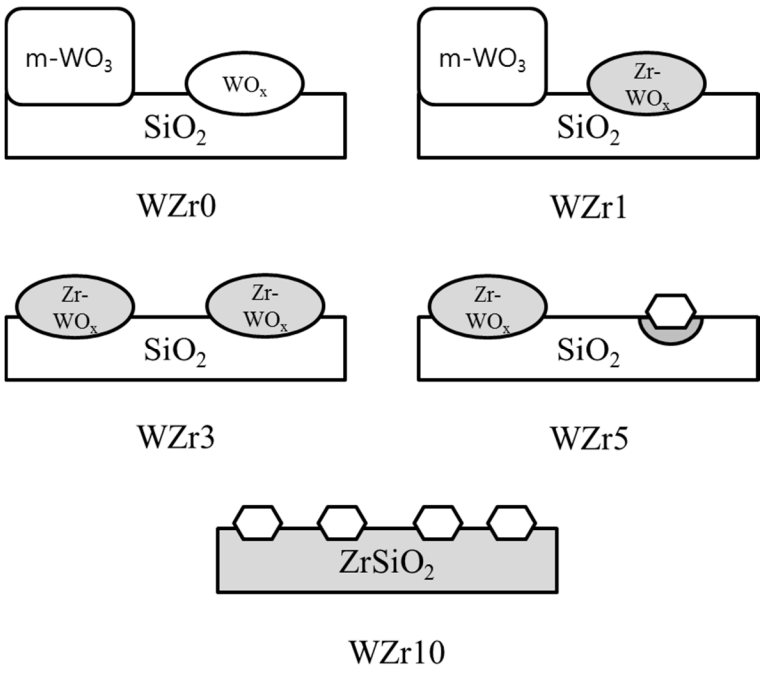

Scheme 3-2 Structures of the WZrX catalysts: Monoclinic WO_3 (m-WO_3), polytungstate (WO_x), Zr-WO_x clusters (Zr-WO_x, gray-filled), and small polytungstate and monotungstate (hexagon).

3.3.4 Acidic properties of WZrX catalysts

To insure the accurate quantification of Brønsted and Lewis acidity, the total amount of acid was estimated by NH_3 TPD and NH_3 *in-situ* FTIR was then used to determine the ratio of Brønsted and Lewis acid sites.

Figure 3-7 shows the NH_3 in-situ FTIR results for samples evacuated at 150°C. The peak maximum at 1450cm^{-1} is assigned to protonated NH_4^+ adsorbed to Brønsted acid sites. The peak of 1610cm^{-1} is assigned to NH_3 coordinatively bonded to Lewis acid sites [138]. Figure 3-8 shows the amount of Brønsted acid sites calculated from the NH_3 TPD and NH_3 *in-situ* FTIR results at each evacuation temperature. When evacuated at 30°C, the highest level of Brønsted acid sites was present on WZr5. While, at 150°C and 250°C, WZr3 contain higher amounts of Brønsted acid than the other catalysts. The Brønsted acid content for WZr0 is comparable to WZr5, except at 30°C. WZr1 and WZr10 show similar Brønsted acidities. Consequently, it can be concluded that stronger Brønsted acid sites were formed more on WZr3 to a greater extent.

It appears that the population of Zr-WO_x clusters is an important factor in terms of Brønsted acidity. In the case of WZr0, the fact that it has a higher Brønsted acidity than WZr1 can be attributed to the large number of W^{5+}-O-W^{6+} bonds, which could generate acidic protons. As discussed above, the WZr3 catalyst contained mainly Zr-WO_x clusters, while the other catalysts contained monoclinic WO_3 or tungstate in smaller sizes, and it showed a stronger Brønsted acidity than the other catalysts. The Brønsted acidities of WZr5 and WZr10 then decreased gradually because tungstate in smaller sizes was formed.

Thus, major factor influencing the Brønsted acidity of the WZrX catalysts is the population of Zr-WO_x clusters.

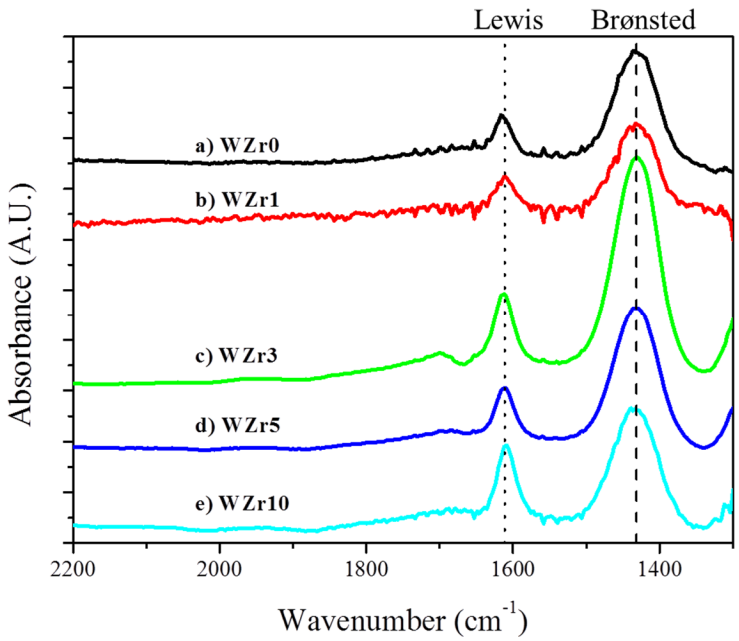

Figure 3-7. NH_3 in-situ FTIR of WZrX catalysts: Evacuation at 150 ºC.

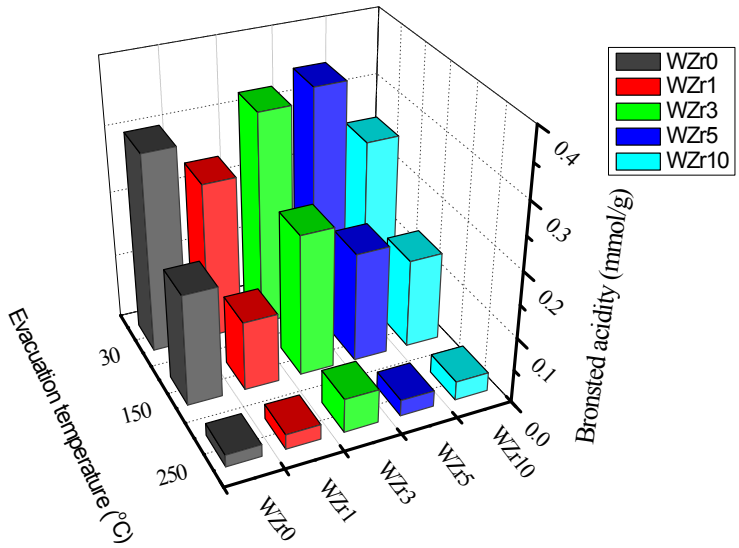

Figure 3-8. Contents of Bronsted acid sites for WZrX cataysts at each evacuation temperature.

3.3.5 Acid catalyzed reactions

It was known that esterification reactions are catalyzed by Brønsted acids. Several authors reported that Lewis acids also catalyzed this reaction [139, 140], but such catalysts are mostly supported metal chlorides, which have highly strong Lewis acid sites and can form HCl. While, supported metal oxides follow the mechanism of Brønsted acid catalyzed reactions [141].

Figure 3-9 shows the results for the prepared WZrX catalysts and control catalysts (HZSM-5, WO_x/ZrO_2) on the esterification of 1-butanol and acetic acid. Compared to the control catalysts, the WZrX catalysts showed a significantly higher activity, except for WZr10. WZr3 showed highest activity among the WZrX catalysts due to its stronger Brønsted acidity. The activities of WZr0 and WZr5 were almost the same. Significantly, the low activity of WZr10 can be explained by its relatively smaller pore size and low surface area even though it has a similar content of Brønsted acid sites as WZr1. The linear relationship between activity and Brønsted acid content at 150^{o}C verifies that the reaction is catalyzed by Brønsted acids.

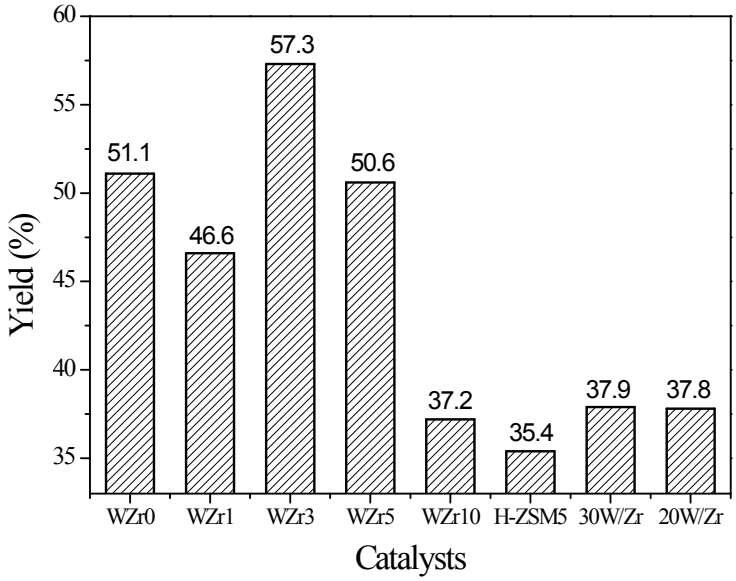

Figure 3-9. Esterification of 1-butanol and acetic acid: T=150ºC, time=4h, 1-butanol/acetic acid=1/1, catalyst 0.2 g.

Chapter 4. Summary and Conclusions

The dehydrative epoxidation of 2,3-butanediol into 2,3-epoxybutane and heterogeneous catalytic process for the production of 1,3-butadiene are reported. Among a series of supported basic metal oxides tested, a CsO_x/SiO_2 catalyst was found to be the most effective catalyst for the dehydrative epoxidation to produce 2,3-epoxybutane. The optimized catalyst with respect to loading amount of Cs_2O and calcination temperature (1 wt.% CsO_x/SiO_2 calcined at 823 K) exhibited specific activity of 59.3 h^{-1}. Based on the experimental evidences and the DFT results, the CsO_x/SiO_2 catalyst appears to be an outstanding catalyst for dehydrative epoxidation reactions for the following reasons: i) sufficiently strong base strength induced by the presence of cesium, ii) large ionic radius and low silicate dissolution that permit Cs^+ to exist on the surface and to be accessible to the reactant, iii) formation of stable basic sites in virtue of strong interactions between Cs^+ and surface oxygens caused by the low point of zero charge of SiO_2, and iv) relatively acidic protons of surface hydroxyl sites of SiO_2 which is advantageous for the elimination to H_2O. When the relative energies for different conformations (*gauche*- and *anti*-arrangement) of *meso*-2,3-butanediol is considered by the DFT calculations, *anti-meso*-2,3-butanediol is less stable than *gauche-meso*-2,3-butanediol in the gas phase (9 kJ/mol) and in the adsorption on the CsO_x/SiO_2 model surface (40 kJ/mol). However, the activation barrier for the dehydrative epoxidation of *anti-meso*-2,3-butanediol into *trans*-2,3-epoxybutane (160 kJ/mol; TS1 and path 1) is

much lower than that of *gauche-meso*-2,3-butanediol into *trans*-2,3-epoxybutane (292 kJ/mol; TS2 and path2) and *cis*-2,3-epoxybutane (276 kJ/mol; TS3 and path3). The above results allow us to conclude that the dehydrative epoxidation is mainly induced via S_N2-like stereospecific mechanism, resulting in the selective formation of *trans*-2,3-epoxybutane from *meso*-2,3-butanediol. Using the dehydrative epoxidation, the production of 1,3-butadiene from 2,3-butanediol using the heterogeneous catalytic system is proposed. Sequential processes consisting of dehydrative epoxidation, isomerization, and acid catalyzed dehydration can result in the highly selective production of 1,3-butadiene. It can conclude that dehydrative epoxidation can expand the scope of chemicals that can be produced from biomass-derived feedstocks by widening the dehydration route.

In order to replace conventional homogeneous mineral acid catalyst for the esterification reaction, mesoporous Zr-WO_x/SiO_2 catalysts with high surface areas and a high density of Zr-WO_x clusters was prepared. The sequential hydrolysis of zirconium and tungsten was used to insure the formation of pre-Zr-WO_x clusters. The Zr/W ratio was varied to find optimum conditions required for Zr-WO_x cluster formation. Except for a Zr/W ratio of 1, the prepared catalysts contained ordered cylindrical mesopores with a uniform size about 5 nm. Not only polytungstate, but inactive monoclinic WO_3 was also formed when for ratios of Zr/W<0.3. Below a certain Zr/W ratio (≈0.5), zirconium was primarily located on tungstate rather than SiO_2, which result in the formation of Zr-WO_x clusters. When the Zr/W ratio exceeded this value, less active monotungstate and polytungstate in smaller sizes were formed and

ordered mesopores sometimes collapsed. Based on the characterization results, it can be concluded that the optimum Zr/W ratio for producing a high density of Zr-WO_x clusters is ca. 0.3 (WZr3). At this ratio, a larger amount of strong Brønsted acid sites are formed. The catalytic performance of Zr-WO_x/SiO_2 catalysts for the esterification of 1-butanol and acetic acid was significantly improved compared to HZSM-5 and WO_x/ZrO_2. Among the Zr-WO_x/SiO_2 catalysts studied, the highest activity was found for a Zr/W ratio of 0.3 because of its high Brønsted acidity as the result of the high density of Zr-WO_x clusters.

Bibliography

[1] J. C. S. Ruiz, J. A. Dumesic, *Energy Environ. Sci.* **2011**, 4, 83-99.

[2] S. V. Vassilev, D. Baxter, L. K. Andersen, C. G. Vassleva, *Fuel* **2010**, 89, 913-933.

[3] J. G. Speight, *The Chemistry and Technology of Petroleum, Marcel Dekker* **1999** pp. 215-216, ISBN 0-8247-0217-4.

[4] S. Dutta, *ChemSusChem* **2012**, 5 2125-2127.

[5] L. Petrus, M. A. Noordermeer, *Green Chem*. **2006**, 8, 861-867.

[6] E. L. Kunkes, D. A. Simonetti, R. M. West, J. C. S. Ruiz, C. A. Gärtner, J. A. Dumesic, *Science* **2008**, 322, 417-421.

[7] M. E. Zakrzewska, E. B. Łukasik, R. B. Łukasik, *Chem. Rev*. **2011**, 111, 397-417.

[8] J. N. Chheda, Y. R. Leshkov, J. A. Dumesic, *Green Chem*. **2007**, 9, 342-350.

[9] R. Weingarten, G. A. Tompsett, W. C. Conner, G. W. Huber, *J. Catal.* **2011**, 279, 174-182.

[10] A. Dias, M. Pillinger, A. Valente, *J. Catal*. **2005**, 229, 414-423.

[11] M. Chidambaram, A. T. Bell, *Green Chem.* **2010**, 12, 1253-1262.

[12] Y. R. Leshkov, C. J. Barrett, Z. Y. Liu, J. A. Dumesic, *Nature* **2007**, 447, 982-985.

[13] L. Bui, H. Luo, W. R. Gunther, Y. R. Leshkov, *Angew. Chem. Int. Ed.* **2013**, 52, 8022-8025.

[14] J. Q. Bond, D. M. Alonso, D. Wang, R. M. West, J. A. Dumesic, *Science* **2010**, 327, 1110-1114.

[15] Y. Choi, D. S. Park, H. J. Yun, J. Baek, D. Yun, J. Yi, *ChemSusChem* **2012**, 5, 2460-2468.

[16] D. S. Park, B. K. Kwak, N. D. Kim, J. R. Park, J. H. Cho, S. Oh, J. Yi, *ChemCatChem* **2012**, 4, 836-843.

[17] D. Yun, T. Y. Kim, D. S. Park, Y. S. Yun, J. W. Han, J. Yi, *ChemSusChem* **2014**, 7, 2193-2201.

[18] A. Corma, S. Iborra, A. Velty, *Chem. Rev.* **2007**, 107, 2411-2502.

[19] A. Harden, G. S. Walpole, *Proc. Royal Soc.* **1906**, B77, 399–405.

[20] J.H. Cho, C. Rathnasingh, H. Song, B.W. Chung, H.J. Lee, D. Seung, *Bioprocess Biosyst. Eng.* **2012**, 35, 1081–1088.

[21] S. H. Han, J. E. Lee, K. Park, Y. C. Park, *N. Biotechnol.* **2013**, 30, 166–172.

[22] T. Hassler, D. Schieder, R. Pfaller, M. Faulstich, V. Sieber, *Bioresour. Technol.* **2012**, 124, 237–244.

[23] M. Y. Jung, C. Y. Ng, H. Song, J. Lee, M. K. Oh, *Appl. Microbiol. Biotechnol.* **2012**, 95, 461–469.

[24] M. Ehsani, M. R. Fernández, J. A. Biosca, A. Julien, S. Dequin, *Appl. Environ. Microbiol.* **2009**, 75, 3196-3205

[25] C. Y. Ng, M. Y. Jung, J. Lee, M. K. Oh, *Microb Cell Fact,* **2012**, 11, 68-81

[26] J. Lian, R. Chao, H. Zhao, *Metab. Eng.* **2014**, 23, 92-99

[27] H. Nan, S. O. Seo, E. J. Oh, J. H. Seo, J. H. D. Cate, Y. S. Jin, *Appl. Microbiol. Biotechnol.* **2014**, 98, 5757-5764.

[28] S. Atsumi, A. F. Cann, M. R. Connor, C. R. Shen, K. M. Smith, M. P. Brynidlsen, K. J. Chou, T. Hanai, J. C. Liao, *Metab. Eng.* **2008**, 10, 305-311.

[29] M. Inui, M. Suda, S. Kimura, K. Yasuda, H. Suzuki, H. Toda, S. Yamamoto, S. Okino, N. Suzuki, H. Yukawa, *Appl. Microbiol. Biotechonol.* **2007**, 77, 1305-1316.

[30] G. K. Donaldson, L. L. Huang, L. A. Maggio-Hall, V. Nagarajan, C. E. Nakamura, W. Suh, **2007** International Patent WO 2007/041269

[31] J. C. Liao, S. Atsumi, M. P. Brynildsen, A. F. Cann, K. J. Chou, C. R. Shen, K. M. Smith, T. Hanai, M. R. Connor **2008** International Patent WO 2008/124523

[32] U. Gunawardena, P. Meinhold, M. W. Peters, J. Urano, R. Feldman **2008** International Patent WO 2008/010124

[33] T. Buelter, A. Hawkins, K. Kersh, P. Meinhold, M. Peters, E. Subbian **2008** International Patent WO 2008/143704

[34] E. J. Steen, R. Chan, N. Prasad, S. Myers, C. J. Petzold, A. Redding, M. Ouellet, J. D. Keasling, *Microb. Cell. Fact*. **2008**, 7, 36.

[35] D. R. Nielsen, E. Leonard, S. H. Yoon, H. C. Tseng, C. Yuan, K. L. Prather, *Metab. Eng.* **2009**, 11, 262-273.

[36] Web page: http://www.butamax.com/renewable-fuel-technologies.aspx

[37] Web page: http://www.butalco.com/

[38] E. Celinska, W. Grajek, *Biotechnol. Adv.* **2009**, 27, 715.

[39] (a) N. Shlechter, D. F. Othmer, S. Marshak, *Ind. Eng. Chem.* **1945**, 37, 900; (b) N. Shlechter, D. F. Othmer, R. Brand, *Ind. Eng. Chem.* **1945**, 37, 905.

[40] J. Baek, T. Y. Kim, W. Kim, H. J. Lee, J. Yi, Green Chemistry 2014, 16(7), 3501-3507.

[41] T. A. Peters, N. E. Benes, A. Holme, J. T.F. Keurentjes, *Appl. Catal. A* **2006**, 297, 182-188.

[42] A. Corma, H. Garcia, S. Iborra, J. Primo, *J. Catal.* **1989**, 120, 78-87.

[43] M. Hino, K. Arata, *J. Chem. Soc. Chem. Commun.* **1988**, 1259–1260.

[44] D. G. Barton, S. L. Soled, G. D. Meitzner, G. A. Fuentes, E. Iglesia, *J. Catal.* **1999**, 181, 57.

[45] G. Larsen, E. Lotero, L. M. Petkovic, D. S. Shobe, *J. Catal.* **1997**, 169, 67.

[46] J.G Santiesteban, J.C Vartuli, S. Han, R.D Bastian, C.D Chang, *J. Catal.* **1997**, 168, 431.

[47] H. Duan, D. Sun, Y. Yamada, S. Sato, *Catal. Commun.* **2014**, 48, 1-4.

[48] S. Ramayya, A. Brittain, C. DeAlmeida, W. Mok, M. J. Antal, *Fuel* **1987**, 66, 1364-1371.

[49] P. J. Chong, G. Curthoys, *Zeolites* **1981**, 1, 41-51.

[50] K. Mori, Y. Yamada, S. Sato, *Appl. Catal. A* **2009**, 366, 304-308.

[51] D. Zhang, S. A. I. Barri, D. Chadwick, *Appl. Catal. A* **2011**, 400, 148-155.

[52] Z. Dai, B. Hatano, H. Tagaya, *Appl. Catal. A* **2004**, 258, 189-193.

[53] W. Zhang, D. Yu, X. Ji, H. Huang, *Green Chem.* **2012**, 14, 3441-3450.

[54] A.V. Tran, R. P. Chambers, *Biotechnol. Bioeng.* **1987**, 29, 343-351.

[55] G. Kresse, J. Furthmuller, *Phys. Rev. B* **1996**, 54, 11169-11186.

[56] J. P. Perdew, K. Burke, M. Ernzerhof, *Phys. Rev. Lett.* **1996**, 77, 3865-3868.

[57] P. E. Blöchl, *Phys. Rev. B* **1994**, 50, 17953-17979.

[58] S. Grimme, *J. Comput. Chem.* **2006**, 27, 1787-1799.

[59] F. Zhang, J. D. Gale, B. P. Uberuaga, C. R. Stanek, N. A. Marks, *Phys. Rev. B* **2013**, 88, 054112-054112-7.

[60] D. W. Sindorf, G. E. Maciel, *J. Am. Chem. Soc.* **1983**, 105, 1487-1493.

[61] I-S.Chuang, G. E. Maciel, *J. Phys. Chem. B* **1997**, 101, 3052-3064.

[62] L. T. Zhuravlev, *Langmuir* **1987**, 3, 316-318.

[63] J. B. Per, A. L. Hensley, Jr., *J. Phys. Chem*. **1968**, 72, 2926-2933.

[64] J. Handzlik, J. Ogonowski, *J. Phys. Chem. C* **2012**, 116, 5571-5584.

[65] A. F. Wright, A. J. Leadbetter, *Philos. Mag.* **1975**, 31, 1391-1401.

[66] H. W. Park, S. Park, D. R. Park, J. H. Choi, I. K. Song, *Korean J. Chem. Eng.* **2011**, 28, 1177-1180.

[67] A. Zecchina, S. Bordiga, C. Lamberti, G. Spoto, L. Carnelli, *J. Phys. Chem.* **1994**, 98, 9577-9582.

[68] D. H. Olson, N. KhoSrOvani, A.W. Peters, B. H. Toby, *J. Phys. Chem. B* **2000**, 104, 4844-4848.

[69] a) Y. Kim, R. J. Kirkpatrick, *Geochimica et Cosmochimica Acta* **1997**, 61, 5199-5208; b) Y. Kim, R. J. Kirkpatrick, R. T. Cygan, *Geochimica et Cosmochimica Acta* **1996**, 60, 4059-4074.

[70] G. Henkelman, H. Jonsson, *J. Chem. Phys.* **2000**, 113, 9978-9985.

[71] G. Henkelman, B. P. Uberuaga, H. Jonsson, *J. Chem. Phys.* **2000**, 113, 9901-9904.

[72] a) S. Sato, R. Takahashi, T. Sodesawa, N. Honda, *J. Mol. Catal. A* **2004**, 221, 177-183; b) S. Sato, F. Sato, H. Gotoh, Y. Yamada, *ACS Catal*. **2013**, 3, 721-734.

[73] A) H. Tsuneki, *Appl. Catal. A* **2001**, 221, 209-217; b) H. Tsuneki, K. Ariyoshi, *Appl. Catal. A* **2007**, 331, 95-99.; c) Y. Sun, H. Yan, D. Liu, D. Zhao, *Catal. Commun*. **2008**, 9,924-930.

[74] a) G. Connell, J. A. Dumesic, *J. Catal.* **1987**, 105, 285-298; b) P. Carniti, A. Gervasini, S. Bennici, *J. Phys. Chem. B* **2005**, 10, 1528-1536.

[75] a) W. H. Brown, C. S. Foote, B. L. Iverson, *Organic Chemistry fourth edition,* Thomson Brooks/Cole: Belmont, CA, **2005**; pp 213-214, 343; b) J. M. Hornback, *Organic Chemistry second edition*, Thomson Brooks/Cole: Belmont, CA, **2006**; pp 272.

[76] P. Burk, S. Tamp, *J. Mol. Struc-THEOCHEM* **2003**, 638, 119-128.

[77] I. Dzidic, P. Kebarle, *J. Phys. Chem.* **1970**, 74, 1466-1474.

[78] S. K. Searla, I. Dzidic, P. Kebarle, *J. Am. Chem. Soc.* **1969**, 91, 2810-2811.

[79] P. Burk, K.Sillar, I. A. Koppel, *J. Mol. Struc.-THEOCHEM* **2001**, 543, 223-231.

[80] M. Huang, A. Adnot, S. Kaliaguine, *J. Catal.* **1992**, 137, 322-332.

[81] W. J. Mortier, *J. Catal.* **1978**, 55, 138-145.

[82] D. Barthomeuf, *Catal. Rev.* **1996**, 38, 521-612.

[83] H. Hattori, *Chem. Rev.* **1995**, 95, 537-558.

[84] S. B. Waghmode, R. Vetrivel, S. G. Hegde, C. S. Gopinath, S. Sivasanker, *J. Phys. Chem. B* **2003**, 107, 8517-8523.

[85] T. Horiuchi, H. Hidaka, T. Fukui, Y. Kubo, M. Horio, K. Suzuki, T. Mori, *Appl. Catal. A* **1998**, 167, 195-202.

[86] R. Bal, K. Chaudhari, S. Sivasanker, *Catal. Letters* **2000**, 70, 75-78.

[87] a) Y. T. Chua, A. R. Mohamed, S. Bhatia, *Appl. Catal. A* **2008**, 343, 142-148; b) A. G. Dedov, G. D. Nipan, A. S. Loktev, A. A. Tyunyaev, V. A. Ketsko, K. V. Parkhomenko, I. I. Moiseev, *Appl. Catal. A* **2011**, 406, 1-12; c) U. Simon, O. Görke, A. Berthold, S. Arndt, R. Schomäcker, H. Schubert, *Chem. Eng. J.* **2011**, 168, 1352-1359.

[88] E. Lippmaa, M. Magi, A. Samoson, G. Engelhardt, A.R. Grimmer, *J. Am. Chem. Soc*. **1980**, 102, 4889-4893.

[89] P. W. J. G. Wijnen, T. P. M. Beelen, J. W. de Haan, C. P. J. Rummens, L. J. M. van de Ven, R.A. van Santen, *J. Non-Cryst. Solids* 1989, 109, 85-94.

[90] L. T., Zhuravlev, *Colloids Surf., A* **2000**, 173, 1-38.

[91] B. M. Reddy, A. Khan, *Catal. Rev.* **2005**, 47, 257-296.

[92] M. M. Bhasin, J. H. McCain, B. V. Vora, T. Imai, P. R. Pujadó, *Appl. Catal. A* **2001**, 221, 397-419.

[93] K. Nakagawa, M. Okamura, N. Ikenaga, T. Suzuki, T. Kobayashic, *Chem. Commun.*, **1998**, 1025-1026.

[94] M. Kosmulski, *Adv. Colloid. Interfac*. **2009**, 152, 14-25

[95] a) A. J. L. Jesus, M. T. S. Rosado, I. Reva, R. Fausto, M. E. Eusébio, J. S. Redinha, *J. Phys. Chem. A* **2006**, 110, 4169-4179; b) A. J. L. Jesus, M. T. S. Rosado, M. L. P. Leitão, J. S. Redinha, *J. Phys. Chem. A* **2003**, 107, 3891-3897.

[96] J. J. Mortensen, M. Parrinello, *J. Phys. Chem. B* **2000**, 104, 2901-2907.

[97] J. Handzlik, R. Grybos, F. Tielens, *J. Phys. Chem. C* **2013**, 117, 8138-8149.

[98] A. Rimola, D. Costa, M. Sodupe, J. F. Lambert, P. Ugliengo, *Chem. Rev.* **2013**, 113, 4216-4313.

[99] J. Tai, Q. Ge, R. J. Davis, M. Neurock, *J. Phys. Chem. B* **2004**, 108, 16798-16805.

[100] A) K. Thomke, *J. Catal.* **1976**, 44, 339-344; b) S. Delsarte, P. Grange, *Appl. Catal. A* **2004**, 259, 269-279; c) M.G. Cutrufello, I. Ferino, V. Solinas, A. Primavera, A. Trovarelli, A. Aurouxc, C. Picciauc, *Phys. Chem. Chem. Phys.* **1999**, 1, 3369-3375.

[101] T. Imanaka, Y. Okamoto, S. Teranishi, *Bull. Chem. Soc. Jpn.* **1972**, 45, 1353-1357.

[102] T. A. Peters, N. E. Benes, A. Holmen, J.T.F. Keurentjes, *Appl. Catal. A* **2006**, 297, 182.

[103] F.R. Chen, G. Coudurier, J.F. Joly, J.C. Vedrine, *J. Catal.* **1993**, 143, 616.

[104] R. Srinivasan, R.A. Keogh, D.R. Milburn, B.H. Davis, *J. Catal.* **1995**, 153, 123.

[105] J. M. Thomas, *Sci. Am.* **1992**, 266, 112.

[106] *US Pat.* 5 401 478, **1995**.

[107] *US Pat.* 5 552 128, **1996**.

[108] *US Pat.* 5 563 310, **1996**.

[109] *US Pat.* 5 453 556, **1995**.

[110] M. Scheithauer, T.K. Cheung, R.E. Jentoft, R.K. Grasselli, B.C. Gates, H. Knözinger, *J. Catal.* **1998**, 180, 1.

[111] D. G. Barton, S. L. Soled, E. Iglesia, *Top. Catal.* **1998**, 6, 87.

[112] C. D. Baertsch, S. L. Soled, E. Iglesia, *J. Phys. Chem. B*, **2001**, 105, 1320.

[113] C. D. Baertsch, K. T. Komala, Y. Chua, E. Iglesia, *J. Catal.* **2002**, 205, 44.

[114] S. Kuba, P. Lukinskas, R. Ahmad, F. C. Jentoft, R. K. Grasselli, B. C. Gates, H. Knözinger, *J. Catal.* **2003**, 219, 376.

[115] M. Scheithauer, R. K. Grasselli, H. Knözinger, *Langmuir*, **1998**, 14, 3019.

[116] J.C. Vartuli, J.G. Santiesteban, P. Traverso, N. Cardona-Martinéz, C.D. Chang, S.A. Stevenson, *J. Catal.* **1999**, 187, 131.

[117] D.C. Calabro, J.C. Vartuli and J.G. Santiesteban, *Top. Catal.* **2002**, 18, 231.

[118] R. D. Wilson, D. G. Barton, C. D. Baertsch, E. Iglesia, *J. Catal.* **2000**, 194, 175.

[119] D. G. Barton,M. Shtein,R. D. Wilson,S. L. Soled,E. Iglesia, *J. Phys. Chem. B*, **1999**, 103, 630.

[120] E. I. Ross-Medgaarden, W. V. Knowles, T. Kim, M. S. Wong, W. Zhou, C. J. Kiely, I. E. Wachs, *J. Catal.* **2008**, 256, 108.

[121] W. Zhou, E. I. Ross-Medgaarden, W. V. Knowles, M. S. Wong, I. E. Wachs, C. J. Kiely, *Nat. Chem.* **2009**, 1, 722.

[122] N. Soultanidis,W. Zhou,A. C. Psarras,A. J. Gonzalez,E. F. Iliopoulou,C. J. Kiely, I. E. Wachs, M. S. Wong, *J. Am. Chem. Soc.* **2010**, 132, 13462.

[123] S. H. Moon, H. Windawi and J. R. Katzer, *Ind. Eng. Chem. Fundam.* **1981**, 20, 396-399.

[124] L.M. Cornaglia, E.A. Lombardo, J.A. Anderson, J.L. Gracia Fierro, *Appl. Catal.* **1993**, 100, 37.

[125] J. Iglesias, J. A. Melero, L. F. Bautista, G. Morales, R. Sánchez-Vázquez, M. T. Andreola, A. Lizarraga-Fernández, *Catal. Today*, **2011**, 167, 46.

[126] A. Guti´errez-Alejandre, J. Ram´ırez, G. Busca, *Catal. Lett.* **1998**, 56, 29.

[127] E. I. Ross-Medgaarden, Israel E. Wachs, *J. Phys. Chem. C*, **2007**, 111, 15089.

[128] J. Macht, C. D. Baertsch, M. May-Lozano, S. L. Soledb, Y. Wang, E Iglesia, *J. Catal.* **2004**, 227, 479.

[129] X. Chen, G. Clet, K. Thomas, M. Houalla, *J. Catal.* **2010**, 273, 236.

[130] X. Carrier,E. Marceau, H. Carabineiro, V. Rodrı´guez-Gonza´ lezab, M. Cheabd, *Phys. Chem. Chem. Phys.* **2009**, 11, 7527.

[131] T. Yamamoto, A. Orita, T. Tanaka, X-Ray Spectrom. **2008**, 37, 226.

[132] M.A. Corte´s-Ja´come, C. Angeles-Chavez, E. Lo´pez-Salinas, J. Navarrete, P. Toribio, J.A. Toledo, *Appl. Catal. A*, **2007**, 318, 178.

[133] F. D. Gregorio, V. Keller, *J. Catal.* **2004**, 225, 45.

[134] M. Occhiuzzi, D. Cordischi, D. Gazzoli, M. Valigi, P. C. Heydorn, *Appl. Catal. A*, **2004**, 269, 169.

[135] C. Martin, P. Malet, G. Solana, V. Rives, *J. Phys. Chem. B*, **1998**, 102, 2759.

[136] J. E. Herrera, J. H. Kwak, J. Z. Hua, Y. Wang, C. H.F. Peden, J. Macht, E. Iglesia, *J. Catal.* **2006**, 239, 200.

[137] C. Sun, S. Liu, D. Liang, K. Shao, Y. Ren, Z. Su, *J. Am. Chem. Soc.* **2009**, 131, 1883.

[138] C. C. Hwang and C. Y. Mou, *J. Phys. Chem. C*, **2009**, 113, 5212-5221.

[139] A.S. Khder, E.A. El-Sharkawy, S.A. El-Hakam, A.I. Ahmed, *Catal. Comm.* **2008**, 9, 769.

[140] S. L. Barbosa, M. J. Dabdoub, G. R. Hurtado, S. I. Klein,A. C.M. Baroni, C. Cunha, *Appl. Catal. A*, **2006**, 313, 146.

[141] A. E. R. S. Khder, *Appl. Catal. A*, **2008**, 343, 109.

국 문 초 록

바이오매스를 이용한 정밀화학물질의 생산은 기존의 석유화학공정을 대체할 수 있는 방법으로서 각광을 받고있다. 석유와 다르게 바이오매스로부터 유래하는 원재료는 많은 양의 산소를 포함하고 있기 때문에 기존에 석유로부터 생산하던 화학물질을 얻기 위해서는 이 산소의 선택적인 제거가 매우 중요하다. 탈수반응, 에스테르화 반응과 같이 물이 제거되는 탈수적 반응들은 바이오매스 유래 물질로부터 산소를 제거함과 동시에 생성물질에 원하는 기능기를 도입할 수 있기 때문에 위의 목적에 부합하는 효과적인 방법이다. 이 논문에서는 바이오매스로부터 유래하는 C4 화학물질의 전환을 위한 비균일계 탈수적 촉매 공정에 대해 연구하였다.

첫 번째로 바이오매스로부터 유래하는 2,3-부탄디올을 2,3-에폭시부탄으로 전환시킬 수 있는 새로운 탈수반응(탈수적 에폭시화반응)과 이를 이용한 1,3-부타디엔 생산을 위한 비균일계 촉매공정에 대해 논의하고자 한다. 이 탈수반응은 염기성 물질이 담지된 촉매에서 활성을 보이며, 특히 세슘이 담지된 실리카(CsO_x/SiO_2) 촉매가 가장 높은 활성을 보이는 것으로 나타났다. CsO_x/SiO_2 촉매의 높은 활성에 대한 원인을 확인하기 위해 다양한 분석툴을 이용한 구조-활성 관계를

찾고자 하였다. 또한 새로운 반응이 어떤 메커니즘으로 일어나는지를 알기 위해 밀도범함수이론(density functional theory, DFT) 계산을 이용하여 이론적으로 해석하고자 하였다. 분석결과 CsO_x/SiO_2 촉매의 높은 활성의 원인은 다음과 같은 요소들이 복합적으로 작용하였음을 확인하였다: i) Cs^+의 담지로 인한 강한 산점의 생성, ii) Cs^+ 이온의 큰 크기로 인해 SiO_2 내부로 침투하지 않기 때문에 생성된 염기점이 표면에서 반응물과 용이하게 접촉가능, iii) SiO_2 담체와 Cs^+의 강한 결합으로 인한 안정적인 염기점의 생성, iv) 약한 산성을 띠는 SiO_2 표면이 탈수반응을 용이하게 함. 또한 탈수적 에폭시화반응은 meso-2,3-butanediol (R,S)이 trans-2,3-epoxybutane (R,R or S,S)으로 전환되는 키랄성의 변화를 가져오는 S_N2 유사 반응 메커니즘을 따르며, 이는 DFT모사 결과와도 일치하였다. 2,3-부탄디올의 탈수적 에폭시화반응을 통해 생성된 2,3-에폭시부탄은 다른 정밀화학물질의 생산에도 유용하게 활용될 수 있다. 염기성 리튬포스페이트 촉매를 이용하여 반응하였을 때, 2,3-에폭시부탄이 높은 선택도를 보이며 3-부텐-2-올로 전환되는 것을 확인하였다. 여기에 더해, 3-부텐-2-올은 1,3-부타디엔을 생산하기에 매우 적합한 전구체로서 작용하며, 산성을 띠는 중형기공성 알루미노실리케이트 촉매를 이용할 경우 매우 높은 수율을 나타내는 것을 확인하였다.

마지막으로, 산촉매작용을 통해 일어나는 1-부탄올의 에스테르화반응용 고활성촉매를 설계 및 제조하였다. 카르복실산과의 에스테르화를 통해 1-

부탄올은 다양한 종류의 에스터로 전환될 수 있는데, 이들은 환경친화적인 용매, 혹은 향수의 전구체로서 매우 유용하게 활용될 수 있다. 현재 대부분의 에스테르화 반응은 황산과 같은 균일계 산촉매를 이용하여 이루어지는데, 이런 균일계 산촉매의 사용은 반응기의 부식, 그리고 환경적인 문제를 야기한다. 따라서 현재의 문제점을 해결하기 위해서는 비균일계 촉매의 개발이 시급한 실정이다. 이와 관련하여 이 연구에서는 텅스텐산화물 담지 지르코늄 촉매에 주목했다. 이 촉매는 알코올의 탈수반응, 알칸의 이성질화 반응에 좋은 활성을 보이는 것으로 알려졌는데, 이는 촉매표면에 생성되는 Zr−WO_x 클러스터가 높은 산특성을 보이기 때문이라고 밝혀졌다. 하지만 현재 이 Zr−WO_x 클러스터를 높은 밀도로 가지고 있는 촉매를 제조하기 위한 방법에 대해서는 연구가 부족한 실정이다. 이 연구에서는 Zr−WO_x 클러스터를 높은 밀도로 제조하기 위한 중형기공성 Zr−WO_x/SiO_2 촉매를 제안하고, 이 촉매에서 Zr/W의 비율에 따른 구조와 산특성을 조사하였다. 순차적인 지르코늄과 텅스텐의 가수분해와 soft−templating을 통해 강한 산성을 나타내는 Zr−WO_x 클러스터가 균일하게 분포한 중형기공 구조의 물질을 제조하였다. 제조된 Zr−WO_x/SiO_2 촉매의 특성을 질소흡착, XRD, TEM, XPS, UV−Vis분광법, NH_3−TPD, *in−situ* FTIR로 분석하였다. 이 물질은 500 m^2/g 이상의 높은 표면적과 균일하게 정렬된 5 nm의 원통형 기공구조를 가지고 있었다. Zr/W의 비율이 0.5보다 작을 때 지르코늄은 주로 텅스테이트와 함께

존재하는 것이 확인이 되었으며, 이는 Zr−WO_x 클러스터가 주로 형성되었음을 의미한다. 가장 높은 Zr−WO_x 밀도는 Zr/W 비율이 0.3일 때 나타났으며, 또한 가장 강한 Brønsted 산특성을 보였다. 결과적으로 Zr/W 비율이 0.3인 Zr−WO_x/SiO_2촉매가 1−부탄올과 아세트산의 에스테르화 반응에 가장 높은 활성을 보였으며, 이 활성은 기존의 HZSM−5, WO_x/ZrO_2 촉매보다 월등하였다.

주요어: 비균일계 촉매작용, 탈수반응, 에스테르화반응, 반응 메커니즘, 촉매 프로세스
학 번: 2011-30277

List of publications

International Publications

International Academic Published Papers (First Author)

1. T. Y. Kim*, J. Baek*, C. K. Song, Y. S. Yun, D. S. Park, W. Kim, J. W. Han, J. Yi, "Gas-phase Dehydration of Vicinal Diols to Epoxides: From a Mechanism to a Practical Application", *Journal of Catalysis* 2015, 323, 85-99.

   (* Tae Yong Kim and Jayeon Baek contributed equally to this work)

2. D. Yun*, T. Y. Kim*, D. S. Park, Y. S. Yun, J. W. Han, J. Yi (*co-first author) , "A Tailored Catalyst for the Sustainable Conversion of Glycerol to Acrolein: Mechanistic Aspect of Sequential Dehydration", ChemSusChem 2014, 7(8), 2193-220.

   (* Tae Yong Kim and Danim Yun contributed equally to this work)

3. J. Baek*, T. Y. Kim*, W. Kim, H. J. Lee, J. Yi (*co-first author), "Selective production of 1,3-butadiene using glucose fermentation liquor", *Green Chemistry* 2014, 16(7), 3501-3507.

   (* Tae Yong Kim and Jayeon Baek contributed equally to this work)

4. T. Y. Kim, D. S. Park, Y. Choi, J. Baek, J. R. Park, J. Yi, "Preparation and characterization of mesoporous Zr-WO_x/SiO_2 catalysts for the esterification of 1-butanol with acetic acid", *Journal of Materials Chemistry* 2012, 22(19), 10021-10028.

International Academic Published Papers (Co-author)

1. J. Baek*, S. Park*, C. K. Song, T. Y. Kim, I. Nam, J. M. Lee, J. W. Han, and J. Yi, 'Radial alignment of c-channel nanorods in 3D porous TiO_2 for eliciting enhanced Li storage performance", *Chemical Communications* 2015, 51, 15019-15022.

2. H. Park, Y. S. Yun, T. Y. Kim, K. R. Lee, J. Baek, J. Yi, "Kinetics of the dehydration of glycerol over acid catalysts with an investigation of deactivation mechanism by coke", *Applied Catalysis B: Environmental* 2015, 176, 1-10.

3. Y. S. Yun, K. R. Lee, H. Park, T. Y. Kim, D. Yun, J. W. Han, J. Yi, "Rational Design of a Bi-functional Catalyst for the Oxydehydration of Glycerol: A Combined Theoretical and Experimental Study", *ACS Catalysis* 2015, 5, 82-94.

4. D. S. Park*, D. Yun*, T. Y. Kim, J. Baek, Y. S. Yun, J. Yi, "A Mesoporous Carbon-Supported Pt Nanocatalyst for the Conversion of Lignocellulose to Sugar Alcohols", *ChemSusChem* 2013, 6(12), 2281-2289.

5. D. S. Park, D. Yun, Y. Choi, T. Y. Kim, S. Oh, J.-H. Cho, J. Yi, "Effect of 3D open-pores on the dehydration of n-butanol to di-n-butyl ether (DNBE) over a supported heteropolyacid catalyst", *Chemical Engineering Journal*, 2013, 228, 889-895.

6. J. R. Park, B. K. Kwak, D. S. Park, T. Y. Kim, Y. S. Yun, J. Yi, "Effect of Acid Type in WO_X clusters on The Esterification of Ethanol with Acetic Acid", *Korean Journal of Chemical Engineering*, 2012, 29(12), 1695-1699.

Patents Application on File

1. 이종협, 백자연, 박수민, 송찬경, 김태용, 남인호, "삼차원 구조의 구형 타이타니아 제조방법", 특허 출원 10-2015-0133388 (2015.09.21)
2. 이종협, 김태용, 박대성, 최영보, 백자연, 박재률, "균일한 중형 기공을 갖는 복합 산화물 촉매, 그 제조 방법 및 상기 촉매를 이용하여 에스테르 화합물을 제조하는 방법", 특허 출원 10-2012-0053823 (2012.05.21)

International Conferences (First author)

1. T. Y. Kim, J. Baek, C. K. Song, Y. S. Yun, D. S. Park, W. Kim, J. Yi, "Production of 1,3-butadiene from 2,3-butanediol using cesium oxide supported silica catalyst", 24th

North American Meeting of the Catalysis Society, Pittsburgh, PA, USA, Jun. 14-19, 2015.

2. T. Y. Kim, J. Baek, C. K. Song, J. M. Lee, J. W. Han, and J. Yi, "Heterogeneous Catalytic Process for the Production of 1,3-Butadiene from 2,3-Butanediol", The 15th Korea-Japan Symposium on Catalysis, Busan, Korea, May. 26-28, 2015.

3. T. Y. Kim, J. Baek, C. K. Song, Y. S. Yun, D. S. Park, J. Yi, "Density Functional Theory Study on Conversion of Biomass Derived 2,3-Butanediol to 2,3-Epoxybutane", The Korean Society of Clean Technology 2014 Fall Meeting, Gyeongju, Korea, Sep. 24-26, 2014.

4. T. Y. Kim, J. Baek, W. Kim, W. K. Synn, H. J. Lee, J. Yi, "Novel catalytic routes for the selective production of 1,3-butadiene from biomass derived 2,3-butanediol", The 14th Japan-Korea Symposium on Catalysis, WINC Aichi, Nagoya, Japan, July 1-3.

5. T. Y. Kim, S. Yu, J. Baek, J. Yi, "Effect of Zr/W ratio on mesoporous Zr-WO_x/SiO_2 as a solid acid: Formation and optimization of Zr-WO_x clusters", 244th American Chemical Society National Meeting & Exposition, Philadelphia, PA, USA, Aug.19-23, 2012.

International Conferences (Co-author)

1. Y. S. Yun, K. R. Lee, T. Y. Kim, D. Yun, J. W. Han, J. Yi, "Bi-functional Mo-V-W-O catalysts for the one-step production of acrylic acid from glycerol and verification via first principle calculations", 24th North American Meeting of the Catalysis Society, Pittsburgh, PA, USA, Jun. 14-19, 2015.

2. D. Yun, T. Y. Kim, Y. S. Yun, J. M. Lee, J. W. Han, and J. Yi, "Ab initio study of the surface model of amorphous aluminosilicate", The 15th Korea-Japan Symposium on Catalysis, Busan, Korea, May. 26-28, 2015.

3. Y. S. Yun, T. Y. Kim, D. Yun, H. Park, J. M. Lee, J. W. Han, and J. Yi, "Mechanistic insight of hydrogenolysis of glycerol over Cu-based catalysts via ab initio

calculations", The 15th Korea-Japan Symposium on Catalysis, Busan, Korea, May. 26-28, 2015.

4. J. Baek, T. Y. Kim, Y. S. Yun, and J. Yi, "Heterogeneous Catalytic Conversions of Alcohols/polyols Derived from Biomasses to Fine Chemicals", The 15th Korea-Japan Symposium on Catalysis, Busan, Korea, May. 26-28, 2015.

5. S. Park, J. Baek, C. K. Song, T. Y. Kim, I. Nam, J. W. Han, and J. Yi, "Rational design of 3D TiO_2 for use in Li-ion battery", 227th ECS Meeting, Chicago, Illinois, USA, May. 24-28, 2015.

6. C. K. Song, J. Baek, T. Y. Kim, S. Yu, J. Yi, "Synthesis of 3D Hierarchical TiO_2 and Its Application to Phenol Photodegradation Reaction", The Korean Society of Clean Technology 2014 Fall Meeting, Gyeongju, Korea, Sep. 24-26, 2014.

7. J. Baek, T. Y. Kim, I. Nam, S. Park, S. Yu, S. Bae, S. Y. Lee, H. N. Umh, Y. H. Kim, J. Yi, "Production of valuable chemicals (1,3-butadiene) from biomass-based resources alternative to the petroleum", 248th American Chemical Society National Meeting & Exposition, San Francisco, CA, USA, Aug. 10-14, 2014.

8. D. S. Park, D. Yun, Y. S. Yun, H. Park, T. Y. Kim, J. Baek, J. Yi, "Direct conversion of lignocellulose to sugar alcohols over Pt supported on a new 3D mesoporous carbon", 247th American Chemical Society National Meeting & Exposition, Dallas, Texas, USA, Mar. 16-20, 2014.

9. D. S. Park, D. Yun, Y. Choi, T. Y. Kim, S. Oh, J.-H. Cho, and J. Yi, "Enhancement of Mass Transport over 3D Open-porous Dandelion-like Catalyst in Liquid-phase Heterogeneous Catalysis", 9th World Congress of Chemical Engineering, Coex, Seoul, Korea, August 18-23, 2014.

10. J. Baek, T. Y. Kim, W. Kim, W. K. Synn, H. J. Lee, J. Yi, "New synthetic pathway for the catalytic production of 1,3-butadiene using 2,3-butanediol and succinic acid derived from glucosic biomass", The 14th Japan-Korea Symposium on Catalysis, WINC Aichi, Nagoya, Japan, July 1-3.

11. D. Yun, D. S. Park, T. Y. Kim, S. Oh, Y. A. Shin, J. Yi, ”Preparation of DSS-SO_3H Catalyst for Stable Production of Acrolein from Glycerol”, The 14th Japan-Korea Symposium on Catalysis, WINC Aichi, Nagoya, Japan, July 1-3.

Domestic Conferences

1. 김태용, 백자연, 윤양식, 박대성, 문원균, 김우영, 한정우, 이종협, “비시널 디올의 탈수반응을 통한 에폭사이드 화합물의 생성 및 이를 통한 바이오매스 유래 2,3-부탄디올로부터 1,3-부타디엔 생산”, 추계 한국화학공학회, 대전컨벤션센터, 10. 23-24 (2014)
2. 윤양식, 이경록, 박홍석, 김태용, 윤다님, 서영종, 김왕규, 이중원, 한정우, 이종협, “글리세롤의 산화탈수반응을 위한 이원기능촉매 개발 및 적용”, 추계 한국화학공학회, 대전컨벤션센터, 10. 23-24 (2014)
3. 송찬경, 백자연, 김태용, 유성주, 이종협, “계층 구조를 가진 3차원 TiO2의 제조 및 이를 이용한 페놀 광분해 반응에의 응용”, 추계 한국청정기술학회, 경주 K호텔, 9 .24-26 (2014)
4. 김태용, 백자연, 송찬경, 윤양식, 박대성, 이종협, “밀도범함수이론을 이용한 바이오매스 유래 2,3-부탄디올의 2,3-에폭시부탄으로의 전환에 대한 연구”, 추계 한국청정기술학회, 경주 K호텔, 9. 24-26 (2014)
5. 윤다님, 김태용, 박대성, 윤양식, 이종협, 한정우, 오석일, 신용안, “글리세롤로부터 아크롤레인을 안정적으로 생산하기 위한 맞춤형 촉매 개발’, 춘계 한국화학공학회, 창원컨벤션센터, 4. 23-25 (2014)
6. 백자연, 김태용, 박대성, 박홍석, 송찬경, 이경록, 이종협, “글루코오스 발효액으로부터의 1,3-부타디엔 생성”, 춘계 한국화학공학회, 창원컨벤션센터, 4. 23-25 (2014)
7. 윤다님, 김태용, 박대성, 윤양식, 한정우, 이종협, “열린 기공 구조를 갖는 브뢴스테드 산촉매의 제조 및 글리세롤 탈수반응에의 적용’, 춘계 한국청정기술학회, 여수경도리조트, 3. 27-28 (2014)
8. 윤양식, 박홍석, 윤다님, 박대성, 김태용, 백자연, 이경록, 이종협, “계층구조를 갖는 나노크기의 고체산촉매 제조 및 응용”, 춘계 한국청정기술학회,

여수경도리조트, 3. 27-28 (2014)

9. 백자연, 김태용, 송찬경, 이종협, “글루코오스 발효액을 이용한 1,3-부타디엔 생성 반응”, 춘계 한국청정기술학회, 여수경도리조트, 3. 27-28 (2014)
10. 김태용, 백자연, 송찬경, 윤양식, 박대성, 한정우, 이종협, “바이오매스 유래 물질의 맞춤형 탈수반응을 위한 비시널 디올로부터 에폭사이드 유래 물질 생성”, 춘계 한국청정기술학회, 여수경도리조트, 3. 27-28 (2014)
11. 백자연, 송현돈, 김태용, 박대성, 윤다님, 윤양식, 박홍석, 이종협, “금 나노입자의 암모니아 보란을 이용한 4-니트로페놀 환원 반응에서의 실시간 전자이동 관찰”, 추계 한국청정기술학회, 제주한화리조트, 9. 25-27 (2013)
12. 윤양식, 박대성, 윤다님, 김태용, 오석일, 이종협, “무수소 조건에서의 글리세롤의 가수소분해 반응을 위한 중형기공 알루미나에 담지된 구리-니켈 이중금속촉매의 제조 및 적용’, 춘계 한국청정기술학회, 여수 경도리조트, 3. 28-29 (2013)
13. 김태용, 백자연, 김우영, 신우균, 이희종, 이종협, “고부가가치 1,3-부타디엔의 생산을 위한 바이오매스 유래 2,3-부탄디올의 전환 및 이를 위한 촉매 공정”, 춘계 한국청정기술학회, 여수경도리조트, 3. 28-29 (2013)
14. 백자연, 윤다님, 최영보, 김태용, 김우영, 이희종, 김영훈, 이종협, “이산화탄소/프로판을 원료로 사용하는 프로필렌 제조용 촉매 공정 개발 1. 고효율 촉매 설계 및 제조”, 추계 한국청정기술학회, 영남대학교, 11. 16 (2012)
15. 김태용, 박대성, 백자연, 최영보, 김영훈, 이종협, “바이오매스 유래 알코올과 유기산의 고부가가치용 촉매개발 연구”, 추계 한국청정기술학회, 영남대학교, 11. 16 (2012)
16. 김태용, 박대성, 최영보, 백자연, 이종협, “바이오매스로부터 고부가가치 화학물질 제조와 중형기공성 Zr-WO_x/SiO_2 촉매의 개발”, 춘계 한국청정기술학회, 연세대학교, 5.25 (2012)
17. 김태용, 박대성, 최영보, 백자연, 박재률, 이종협, “부탄올 에스테르화 반응을 위한 중형기공의 Zr-WO_x/SiO_2 촉매의 제조 및 특성 분석”, 춘계 한국화학공학회, 제주국제컨벤션센터, 4.25-27 (2012)
18. 박대성, 곽병규, 김태용, 박재률, 윤양식, 이종협, “다공성 구형 실리카에 담지된 헤테로폴리산 촉매의 제조 및 불균일 촉매반응에의 적용”, 추계 한국

화학공학회, 송도컨벤시아, 10. 26-28 (2011)

19. 곽병규, 박대성, 박재률, 윤양식, 김태용, 이종협, “폐글리세롤 수소첨가분해 반응용 $CuCr_2O_4$ 촉매에서 조촉매의 효과”, 추계 한국화학공학회, 송도컨벤시아, 10. 26-28 (2011)